

**The Spectrum of Kaon States in the
Isodoublet strangeness $S = 1$ T_{1u} Channel
by the Stochastic LapH Method in Lattice
QCD**

by
You-Cyuan Jhang

Submitted in partial fulfillment of the
requirements for the degree of
Doctor of Philosophy
at
Carnegie Mellon University
Department of Physics
Pittsburgh, Pennsylvania

Advisor: Professor Colin Morningstar

December 20, 2013

Abstract

Lattice QCD calculations of energies in bosonic channels have mostly been restricted to the use of quark-antiquark meson operators due to the computational challenges associated with evaluating correlation functions of multi-meson operators. The stochastic LapH method has provided an efficient way to compute correlation functions involving multi-hadron operators. This method is applied to construct a 58×58 correlation matrix using 9 single-meson operators and 49 two-meson operators in the isodoublet strangeness $S = 1$ T_{1u} channel, which contains the spin-1 and spin-3 kaon states. The matrix of temporal correlations is evaluated using a Monte Carlo ensemble of 551 configurations on an anisotropic $24^3 \times 128$ lattice. Due to computational limitations, light quark masses are used that produce an unphysically heavy pion having a mass around 390 MeV, but the strange quark mass is tuned to its physical value. A clover-improved Wilson fermion action is used in generating the Monte Carlo ensemble, and the correlators are formed using source and sink operators constructed out of Laplacian Heaviside smeared quark fields displaced with stout-smeared gauge links. Overlap factors are used to identify the finite-volume eigenstates that should evolve into the kaon resonances in infinite volume. These results are compared to experiment and to results from a previous study for the isovector nonstrange T_{1u}^+ channel.

Acknowledgments

I would like to express my deep gratitude to Prof. Colin Morningstar, my research advisor, for his encouragement, guidance, and help with this research. To the other members of my thesis committee, Prof. Stephen Wallace, Prof. Brian Quinn and Prof. Rupert Croft, thank you for your efforts and feedback. I would also like to thank Prof. K. Jimmy Juge, Prof. John Bulava, Dr. Chik Him Wong, Dr. David Lenkner, Dr. Justin Foley and Brendan Fahy for their persistent work in our collaboration, and Dr. Balint Joo and Dr. Robert Edwards for their work in generating the gauge configurations used in this work. I extend my gratitude to all of the faculty and staff in the Physics Department at Carnegie Mellon University for financial support and assistance when I needed it. I thank Prof. Curtis Meyer, along with my research advisor, for maintaining our Medium Energy Group computer cluster. Finally, I would like to thank my family in Taiwan for their love, support, and constant encouragement over the years.

Contents

1	Introduction	1
2	Lattice QCD	9
2.1	Imaginary-time path-integral formalism	10
2.2	Discretization of the QCD Action	12
2.2.1	Link Variables	13
2.2.2	The Gauge Action	14
2.2.3	The Quark Action	17
2.3	Monte Carlo Integration	21
2.3.1	Importance Sampling	22
2.3.2	Metropolis-Hastings Algorithm	23
2.3.3	Introduction of a pseudofermion field	24
2.3.4	The HMC Algorithm	26
2.3.5	The RHMC method	28
2.3.6	Updating Improvements	29
2.4	Action and Ensemble Parameters	30
3	Hadronic Operators	33
3.1	Smearing of Link Variables	33
3.2	Smearing of Quark Fields	35
3.3	Covariant Displacements	36
3.4	Single-Hadron Operators	38
3.4.1	Symmetry Transformations on the Lattice	38
3.4.2	Meson Elemental Operators	39
3.4.3	Baryon Elemental Operators	40
3.4.4	Group-Theory Projections	42
3.4.5	Flavor and G Parity Considerations	46
3.4.6	Summary of Single-Hadron Operators	50
3.5	Multi-hadron Operators	50
3.5.1	Group-Theory Projections	51
3.5.2	Flavor Consideration of Multi-hadrons	52

4	Hadronic Correlators	55
4.1	Quark Propagators and the LapH Subspace	56
4.2	Stochastic LapH Method with Noise Dilution	61
4.3	Correlator Construction of Hadrons	65
4.3.1	Meson to Meson Correlators	65
4.3.2	Baryon to Baryon Correlators	68
4.3.3	Two-Meson to Meson correlators	70
4.3.4	More Complicated Correlators	72
4.3.5	Avoiding Biased Estimates	72
5	Implementation and Analysis	75
5.1	Correlator Matrix Analysis	75
5.1.1	Noise Reduction	75
5.1.2	“Rotated” Correlation Matrices	76
5.1.3	Effective Masses	78
5.1.4	Fitting the Correlators	78
5.1.5	Error Analysis Using Resampling Methods	79
5.2	Implementation Details	81
5.3	Smearing Parameters and Dilution Scheme	84
5.4	Single-Hadron Operator “Pruning”	87
5.5	Multi-hadron Operator Testing	89
5.6	Operator Selection in $I = \frac{1}{2}$, $S = 1$, T_{1u} Channel	90
6	Isodoublet strangeness $S = 1$ T_{1u} Spectroscopy Results	98
6.1	Analysis of Correlation Matrix	99
6.2	Level Identification and Spectrum	101
7	Conclusion and Outlook	125

List of Tables

2.1	Ensemble Information	32
3.1	Meson Displacement Types	41
3.2	Baryon Displacement Types	42
3.3	O_h Subduction	45
3.4	Continuous to Lattice Groups	46
3.5	Single-Hadron Flavor Structure	49
3.6	Bosonic States Flavor Content	53
3.7	Fermionic States Flavor Content	54
4.1	Three Types of Quark Lines	60
5.1	The Number of Single-Hadron Operators Produced on Various Ensemble	89
5.2	Single-Hadron Operators	92
5.3	Experimental Expected Levels in T_{1u} Channel and Multi-Hadron Op- erators	95
5.4	Experimental Expected Levels in T_{1u} Channel and Multi-Hadron Op- erators 2	96
5.5	Experimental Expected Levels in T_{1u} Channel and Multi-Hadron Op- erators 3	97

List of Figures

1.1	The Running Coupling $\alpha_s(Q^2)$ and Various Measurements of $\alpha_s(M_z^2)$	3
1.2	Heavy Quark Potential	4
1.3	Ground State Energy Spectrum from Lattice QCD	5
1.4	Isovector Single-Hadron Spectrum on Different Lattice Symmetry Channels	6
4.1	Volume Dependence of the LapH Eigenvalues	61
4.2	Meson Correlators	67
4.3	Baryon Correlators	69
4.4	Two Meson to Meson Correlators	71
4.5	Two Meson to Two Meson Correlators	73
5.1	Choice of σ cutoff	85
5.2	LapH noise vs lattice noise	86
5.3	Volume Effect of LapH Noise	87
5.4	Effective Mass of Localized Operators	91
6.1	Largest Off-Diagonal Elements of Rotated Correlation Matrix	100
6.2	Effective Masses for Levels 0 to 11	102
6.3	Effective Masses for Levels 12 to 23	103
6.4	Effective Masses for Levels 24 to 35	104
6.5	Effective Masses for Levels 36 to 47	105
6.6	Effective Masses for Levels 48 to 56	106
6.7	Overlap Factors for Various Two-Meson Operators (A)	109
6.8	Overlap Factors for Various Two-Meson Operators (B)	110
6.9	Overlap Factors for Various Two-Meson Operators (C)	111
6.10	Overlap Factors for Various Two-Meson Operators (D)	112
6.11	Single-Hadron State Identification Level 0	114
6.12	Single-Hadron State Identification Level 1	115
6.13	Single-Hadron State Identification Level 2	116
6.14	Single-Hadron State Identification Level 3	117
6.15	Single-Hadron State Identification Level 4	118
6.16	Single-Hadron State Identification Level 5	119
6.17	Single-Hadron State Identification Level 6	120

6.18	Single-Hadron State Identification Level 7	121
6.19	Energies of Kaon Resonance Precursor States in $I = \frac{1}{2}, S = 1, T_{1u}$ Channel	123
6.20	Comparison With Isovector Non-strange T_{1u}^+ Channel	124

Chapter 1

Introduction

The development of Quantum Chromodynamics (QCD) dates back to the 1950s and 1960s when an avalanche of hadron states were discovered in experiments involving particle accelerators. The hadron states which were bosons (of integer spin) were termed *mesons*, whereas the fermionic hadron states (of half-integer spin) were called *baryons*. In order to explain these states, the idea that they were composed of constituent particles was proposed separately by Gell-Mann [1] and Zweig [2] in 1964. Gell-Mann called these constituent particles *quarks*, whereas Zweig called them *aces*. The original model involved three flavors of quarks, known as up (u), down (d) and strange (s), but later experiments at higher energies discovered three more flavors of heavier quarks, known as charm (c), bottom (b), and top (t). Quarks are assumed to have half-integer spin and fractional electric charge. Based on this quark postulate, Fritzsch, Gell-Mann and Leutwyler [3] formulated a quantum field theory of the strong interactions later in 1973. Their formulation, known as Quantum Chromodynamics, is widely accepted as the correct theory of the strong interactions.

QCD introduces massless, spin-1 gauge bosons, known as *gluons*, to mediate the interactions between quarks. Both quarks and gluons are assumed to have an additional quantum number or charge known as *color*. QCD is a quantum field theory whose Lagrange density looks remarkably similar to that of Quantum Electrodynamics (QED), but instead of being based on a local $U(1)$ gauge symmetry, it is based on a local $SU(3)$ gauge symmetry. In QED, the mediating bosons, known as photons, only carry the force and are not sources of the force, that is, they are electrically neutral. In contrast, gluons not only carry the force, but they possess color charge and are sources of the force. Whereas photons do not directly interact with other photons

and linear superposition applies in QED, gluons couple strongly to other gluons and linear superposition does not apply in QCD.

The coupling α in QED is small, so most QED computations can be carried out using a power series expansion in the coupling, that is, using perturbation theory. Lorentz-covariant perturbation theory in QED was extensively developed prior to the 1960s, with contributions to any process at a particular power in the coupling being obtained from so-called Feynman diagrams. At short wavelengths, that is, at high energies, the effective coupling α_s in QCD is small and Feynman diagram techniques work well. This property is known as *asymptotic freedom* [4, 5]. Asymptotic freedom is the property of QCD in which the running coupling $\alpha_s(Q)$ decreases as Q increases. Perturbative expansions in QCD are valid only for momentum transfers corresponding to $Q^2 \gg \Lambda_{\text{QCD}}^2$, where Λ_{QCD} is roughly 300 MeV. Theoretical predictions of the running coupling and its value at $Q^2 \approx M_Z^2$ with $M_Z \approx 90$ GeV have been verified in a series of experiments, as shown in Fig. 1.1. Perturbative expansions work reasonably well for processes dominated by large energies, such as deep inelastic scattering, but in the low energy regime pertinent to hadron formation, the running coupling is large and a perturbative approach fails.

Efforts have been made to construct quark models [6, 7] in the low-energy regime using empirical potentials and appropriate symmetry considerations. The QCD *confinement hypothesis* [8] states that only color-singlet objects can be observed, such as mesons and baryons; a lone colored quark cannot be observed in isolation. In quark models, mesons are bound states of quark-antiquark pairs having total zero color, whereas baryons are bound states of three quarks combined in a colorless fashion. Quark models can make predictions about the energies and quantum numbers of low-lying states which agree qualitatively with experiment, especially for heavier quark systems, but predictions about higher excited states are much less reliable. States involving excitations of the gluon field, such as glueballs and hybrid mesons and hybrid baryons, cannot be well described by conventional quark models.

Lattice QCD is a first-principles approach to studying QCD in the low-energy regime. This method was first proposed by Wilson [9] in 1974. In this approach, QCD is formulated on a discrete space-time lattice so that calculations can be done using computers and the Monte Carlo method. The quark fields are placed on the sites of the lattice, and the gluon fields reside on the links connecting the lattice sites. The lattice action is formulated in such a way so as to maintain gauge invariance

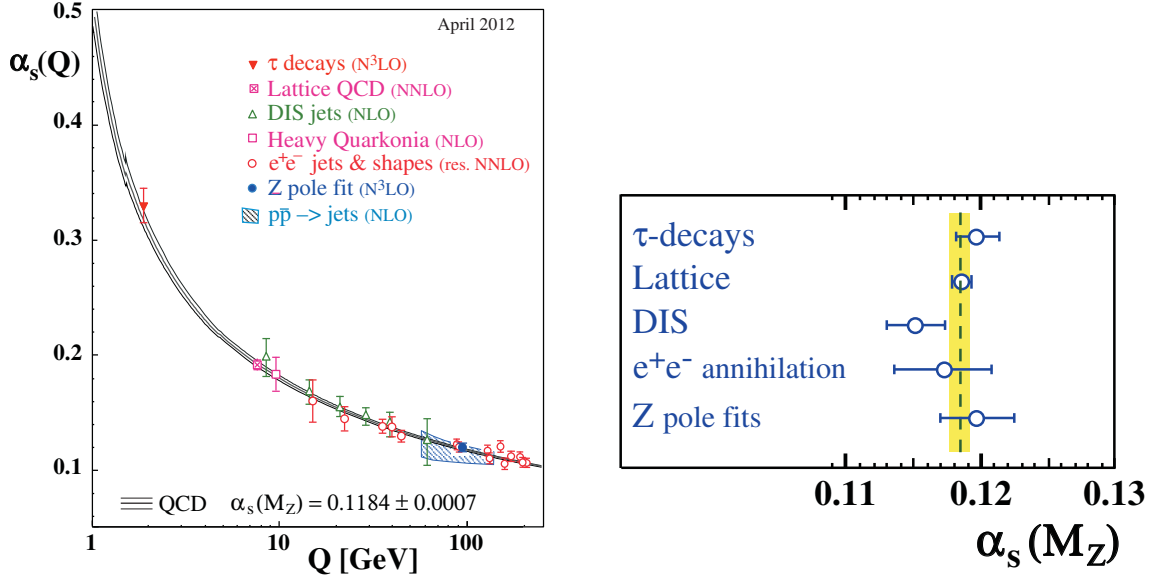


Figure 1.1: (Left) Various measurements of the running coupling α_s as a function of Q , consistent with QCD predictions indicated by solid black lines. (Right) The values of $\alpha_s(M_Z)$, the running coupling at the Z -boson mass M_Z , obtained from various types of measurements and lattice simulations. Each data point is the average of measurements from different collaborations. The yellow region indicates the world average value of $\alpha_s(M_Z) = 0.1184 \pm 0.0007$. Both figures are taken from the Quantum Chromodynamics section in Ref. [6].

applied at the lattice sites, and the imaginary time formalism is exploited to replace the oscillatory exponential of the action with real and positive Boltzmann weights, facilitating the application of the Monte Carlo method. This numerical method has since become the major approach for low-energy QCD calculations.

During the 1970s and 1980s, available computing resources and the Monte Carlo importance-sampling algorithms were of insufficient power to carry out lattice QCD calculations at small lattice spacings and for large volumes. In those days, lattice QCD studies were restricted to the *quenched approximation*, in which the fermion determinant (to be discussed later) in the path integral formulation is set to unity. By the turn of the century, advances in updating-algorithms and computing-power eliminated the quenched approximation, and calculations for lattice spacings below 0.1 fm and volumes greater than $(3 \text{ fm})^3$ are now practical. The small masses of the light u, d quarks greatly slow the computations, so unphysically heavy masses are often used, resulting in a pion mass around 200-400 MeV, instead of 140 MeV, but

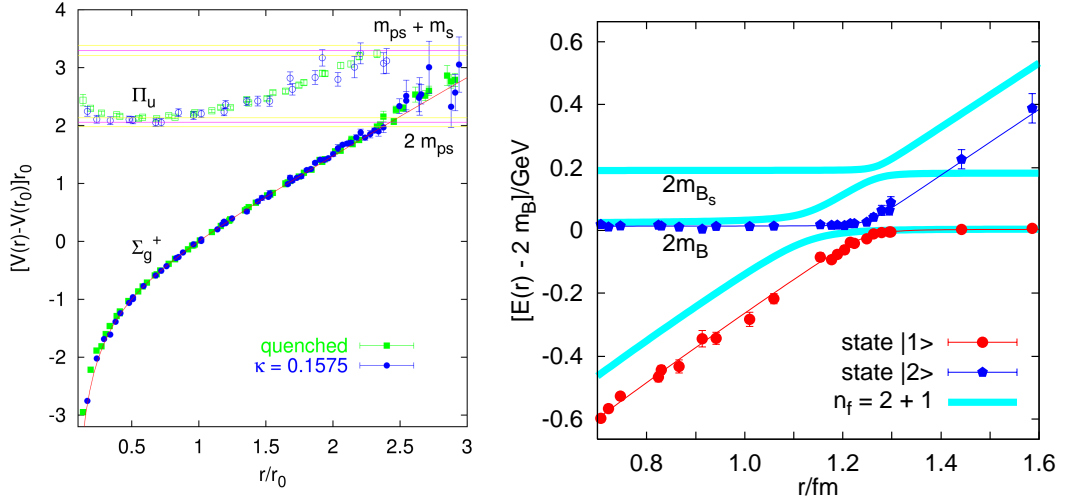


Figure 1.2: (Left) A lattice QCD calculation of the heavy-quark potential $V(r)$ as a function of spatial quark-separation r (see the blue points labeled Σ_g^+). The linear rise for large r confirms the phenomenon of quark confinement. The higher line (label Π_u) represents an excitation of the “flux tube” of gluons between the two heavy quarks, from Ref. [10]. (Right) Observation of string-breaking in QCD with two quark flavors $N_f = 2$. At small r , red points show the static quark potential, and the blue points show the excited-state energy of a state that is two mesons, each consisting of a static heavy quark and a dynamical light quark. As r increases, the energies eventually become comparable, then the two-meson state becomes the lower-lying energy at large r . The bands represent the speculation of the authors for the analogous curves in $N_f = 2 + 1$ QCD, which includes u, d, s quarks. From Ref. [11].

simulations at the physical values are now starting to be possible.

Lattice QCD has been very successful at computing a variety of low-energy quantities, such as the masses of the low-lying hadrons, hadron structure functions, weak-decay constants, and weak-current matrix elements. Two particular successes of lattice QCD are the static quark-antiquark potential and the low-lying hadron spectrum.

Color confinement [8] in QCD suggests that the energy of gluons in the presence of a static quark-antiquark pair should increase with the separation r between the quark and the antiquark, making it impossible to isolate a single quark. A phenomenological potential that rises linearly with r does a reasonably good job of describing the low-lying states of charmonium. A linearly rising potential is suggestive of a string tension, leading many to believe that the gluon field forms a string-like flux tube connecting the quark and the antiquark. Lattice QCD calculations have confirmed such a linearly

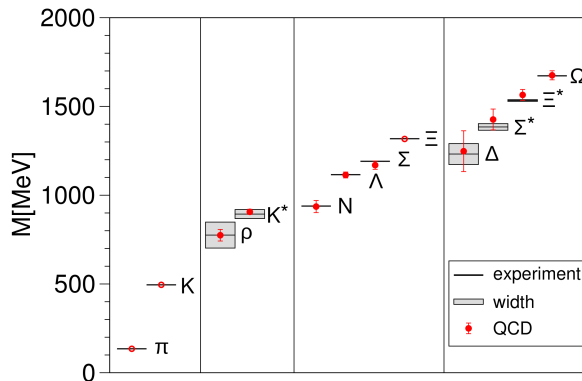


Figure 1.3: A survey of ground state energies in some experimentally well-known symmetry channels, computed with lattice QCD by the BMW collaboration[12].

rising energy at large distances, up until the point at which two mesons can be created, leading to the string breaking. In fact, the static quark potential fits well by a Coulomb-plus-linear potential over a wide range of separations [10], as shown in Fig. 1.2 and string breaking has been demonstrated [11], at least for two quark flavors, as also shown in Fig. 1.2.

Another success of lattice QCD is the mass spectrum of the lowest-lying states in each symmetry channel. A recent calculation is shown in Fig. 1.3, along with experimental results for comparison. These results were the first to be done at the physical point, that is, using u and d quark masses that produce a pion of mass 140 MeV.

Our goal in this work is to make progress towards a first-principles comprehensive determination of the low-lying spectrum of states in QCD using lattice QCD techniques, focusing on the energies of excited states. Such calculations are very challenging. Because of the way in which stationary-state energies are extracted from the temporal correlations of suitable quantum field operators in such calculations, the energy of a particular state of interest can only be determined after contributions from all lower-lying and nearby states in the same symmetry channel are carefully considered. Multi-hadron states populate the spectrum below most of the resonances of interest. To reliably determine the energies of such states, the use of appropriate multi-hadron operators is crucial. The evaluation of correlations involving multi-hadron operators contains new challenges since not only must initial- to final-time quark propagation be included, but also final- to final-time quark propagation must be

incorporated. Reliably estimating such propagators has not been possible until very recently, when new computational techniques, such as the stochastic LapH method, were developed.

A first-pass glimpse of the isovector meson spectrum using only single-meson operators on a $24^3 \times 128$ space-time lattice is shown in Fig. 1.4. The boxes indicate the energies obtained from crude fits, and the shaded areas indicate where multi-hadron states are expected to occur. One sees that careful consideration of mixings with two-hadron states will be important for obtaining reliable energy extractions of the excited states.

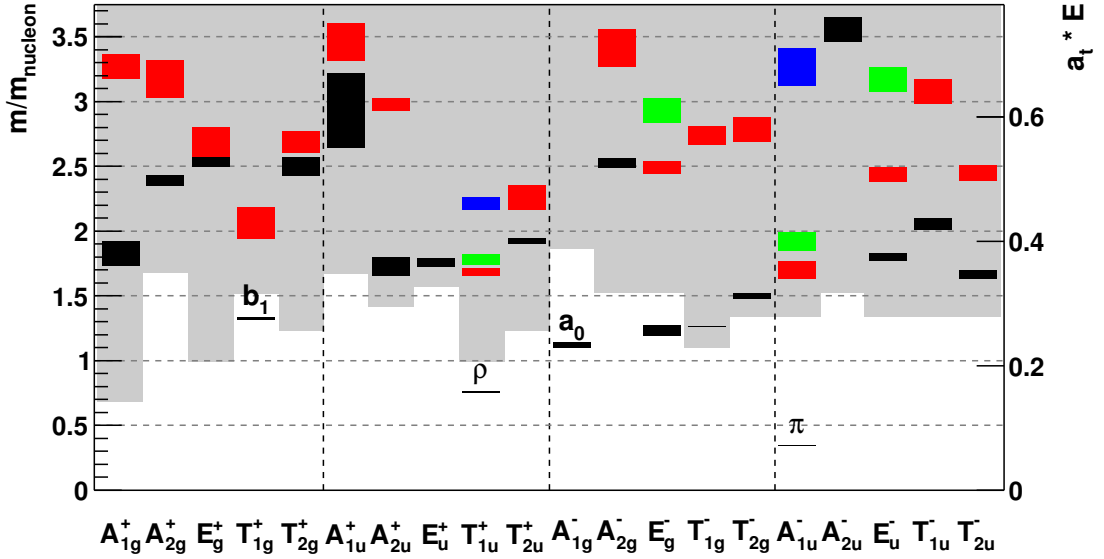


Figure 1.4: The preliminary calculations of isovector single-hadron operators on different lattice-symmetry channels. Each box is the statistical average and error of energy levels extracted using only single-hadron operators. The vertical coordinate on the left is represented in terms of the ratio with respect to nucleon mass on the same lattice simulations. Separate coordinate in terms of inverse temporal lattice spacing is shown on the right. The shaded area is above the threshold of two-meson bound states under the no-interaction approximation of two lowest possible meson states. The ground states, first, second and third excited states are represented by black, red, green and blue boxes in increasing energy order. Results are averaged over 170 configurations on a $(24^3|390)$ ensemble, described in Sec. 2.4. The lattice symmetry channels and single-hadron operators are also discussed in detail in Sec. 3.4.

Good multi-hadron operators are combinations of single-hadron operators that

each create a definite momentum. Such operators, however, are difficult to include in lattice QCD calculations. This difficulty stems from the fact that multi-hadron correlators require the calculation of quark propagation from all spatial points on an initial time slice to all spatial points on another (or the same) time slice. Translational invariance cannot be used to limit the source to one site, as is done in the usual point-to-all method. Correlators involving isoscalar mesons must confront the same difficulty.

In this work, we employ the Stochastic Laplacian Heaviside (Stochastic LapH) algorithm, which provides stochastic estimates of quark propagation that are sufficiently accurate and efficient to allow the evaluations of correlators involving multi-hadrons and isoscalar mesons. A description of this method, with preliminary testing, has been carried out in Refs. [13–15], showing that it is far more efficient than traditional noise-dilution methods. In this work, we review some of these results, but the main focus will be on the application of this method to meson spectroscopy.

This work, and a complementary study[16], are the first to study excited-state spectra in lattice QCD using both single-hadron operators and a complete set of two-hadron operators. Ref. [16] focused on the resonance-rich $I = 1$, $S = 0$, T_{1u}^+ channel, where I denotes isospin, S denotes strangeness, and the T_{1u}^+ notation will be explained later, but includes the spin-1 resonances, such as the ρ meson. Here, we focus on the analogous $I = \frac{1}{2}$, $S = 1$, T_{1u} channel, which includes the spin-1 kaon resonances. We use a 58×58 correlator matrix involving 9 single-hadron operators and 49 two-meson operators. Correlation matrices of this large size have never before been used in lattice QCD. With such a large number of energies extracted, level identification will be a key issue, especially since we study the stationary states of a fully interacting quantum field theory.

Other than the statistical errors that emerge from the Monte Carlo integration, there are systematic errors in our computation. First, there are discretization errors from our use of a finite lattice spacing a . We reduce such errors by using improved discretization schemes, as discussed in Sec. 2.2, but carefully extrapolating to the continuum limit must eventually be done. Another source of errors comes from the use of a finite volume. For the volumes we use, these are adequately suppressed, being $\mathcal{O}(\exp(-m_\pi L))$, where m_π is the pion mass, and L is the spatial extent of the lattice. This is a small effect for all ensembles in this work since $m_\pi L$ is greater than 3. Momenta are quantized in a finite volume and all stationary states are discrete.

Techniques have been developed[17–19] to deduce properties of continuum scattering and decay widths from the finite-volume discrete energy levels. The most serious systematic error in this work comes from our use of u and d quark masses that are too large. The Dirac matrix becomes ill-conditioned as the u and d quark masses approach their physical values. To make our calculations practical, we currently must resort to using u and d quark masses that produce a pion having a mass of 390 MeV or 240 MeV. Our first results reported here are for a 390 MeV pion mass, but results for the 240 MeV pion mass will be available in the near future.

This work is structured as follows. In Chap. 2, a brief review of the lattice QCD formalism is presented. The formulation of a discretized action is discussed, the Monte Carlo method with importance sampling for estimating QCD path integrals is described, and the Monte Carlo ensembles we use are detailed. In Chap. 3, the design and construction of our single-hadron and multi-hadron operators are discussed. The hadronic correlators are the topic of Chap. 4. The stochastic LapH method is reviewed, and the evaluations of the various type of correlators are discussed. Our data analysis methods are detailed in Chap. 5, and other implementation details are presented. Our results for the energy levels in the $I = \frac{1}{2}$, $S = 1$, T_{1u} channel on a $24^3 \times 128$ lattice with pion mass around 390 MeV are then presented in Chap. 6. We use a 58×58 correlator matrix involving 9 single-hadron operators and 49 two-meson operators. The work concludes with a summary in Chap. 7, and future improvements are discussed.

Chapter 2

Lattice QCD

Lattice QCD calculations are performed using the path-integral formulation of quantum field theory. Instead of approximating the path integrals using a perturbative method, the lattice QCD approach places the system on a space-time lattice and performs the path integration by the Monte Carlo method. The space-time lattice provides an ultraviolet cutoff of order a^{-1} , where a is the lattice spacing. The discretized QCD action is no longer invariant under the rotations, translations, and boosts of continuous space-time, but exact local gauge invariance is maintained through the use of link variables, which are path-ordered exponentials of the gluon field along the links connecting the lattice sites. The gauge-covariant derivatives of the continuum action are approximated using finite differences in terms of the link variables, and this introduces discretization errors that are $O(a)$ or higher. Such errors can be reduced by so-called improvement terms in the lattice QCD, introduced to cancel off the leading discretization effects. Wick rotation of the QCD action to imaginary time is necessary for applying Monte Carlo method techniques. Integration over the quark fields is done exactly, but this introduces a nonlocal determinant involving the gluon field. This determinant is handled by introducing a pseudofermion field. The Monte Carlo method used in this work is known as the Rational Hybrid Monte Carlo (RHMC) method, which is a variant of the Markov-chain Metropolis method with a sophisticated method of proposing an update.

This chapter is organized as follows. The path integral formulation and the QCD action in imaginary time are reviewed in Sec. 2.1. The discretization of the QCD action is described in Sec. 2.2. In Sec. 2.3, we describe our implementation of the Monte Carlo method. Along with the basic ideas of Monte Carlo method, the algo-

rithms that are used to deal with dynamical fermions are discussed. Some details of the gauge configurations used in this work are summarized in Sec. 2.4.

2.1 Imaginary-time path-integral formalism

Lattice QCD calculations start with the path-integral formulation [20] of quantum field theory defined through the partition function

$$\mathcal{Z} = \int \mathcal{D}\Phi e^{iS[\Phi]}, \quad S[\Phi] = \int d^4x \mathcal{L}[\Phi], \quad (2.1)$$

where Φ represents all fields in the system, and $S[\Phi]$ is the action obtained by 4-spatial integration of the Lagrangian density $\mathcal{L}[\Phi]$. The functional measure $\mathcal{D}\Phi$ indicates an integration over all field configurations. QCD is defined in terms of quark fields $\psi, \bar{\psi}$ and the non-Abelian gauge fields A_μ , and the partition function is given by

$$\mathcal{Z} = \int \mathcal{D}A_\mu \int \mathcal{D}\psi \mathcal{D}\bar{\psi} e^{i(S_F + S_G)}, \quad (2.2)$$

where the action is the sum of the gauge field part S_G and the fermion field part S_F , which are the 4-spatial integrations of the Lagrangian density \mathcal{L}_G and \mathcal{L}_F , respectively, given by

$$\mathcal{L}_G = -\frac{1}{4} F_{\mu\nu}^c F_c^{\mu\nu}, \quad F_{\mu\nu}^c = \partial_\mu A_\nu^c - \partial_\nu A_\mu^c - ig[A_\mu^c, A_\nu^c], \quad (2.3)$$

$$\mathcal{L}_F = \bar{\psi}(i\gamma_\mu D_\mu - m)\psi, \quad D_\mu = \partial_\mu - igA_\mu, \quad (2.4)$$

where g is the coupling constant. A full description of the fermion fields with all indices is given by $\psi_{\alpha c}^B(x)$ and $\bar{\psi}_{\alpha c}^B(x)$, with space-time position denoted by x , the flavor index $B = 1, 2, \dots, N_f$ required for N_f -flavored QCD, and the Dirac index $\alpha = 1, 2, 3, 4$ for the four spinor components. The gauge field is described by vector field

$$A_\mu(x) = \sum_{c=1}^8 A_\mu^b(x) T_c, \quad (2.5)$$

with Lorentz index $\mu = 0, 1, 2, 3$ and color index c , where T_c are the eight Hermitian, traceless generators of $SU(3)$ matrices.

Monte Carlo estimates of quantum field theory path integrals generally have very

large variances unless importance sampling is exploited. However, only functions that have the properties of a probability density can be incorporated into the importance sampling. In particular, such functions must be real and non-negative. Since the oscillatory factor $e^{iS[\Phi]}$ in the Minkowski-space path integral formalism is complex valued, we apply a Wick rotation to imaginary time $t \rightarrow -i\tau$ in order to obtain a real and nonnegative weighting $e^{-S[\Phi]}$. Under this Wick rotation, the space-time coordinates and the vector fields are transformed according to

$$x^4 = x_4 = ix_M^0 = ix_0^M, \quad x^j = x_j = x_M^j = -x_j^M, \quad (2.6)$$

$$A^4 = A_4 = -iA_M^0 = -iA_0^M, \quad A^j = A_j = -A_M^j = iA_j^M, \quad (2.7)$$

where the superscript M implies Minkowski space-time and the Minkowski-space metric is $g_{\mu\nu} = \text{diag}(1, -1, -1, -1)$. Here $\mu = 4$ is the imaginary time coordinate and $j = 1, 2, 3$ are the original spatial coordinates. The Dirac γ -matrices transform according to

$$\gamma^4 = \gamma_4 = \gamma_M^0 = \gamma_0^M, \quad \gamma^j = \gamma_j = -i\gamma_M^j = i\gamma_j^M, \quad (2.8)$$

$$\{\gamma_\mu, \gamma_\nu\} = 2\delta_{\mu\nu}, \quad \gamma_\mu^\dagger = \gamma_\mu, \quad \gamma^5 = \gamma_5 = \gamma_4\gamma_1\gamma_2\gamma_3 = \gamma_M^5. \quad (2.9)$$

The QCD path-integral partition function in imaginary time has the form

$$\mathcal{Z} = \int \mathcal{D}A_\mu \int \mathcal{D}\psi \mathcal{D}\bar{\psi} e^{-(S_F + S_G)}, \quad (2.10)$$

where the gluon and fermion Lagrangian densities are then

$$\mathcal{L}_G = \frac{1}{4} F_{\mu\nu}^c F_{\mu\nu}^c, \quad F_{\mu\nu}^c = \partial_\mu A_\nu^c - \partial_\nu A_\mu^c + ig[A_\mu^c, A_\nu^c], \quad (2.11)$$

$$\mathcal{L}_F = \bar{\psi}(\gamma_\mu D_\mu + m)\psi, \quad D_\mu = \partial_\mu + igA_\mu. \quad (2.12)$$

The imaginary-time formulation is used throughout this work.

All observables of QCD are contained in the n -point correlation functions of the theory. We extract the energies of the stationary states of QCD from the two-point temporal correlation functions

$$C_{ij}(t_F - t_0) = \frac{\int \mathcal{D}A_\mu \int \mathcal{D}\psi \mathcal{D}\bar{\psi} \{O_i[\psi, \bar{\psi}, A_\mu](t_F) \bar{O}_j[\psi, \bar{\psi}, A_\mu](t_0)\} e^{-(S_F + S_G)}}{\int \mathcal{D}A_\mu \int \mathcal{D}\psi \mathcal{D}\bar{\psi} e^{-(S_F + S_G)}}, \quad (2.13)$$

where the operators $\overline{O}_j[\psi, \overline{\psi}, A_\mu](t_0)$ create the states of interest at source time t_0 and the operators $O_i[\psi, \overline{\psi}, A_\mu](t_F)$ annihilate these states at a later sink time t_F . Equation (2.13), formulated on a space-time lattice, is the main quantity that we calculate in this work.

2.2 Discretization of the QCD Action

A naive discretization of the QCD action can be achieved by taking the continuum QCD action and replacing the continuous space-time variable x_μ with discrete lattice variables $x_\mu \rightarrow n_\mu a_\mu$, where a_μ is the lattice spacing in direction $\hat{\mu}$ and the vector n_μ labels the points in space-time lattice. Field, field derivatives and space-time integrations are replaced by

$$\Phi(x) \rightarrow \Phi(n), \quad (2.14)$$

$$\partial_\mu \Phi(x) \rightarrow \frac{1}{2a_\mu} [\Phi(n + \hat{\mu}) - \Phi(n - \hat{\mu})], \quad (2.15)$$

$$\int d^4x \rightarrow \left(\prod_\mu a_\mu \right) \sum_n, \quad (2.16)$$

for a general field Φ , keeping boundary conditions in mind. However, such a simple discretization of the QCD action does not preserve a key symmetry of the theory, namely, local gauge invariance. The QCD action in continuous space-time is invariant under a local gauge transformation, given by

$$\psi(x) \rightarrow \Omega(x) \psi(x), \quad (2.17)$$

$$\overline{\psi}(x) \rightarrow \overline{\psi}(x) \Omega^\dagger(x), \quad (2.18)$$

$$A_\mu(x) \rightarrow \Omega(x) A_\mu(x) \Omega^\dagger(x) - \frac{i}{g} \Omega(x) \partial_\mu \Omega^\dagger(x), \quad (2.19)$$

where $\Omega(x)$ is a 3×3 unitary matrix of unit determinant, that is, an element of $SU(3)$. Wilson solved this [9] by expressing the action in terms of path-ordered exponentials of the gluon field, known as link variables. Another problem one encounters in formulating QCD on a lattice is the so-called fermion doubling problem [21], in which additional degrees of freedom which are absent in the continuum limit appear in the lattice theory. Solutions to the doubling problem are presented in Sec. 2.2.3.

An anisotropic lattice in which the temporal lattice spacing a_t is smaller than the spatial lattice spacing a_s is used in this work. This is important for adequately resolving the correlators associated with higher lying excited states. Details of these issues are discussed below.

2.2.1 Link Variables

A formulation of Euclidean nonabelian gauge theory that preserves local gauge invariance was first proposed by Wilson [9] to study QCD confinement non-perturbatively. He introduced the *gauge transporter* $G(x, y)$ defined by

$$G(x, y) = P e^{ig \int_x^y A_\nu(z) dz_\nu}, \quad (2.20)$$

where A_ν is the gluon field and P denotes path-ordering along the curve starting from x and ending at y . In lattice QCD, we associate a gauge transporter with each link connecting neighboring sites of the lattice:

$$U_\mu(x) = G(x, x + \hat{\mu}). \quad (2.21)$$

The quantities $U_\mu(x)$ are known as *gauge links* or *link variables*.

The link variables are not gauge-invariant objects. Under a local gauge transformation $\Omega(x)$, which are $SU(3)$ matrices, the link variables transform as

$$U_\mu(x) \rightarrow \Omega(x) U_\mu(x) \Omega^\dagger(x + \hat{\mu}). \quad (2.22)$$

One of the simplest gauge-invariant objects in lattice QCD is the trace of the product of link variables around the smallest possible closed loop, known as a *plaquette*:

$$U_{\mu\nu}(x) \equiv \text{Tr} \left[U_\mu(x) U_\nu(x + \hat{\mu}) U_\mu^\dagger(x + \hat{\nu}) U_\nu^\dagger(x) \right] \approx e^{iga^2 F_{\mu\nu}(x)}. \quad (2.23)$$

The connection between plaquettes $U_{\mu\nu}$ and the field stress tensor $F_{\mu\nu}$ follows from

$$U_\mu(x) \approx e^{iga A_\mu(x)}. \quad (2.24)$$

Given the above connection, one can use the plaquettes as the basic building blocks for the discretized gauge action.

2.2.2 The Gauge Action

From the expansion of $U_{\mu\nu}$ in terms of the lattice spacing a in Eq. (2.23), a suitable discretization of the QCD gauge action is given by

$$S_G^W = \frac{\beta}{\xi_0} \sum_{x, i < j} \left\{ 1 - \frac{1}{6} [U_{ij}(x) + U_{ij}^\dagger(x)] \right\} + \beta \xi_0 \sum_{x, i} \left\{ 1 - \frac{1}{6} [U_{it}(x) + U_{it}^\dagger(x)] \right\}, \quad (2.25)$$

where β is related to the bare coupling constant g through $\beta = 6/g^2$. Here, an anisotropic lattice is used with bare gauge anisotropy parameter ξ_0 . As usual, the Roman letters $i, j = 1, 2, 3$ are used to denote spatial directions, and t denotes the temporal direction. The classical small- a expansion of Eq. (2.25) indicates [22] that the leading discretization error is of order $O(a^2)$. Additional terms can be added to cancel off the leading discretization error and create a so-called improved action.

The construction of improved actions using perturbation theory was first proposed by Symanzik [23, 24], who applied such an approach to the ϕ^4 theory and the nonlinear σ -model. A simple example using a scalar field in one dimension serves to illustrate the method. The simplest finite difference approximation to a classical field derivative is $D^{(2)}[\Phi](x) = \frac{1}{2a}[\Phi(x+a) - \Phi(x-a)]$. For a small a , the Taylor expansion of $\Phi(x \pm a)$ shows that

$$D^{(2)}[\Phi](x) = \Phi'(x) + \frac{a^2}{6}\Phi'''(x) + O(a^4). \quad (2.26)$$

We can also define an operator $D^{(4)}[\Phi](x)$ using

$$D^{(4)}[\Phi](x) = \frac{1}{4a}[\Phi(x+2a) - \Phi(x-2a)] \quad (2.27)$$

$$= \Phi'(x) + \frac{4a^2}{6}\Phi'''(x) + O(a^4). \quad (2.28)$$

The combination $D^{(S)}[\Phi](x) = \frac{4}{3}D^{(2)}[\Phi](x) - \frac{1}{3}D^{(4)}[\Phi](x)$ has discretization error of $O(a^4)$, compared to the naive finite difference operator $D^{(2)}[\Phi](x)$ that had $O(a^2)$ correction terms. In the quantum theory, radiative corrections complicate the above considerations. Improvement coefficients can be determined order by order in the coupling g of the theory by matching various scattering amplitudes in the lattice theory with that of the continuum theory.

In a similar manner, Lüscher and Weisz [25], as well as Curci [26], used the same matching procedure to improve the Wilson gauge action. The unimproved Wilson

discretization is known to match the continuum form $\mathcal{L}_G^{(0)} \propto \text{Tr}(F_{\mu\nu}F_{\mu\nu})$, with a leading error of order $O(a^2)$. Therefore, improvement involves identifying the possible $O(a^2)$ contributions. Three terms involving an extra covariant derivative D_μ with $F_{\mu\nu}$ are given by

$$\begin{aligned}\mathcal{L}_{G,1}^{(2)} &= \text{Tr}(D_\mu F_{\mu\nu} D_\mu F_{\mu\nu}), \\ \mathcal{L}_{G,2}^{(2)} &= \text{Tr}(D_\sigma F_{\mu\nu} D_\sigma F_{\mu\nu}), \\ \mathcal{L}_{G,3}^{(2)} &= \text{Tr}(D_\mu F_{\mu\nu} D_\sigma F_{\sigma\nu}).\end{aligned}$$

To eliminate the $O(a^2)$ terms, one has to choose bigger path-ordered loops other than simple 1×1 plaquettes. The 2×1 path-ordered loops suffice to cancel the $O(a^2)$ terms at leading order in perturbation theory. More explicitly, we define the rectangular Wilson loops as

$$U_{\mu\nu}^R = U_\mu(x)U_\mu(x + \hat{\mu})U_\nu(x + 2\hat{\mu})U_\mu^\dagger(x + \hat{\mu} + \hat{\nu})U_\mu^\dagger(x + \hat{\nu})U_\nu^\dagger(x). \quad (2.29)$$

The appropriate coefficients for combining these two types of Wilson loops are shown for an isotropic lattice in Ref. [25, 26], which produces the tree-level $O(a^2)$ Symanzik improved gauge action. On an anisotropic lattice, separate treatment for the spatial and temporal directions is required.

In the Symanzik approach, the couplings in the lattice QCD action are power series expansions in g . As long as the coefficients of higher powers of g are small in these couplings, the use of perturbation theory is justified. However, one finds in lattice QCD that the coefficients of the higher powers of g become uncomfortably large. Lepage and Mackenzie[27] identified the source of these large contributions as the so-called tadpole diagrams in the lattice perturbation theory. They recommended absorbing the effects of these diagrams into tadpole-improvement parameters, then the resulting perturbative expansions of the couplings multiplying the tadpole-improved operators were found to be much better behaved and could be treated in perturbation theory. *Tadpole improvement* [27, 28] removes unphysical ultraviolet fluctuations introduced by the gauge transporter. The improvement is carried out by renormalizing the spatial and temporal link variables through a mean-field approximation u , defined by the

expectation of plaquettes $U_{\mu\nu}$

$$u = \left\langle \frac{1}{3} \text{ReTr}(U_{\mu\nu}) \right\rangle^{1/4}. \quad (2.30)$$

It can be shown [27, 28] that the expectation value is dominated by ultraviolet fluctuations. The link variables U_μ are then replaced by U_μ/u in the action. For an anisotropic lattice, separate spatial tadpole factor u_s and temporal tadpole factor u_t are used.

For our lattices, one finds that u_t is very close to unity, so $u_t = 1$ is used [29]. The parameter u_s is set using small Monte Carlo calculations. One computes u_s using the expectation value of the spatial plaquette as in Eq. (2.30) for a given input value of u_s , repeating the calculations until the input value matches the output value. More details can be found in Ref. [29].

In summary, we choose the gauge action used in Ref. [29, 30] with tree-level Symanzik improvement and tadpole improvement, given by

$$S_G = \frac{5\beta}{3\xi_0 u_s^4} \Omega_s + \frac{4\beta\xi_0}{3u_s^3 u_t^2} \Omega_t - \frac{\beta}{12\xi_0 u_s^6} \Omega_s^R - \frac{\beta\xi_0}{12u_s^4 u_t^2} \Omega_t^R, \quad (2.31)$$

where Ω_s and Ω_t terms are tadpole improved Wilson gauge action defined including only Wilson plaquettes

$$\Omega_s = \sum_{x,i < j} [1 - P_{ij}(x)], \quad \Omega_t = \sum_{x,i} [1 - P_{it}(x)], \quad (2.32)$$

$$P_{\mu\nu} = \frac{1}{6} \text{Tr} [U_{\mu\nu}(x) + U_{\mu\nu}^\dagger(x)] = \frac{1}{3} \text{Re Tr} [U_\mu(x) U_\nu(x + \hat{\mu}) U_\mu^\dagger(x + \hat{\nu}) U_\nu^\dagger(x)]. \quad (2.33)$$

The Symanzik-improvement terms with 2×1 rectangle Wilson loops are defined by

$$\Omega_s^R = \sum_{x,i \neq j} [1 - R_{ij}(x)], \quad \Omega_t^R = \sum_{x,i} [1 - R_{it}(x)] \quad (2.34)$$

$$R_{\mu\nu} = \frac{1}{3} \text{Re Tr} [U_\mu(x) U_\mu(x + \hat{\mu}) U_\nu(x + 2\hat{\mu}) U_\mu^\dagger(x + \hat{\mu} + \hat{\nu}) U_\mu^\dagger(x + \hat{\nu}) U_\nu^\dagger(x)]. \quad (2.35)$$

The discretization error for this action is $O(a_t^2, g^2 a_s^2, a_s^4)$. Eq. (2.31) is the final form of the QCD gauge-field action used here.

2.2.3 The Quark Action

A naive discretization of the quark action can be achieved by replacing the covariant derivative D_μ in the fermion action by the covariant finite difference ∇_μ :

$$D_\mu(x, y) \rightarrow \nabla_\mu(x, y) = \frac{1}{2a_\mu} \left[U_\mu(x) \delta(x + \hat{\mu}, y) - U_\mu^\dagger(x - \hat{\mu}) \delta(x - \hat{\mu}, y) \right]. \quad (2.36)$$

The link variable $U_\mu(x)$ in the above finite difference is required to keep the discretized fermion action gauge invariant. The naive quark action S_F^N can be expressed as

$$S_F^N = \sum_x \bar{\psi}(y) K^N(x, y) \psi(x), \quad (2.37)$$

$$K^N(x, y) = \left[\sum_{i=1}^3 \gamma_i \nabla_i(x, y) + \gamma_t \nabla_t(x, y) + m \delta(x, y) \right], \quad (2.38)$$

where K^N represents the naive discretization of the Dirac matrix. The Dirac matrix is not Hermitian, but rather, it satisfies the condition

$$K^{N\dagger} = \gamma_5 K^N \gamma_5. \quad (2.39)$$

The above relation ensures that the eigenvalues of K^N are real or come in complex conjugate pairs, which guarantees that the determinant of the Dirac matrix is real, an important feature for the application of the Monte Carlo method.

The above action suffers from the fermion doubling problem [21]. This can be seen [31] by considering the Fourier transformation of the Dirac matrix in the gauge-free limit ($U_\mu = 1$). To simplify the discussion, we restrict our attention to an isotropic lattice. The momentum-space two-point propagator of the quark fields is given by the inverse of the Dirac matrix K^N :

$$\langle \psi(p) \bar{\psi}(q) \rangle = [K^N(p, q)]^{-1} = \delta(p, q) \frac{-\frac{i}{a} \sum_\mu \gamma_\mu \sin(ap_\mu) + m}{\left[\frac{1}{a} \sum_\mu \sin(ap_\mu) \right]^2 + m^2}, \quad (2.40)$$

which is obtained using the Fourier transformation of Eq. (2.13) and carrying out the path integration over the quark fields. In the continuum limit $a \rightarrow 0$, the above expression is expected to have single pole at $p^2 = -m^2$, when $\sin(p) \rightarrow p$. However, the above discretization introduces 15 additional poles at $(p - \Pi)^2 = -m^2$, where Π

denotes the four vector with one of the four elements being set to π/a_μ . These extra unphysical poles are referred to as the fermion doublers. They correspond to modes that do not occur in the continuum theory. The presence of gauge fields does not remove these fermion doublers.

The fermion doubling problem is difficult to solve. The Nielsen and Ninomiya no-go theorem [32] states that there are no fermion discretization schemes which satisfy locality, chiral symmetry, and have the correct continuum limit without introducing fermion doublers. Maintaining the correct continuum limit is crucial, so any discretization scheme that removes the doublers has to break either locality or chiral symmetry. One choice is the staggered fermion formulation[33–35]. In the staggered fermion formulation, one spreads the four Dirac components over neighboring sites, so that the fermion degrees of freedom are thinned out over the lattice. This breaks locality, but maintains a remnant of chiral symmetry. This formulation produces other problems that make the extraction of excited states very difficult. Another choice that preserves exact chiral symmetry is the domain-wall formulation [36, 37], which introduces an extra fifth space-time dimension. The overlap formulation [38, 39] is equivalent to domain-wall fermions as the extent of the fifth dimension is made large and integration over certain fields are carried out. These fermion formulations break locality since the extra terms from the fifth dimension have to couple to the original four-dimensional action to remove the doublers. Both the domain-wall and overlap formulations are very expensive to use. In this work, we use the Wilson fermion formulation [40], in which an extra term is introduced in the fermion action which raises the energies of the fermion doublers so that they do not pollute the low-lying spectrum. The added term explicitly breaks chiral symmetry.

The choice of discretization scheme depends on the problem of interest and its computational cost. Wilson fermions are less expensive to use, and the problem of broken chiral symmetry can be alleviated through the use of stout-smeared links [41] in the fermion action (described later in Sec. 3.1). In discrete-time, the transfer matrix $T = e^{-H a_t}$ is the temporal-evolution operator, where H is the Hamiltonian of the continuous-time version of the theory. Positivity of the transfer matrix ensures that the corresponding Hamiltonian is Hermitian, which is crucial for our determination of the spectrum.

As proposed by Wilson [40], the fermion doubling problem can be avoided by

adding a Laplacian term Δ_μ , defined as

$$\Delta_\mu(x, y) = \frac{1}{a_\mu^2} \left[U_\mu(x) \delta(x + \hat{\mu}, y) + U_\mu^\dagger(x - \hat{\mu}) \delta(x - \hat{\mu}, y) - 2\delta(x, y) \right]. \quad (2.41)$$

The anisotropic Wilson fermion action S_F^W is then given by

$$S_F^W = \sum_x \bar{\psi}(y) K^W(x, y) \psi(x), \quad (2.42)$$

$$K^W(x, y) = \left\{ \sum_{i=1}^3 \left[\gamma_i \nabla_i(x, y) - \frac{a_s}{2} \Delta_i(x, y) \right] + \left[\gamma_t \nabla_t(x, y) - \frac{a_t}{2} \Delta_t(x, y) \right] + m \delta(x, y) \right\}. \quad (2.43)$$

The additional term in the action can be regarded as an extra mass term that is momentum-dependent. In the free-field limit as in Eq. (2.40), the inverse of this new Dirac matrix K^W is given in momentum space by

$$[K^W(p, q)]^{-1} = \delta(p, q) \frac{-\frac{i}{a} \sum_\mu \gamma_\mu \sin(a_\mu p_\mu) + \left[m - \frac{1}{a} \sum_\mu (\cos(ap_\mu) - 1) \right]}{\left[\frac{1}{a} \sum_\mu \sin(a_\mu p_\mu) \right]^2 + \left[m - \frac{1}{a} \sum_\mu (\cos(ap_\mu) - 1) \right]^2}. \quad (2.44)$$

From Eq. (2.44), one observes that the only low-lying pole is then at $p^2 = -m^2$ as $a \rightarrow 0$. The doubler poles are raised so that their energies are of $O(a^{-1})$. It is straightforward to show that K^W satisfies γ_5 Hermiticity (see Eq. (2.39)), as required for application of the Monte Carlo method.

The leading discretization error for the Wilson fermion action is $O(a)$. To reduce this lattice artifact, the Symanzik procedure [23, 24] can again be followed to remove the $O(a)$ terms. The possible $O(a)$ contributing terms are

$$\begin{aligned} \mathcal{L}_{F,1}^{(1)} &= \bar{\psi} \sigma_{\mu\nu} F_{\mu\nu} \psi, \\ \mathcal{L}_{F,2}^{(1)} &= \bar{\psi} \vec{D}_\mu \vec{D}_\mu \psi + \bar{\psi} \overleftarrow{D}_\mu \overleftarrow{D}_\mu \psi, \\ \mathcal{L}_{F,3}^{(1)} &= m \text{Tr}(F_{\mu\nu} F_{\mu\nu}), \\ \mathcal{L}_{F,4}^{(1)} &= m [\bar{\psi} \gamma_\mu \vec{D}_\mu \psi - \bar{\psi} \gamma_\mu \overleftarrow{D}_\mu \psi], \\ \mathcal{L}_{F,5}^{(1)} &= m^2 \bar{\psi} \psi, \end{aligned}$$

where $\sigma_{\mu\nu} = \frac{1}{2i}[\gamma_\mu, \gamma_\nu]$. Note that $\mathcal{L}_{F,3}^{(1)}$ and $\mathcal{L}_{F,5}^{(1)}$ can be absorbed into the original action through a redefinition of bare-mass parameter m and bare-coupling constant, whereas $\mathcal{L}_{F,2}^{(1)}$ and $\mathcal{L}_{F,4}^{(1)}$ terms can be shown [22] to be combinations of $\mathcal{L}_{F,1}^{(1)}$ restricted by the Dirac equation $(\gamma_\mu D_\mu + m)\psi = 0$. Hence, it suffices to add an extra term that has the continuum limit as $\mathcal{L}_{F,1}^{(1)}$.

The most commonly-used choice is due to Sheikholeslami and Wohlert [42], who added the so-called *clover* term $c_{sw}\bar{\psi}\frac{1}{2}\sigma_{\mu\nu}F_{\mu\nu}^{sw}\psi$ to the Wilson action, where the field-strength $F_{\mu\nu}^{sw}$ is defined using the sum of four plaquettes $Q_{\mu\nu}$ as follows:

$$F_{\mu\nu}^{sw}(x) = \frac{1}{8ia_\mu a_\nu} \left[Q_{\mu\nu}(x) - Q_{\mu\nu}^\dagger(x) \right], \quad (2.45)$$

$$Q_{\mu\nu}(x) = U_{\mu\nu}(x) + U_{\nu-\mu}(x) + U_{-\mu-\nu}(x) + U_{-\nu\mu}(x). \quad (2.46)$$

The leading contribution [42] of this clover term can be shown to approach $\mathcal{L}_{F,1}^{(1)}$ with appropriate coefficient c_{sw} calculated from perturbation theory. Again, large radiative corrections to the c_{sw} coefficient can be avoided by including tadpole-improvement factors. Here, we use $\tilde{u}_{s,t}$ to distinguish from the tadpole factors $u_{s,t}$ introduced for the gauge action.

In summary, we use the clover-improved, tadpole-improved, anisotropic Wilson fermion action S_F given by

$$S_F = \sum_x \bar{\psi}(y) K(x, y) \psi(x), \quad (2.47)$$

$$\begin{aligned} K(x, y) = & \left\{ \frac{1}{\nu \tilde{u}_s} \sum_i \left[\gamma_i \nabla_i(x, y) - \frac{a_s}{2} \Delta_i(x, y) \right] \right. \\ & \left. + \frac{1}{\tilde{u}_t} \left[\gamma_t \nabla_t(x, y) - \frac{a_t}{2} \Delta_t(x, y) \right] + m \delta(x, y) \right\} \\ & - \frac{1}{2} \left\{ \frac{c_s a_s}{\tilde{u}_s^3} \sum_{i < j} \sigma_{ij} F_{ij}^{sw}(x) \delta(x, y) + \frac{c_t a_t}{\tilde{u}_t \tilde{u}_s^2} \sum_i \sigma_{ti} F_{ti}^{sw}(x) \delta(x, y) \right\}, \end{aligned} \quad (2.48)$$

where the parameter ν is the ratio of bare gauge anisotropy ξ_0 to the bare fermion anisotropy, and $c_s = 1$ and $c_t = \frac{1}{2}(1 + 1/\xi)$, where $\xi = a_s/a_t$ is the desired lattice aspect-ratio. The tuning of these parameters will be discussed later in Sec. 2.4. The leading discretization error of this improved fermion action is of $O(g^2 a_s, g^2 a_t, a_s^2, a_t^2)$. Note that the above Dirac matrix K satisfies γ_5 Hermiticity as in Eq. (2.39), as needed for application of the Monte Carlo method.

2.3 Monte Carlo Integration

In this section, we focus on how we estimate the QCD path integrals defined on a space-time lattice as described in the previous section. First, note that we can separate the path integral in Eq. (2.10) into an integration over the fermion fields and an integration over the link variables:

$$\mathcal{Z} = \int \mathcal{D}U e^{-S_G[U]} \int \mathcal{D}\psi \mathcal{D}\bar{\psi} \exp \left[\sum_x \bar{\psi}(x) K(x, y) \psi(y) \right], \quad (2.49)$$

where the gauge field A used in the continuum formulation is then replaced with the link variables U in the lattice formulation. The gauge action S_G is defined in Eq. (2.31), and the fermion action is given in Eq. (2.47), with $K(x, y)$ defined in Eq. (2.48). The path integral over the fermion Grassmann fields $\psi, \bar{\psi}$ in Eq. (2.49), being of Gaussian form, can be evaluated exactly using the *Matthews-Salam formula* [43, 44], yielding

$$\mathcal{Z} = \int \mathcal{D}U e^{-S_G[U]} \det[K], \quad (2.50)$$

where $\det[K]$ is called the *fermion determinant*. The use of *Wick's theorem* [45] allows us to evaluate the two-point correlation functions defined in Eq. (2.13), obtaining

$$C_{ij}(t_F - t_0) = \frac{\int \mathcal{D}U e^{-S_G[U]} \det[K] \mathcal{F}[K^{-1}]}{\int \mathcal{D}U e^{-S_G[U]} \det[K]}, \quad (2.51)$$

where $\mathcal{F}[K^{-1}]$ depends on the particular source and sink operators involved. The function \mathcal{F} is typically a sum of products of K^{-1} corresponding to the fermion field pairs ψ and $\bar{\psi}$ appearing in Eq. (2.13), as prescribed by Wick's theorem. The remaining path integrals over the link variables for the two-point correlation functions, which involve the fermion determinant $\det[K]$ and the inverse of the Dirac matrix K^{-1} , cannot be evaluated exactly, so we resort to estimating them with the Monte Carlo method.

2.3.1 Importance Sampling

The Monte Carlo method with importance sampling provides estimates [46] of the correlation functions in Eq. (2.51) given by

$$C_{ij}(t - t_0) \approx \langle \mathcal{F} \rangle \pm \frac{1}{\sqrt{N_{\text{cfg}}}} \left(A_0(\mathcal{F}) + 2 \sum_{h \geq 1} A_h(\mathcal{F}) \right)^{1/2}, \quad (2.52)$$

$$\langle \mathcal{F} \rangle = \frac{1}{N_{\text{cfg}}} \sum_{i=1}^{N_{\text{cfg}}} \mathcal{F}[K^{-1}; U^{(i)}] \quad (2.53)$$

$$A_h(\mathcal{F}) = \frac{1}{N_{\text{cfg}} - h} \sum_{i=1}^{N_{\text{cfg}} - h} \left(\mathcal{F}[K^{-1}; U^{(i)}] - \langle \mathcal{F} \rangle \right) \left(\mathcal{F}[K^{-1}; U^{(i+h)}] - \langle \mathcal{F} \rangle \right), \quad (2.54)$$

where the N_{cfg} configurations $\{U^{(i)}\}$ are chosen randomly with probability density $w[U]$ given by

$$w[U] = \frac{e^{-S_G[U]} \det[K]}{\int \mathcal{D}U e^{-S_G[U]} \det[K]}. \quad (2.55)$$

The quantity $A_h(\mathcal{F})$ is known as the autocorrelation function. The Monte Carlo approximation above is justified by the central limit theorem. The statistical error decreases as the number of samples N_{cfg} increases. For the method to be applicable, the importance-sampling weight $w[U]$ must have the properties of a probability, namely, it must be real and nonnegative, and satisfy $\int \mathcal{D}U w[U] = 1$ (directly followed by Eq. 2.55). The γ_5 -Hermiticity of Dirac matrix K ensures that $\det K$ is real, and positivity follows from the properties of our fermion action.

The random selection of the set of configurations $\{U^{(i)}\}$ for the Monte Carlo integration is done using a discrete-“time” Markov process whose equilibrium is the probability density $w[U]$. A Markov chain is used which is a sequence of randomly-chosen gauge configurations $\{U^{(k)}\}$, where k labels the discrete Markov “time” along the chain [22, 47, 48]; the probability of selecting the k -th configuration $U^{(k)}$ in the chain depends only on the previous configuration $U^{(k-1)}$ and no earlier times in the history of the chain. This is a key property of a Markov process. The Markov process used must have a unique equilibrium distribution

$$\int \mathcal{D}U p(U' \leftarrow U) w[U] = w[U'], \quad (2.56)$$

that coincides with a fixed-point distribution. This can be ensured if the transition probability $p(U' \leftarrow U)$ allows every configuration to eventually be reached from every other configuration (ergodicity), and if the transition probability satisfies a *detailed balance* [47] condition:

$$p(U' \leftarrow U)w[U] = p(U \leftarrow U')w[U']. \quad (2.57)$$

Ergodicity and the existence of the fixed-point enable us to start from an arbitrary distribution and eventually reach the equilibrium distribution.

2.3.2 Metropolis-Hastings Algorithm

One simple method that provides a transition probability satisfying detailed balance is the *Metropolis-Hastings method* [49, 50]. In this algorithm, one uses a proposal probability $R(U' \leftarrow U)$ satisfying ergodicity to suggest a new configuration U' , then an accept-reject step is applied. The suggested configuration is accepted with a probability

$$P_{\text{acc}}(U' \leftarrow U) = \min\left(1, \frac{R(U \leftarrow U')w[U']}{R(U' \leftarrow U)w[U]}\right). \quad (2.58)$$

If the candidate configuration is rejected, the current configuration U is retained. The process of using R to suggest a new configuration, then applying the accept-reject step is known as an “update.” This procedure produces a Markov chain whose limiting stationary distribution is $w[U]$. Note that the normalization of $w[U]$ does not play a role in the accept-reject step, so this normalization never needs to be computed. Also note that if the proposal probability is reversible, that is, if $R(U' \leftarrow U) = R(U \leftarrow U')$, then the dependence on R drops out of the acceptance probability, and this even simpler method is known as the Metropolis method.

In practical applications of the Metropolis-Hastings method, one usually starts the Markov chain with an arbitrarily selected configuration. One then applies a large number of updates until the chain reaches its stationary limit and is in equilibrium. One typically monitors a handful of observables, and when the Monte Carlo estimates of these observables no longer change, one is reasonably certain that the equilibrium of the chain has been reached. This process of evolving the Markov chain into its equilibrium from an arbitrarily starting point is known as *thermalization*. Only configurations encountered *after* thermalization are used in our estimates of the temporal

correlations of hadron operators.

In the Metropolis-Hastings method, one has significant freedom to choose the proposal probability density. If the application of the probability R is reasonably inexpensive, then an acceptance rate of around 50% is the rule of thumb. Such an acceptance rate is large enough to avoid wasting a lot of time with rejections, but allows large enough configuration changes in order to explore most of the volume of configuration space within practically achievable values of N_{cfg} . It is also important to choose an R that keeps autocorrelations reasonably small. The error term in Eq. (2.52) can be uncomfortably large if the autocorrelations A_h are not small. An easy trick to reduce autocorrelations is to avoid using consecutive configuration along the Markov chain. Instead, one selects configurations for the Monte Carlo estimate only after some number N_{skip} of Metropolis-Hastings updates. As lattice systems near a critical point, in which spatial correlations become large, simple choices for R tend to suffer from a phenomenon known as *critical slowing down* [51] in which the N_{skip} required to produce small autocorrelations becomes very large. In such cases, better and more efficient R probabilities must be used.

Accurate Monte Carlo estimates in lattice field theory depend on using efficient algorithms to make updates to the field across the entire lattice. In other words, global updates having a reasonable acceptance rate are needed. If it were not important to include the $\det K$ in the importance sampling, then such global updates could be achieved by sweeping through the lattice, carrying out local updates of single link variables, such as proposed by Creutz [52, 53] and others and improved through the *heat bath algorithm* [54, 55] and *overrelaxation* [56] method. Each local update involves small changes to the fields, leading to a good acceptance rate. However, it turns out that inclusion of the $\det K$ in the importance sampling is crucial for obtaining Monte Carlo estimates with reasonably small variances. The presence of the determinant makes single-link updates nearly as expensive as global updates, so sweeping through the lattice with local updates is not an efficient way of accomplishing the global updates that are needed.

2.3.3 Introduction of a pseudofermion field

The fermion determinant $\det K$ is costly to evaluate exactly, so a reliable means of approximating $\det K$ is necessary. We use a method involving pseudofermion fields [57].

The fermion determinant may be expressed as the path integral in terms of a complex scalar field ϕ of the Gaussian form

$$\det K[U] = \int \mathcal{D}\phi^\dagger \mathcal{D}\phi e^{-\phi^\dagger K[U]^{-1} \phi}, \quad (2.59)$$

where ϕ are extra pseudofermion (bosonic) fields. For N_f quark flavors, the Dirac matrix determinant can be factorized into a product of determinants $K^{(f)}[U]$ for each flavor f :

$$\det(K[U]) = \prod_{f=1}^{N_f} \det(K^{(f)}[U]). \quad (2.60)$$

The Dirac matrix determinant for each flavor is guaranteed to be real from the γ_5 -Hermiticity condition:

$$\begin{aligned} \det(K^{(f)}[U])^* &= \det(K^{(f)\dagger}[U]) = \det(\gamma_5 K^{(f)}[U] \gamma_5) \\ &= \det(\gamma_5) \det(K^{(f)}[U]) \det(\gamma_5) = \det(K^{(f)}[U]), \end{aligned} \quad (2.61)$$

since $\det(\gamma_5)^2 = 1$. We work in the limit that the u and d quarks have the same mass $m_u = m_d$, which means $K^{(u)} = K^{(d)}$ so one can show that the product of their Dirac matrix determinants must also be nonnegative:

$$\begin{aligned} \det(K^{(u)}[U]) \det(K^{(d)}[U]) &= \det(K^{(u)}[U]) \det(K^{\dagger(u)}[U]) \\ &= \det(K^{(u)}[U] K^{\dagger(u)}[U]) \geq 0. \end{aligned} \quad (2.62)$$

The Dirac matrix for the s quark is also real and positive due to the larger s quark mass, but it is convenient to write its determinant in the form

$$\begin{aligned} \det(K^{(s)}[U]) &= (\det(K^{(s)}[U]) \det(K^{\dagger(s)}[U]))^{1/2} \\ &= \det(K^{(s)}[U] K^{\dagger(s)}[U])^{1/2}. \end{aligned} \quad (2.63)$$

Inclusion of the u, d, s quarks only, with $m_u = m_d$, means that we only need to introduce two types of pseudofermion fields, one $\phi^{(l)}$ for the light quarks and one $\phi^{(s)}$ for the s quark. The action in terms of the pseudofermion fields is given by

$$S_{QCD}[U, \phi^{(l)}, \phi^{(s)}] = S_G[U] + \phi^{(l)\dagger} (K[U]^{(l)\dagger} K^{(l)}[U])^{-1} \phi^{(l)}$$

$$+\phi^{(s)\dagger} \left(K^{(s)\dagger}[U]K^{(s)}[U] \right)^{-1/2} \phi^{(s)}. \quad (2.64)$$

The lattice QCD action, written in this form, using pseudofermion fields, is suitable for the *Hybrid Monte Carlo* (HMC) and the *Rational Hybrid Monte-Carlo* (RHMC) methods, discussed below.

2.3.4 The HMC Algorithm

The Hybrid Monte Carlo (HMC) method, introduced by Duane and others [58], provides a means of proposing a global update in lattice QCD that yields a high acceptance rate in the Metropolis-Hastings accept-reject stage. However, it is applicable only when there are an even number of quark flavors occurring in mass degenerate pairs. The HMC algorithm is particularly popular for $N_f = 2$ simulations involving only u, d quarks having the same mass.

This method begins by introducing a fictitious momentum $P_\mu^{(i)}(x)$ that is conjugate to the gauge field $U_\mu^{(i)}(x)$, where μ is the Lorentz label and i is the color label on the basis of eight $SU(3)$ generators. The method utilizes a multivariate Gaussian integral designed to evaluate to unity:

$$1 = \int \mathcal{D}P e^{-\frac{1}{2}P^2}. \quad (2.65)$$

This unity can be inserted into the path-integral expression for the partition function for $N_f = 2$ with $m_u = m_d$:

$$\begin{aligned} \mathcal{Z} &= \int \mathcal{D}P e^{-\frac{1}{2}P^2} \int \mathcal{D}U \mathcal{D}\phi^\dagger \mathcal{D}\phi e^{-S_G[U] - \phi^\dagger (K[U]^\dagger K[U])^{-1} \phi}, \\ &= \int \mathcal{D}U \mathcal{D}\phi^\dagger \mathcal{D}\phi \mathcal{D}P e^{-H}, \end{aligned} \quad (2.66)$$

introducing a fictitious “Hamiltonian” defined by

$$H = \frac{1}{2} \sum_{x,\mu,i} [P_\mu^{(i)}(x)]^2 + S_{QCD}[U, \phi]. \quad (2.67)$$

We then have a path integral over the gauge links U , the pseudofermion fields ϕ , and

the conjugate momenta P . For $N_f = 2$ with $m_u = m_d$, we can write

$$\phi = K[U]^\dagger \chi, \quad \phi^\dagger = \chi^\dagger K[U], \quad (2.68)$$

and express the path integral of the partition function by

$$\mathcal{Z} = \int \mathcal{D}P e^{-\frac{1}{2}P^2} \int \mathcal{D}U \mathcal{D}\chi^\dagger \mathcal{D}\chi e^{-S_G[U] - \chi^\dagger \chi}. \quad (2.69)$$

For current configuration $U_{\text{cur}}, \phi_{\text{cur}}, P_{\text{cur}}$, the HMC method proposes a new U, ϕ, P in the following way:

1. a new set of momenta P and the fields χ, χ^\dagger are randomly selected using the Gaussian distributions $e^{-P^2/2}$ and $e^{-\chi^\dagger \chi}$, respectively,
2. the proposed pseudofermion fields $\phi = K[U_{\text{cur}}]^\dagger \chi$ and $\phi^\dagger = \chi^\dagger K[U_{\text{cur}}]$ are then computed,
3. solve a discrete “time” version of Hamilton’s equations (keeping ϕ, ϕ^\dagger unchanged)

$$\begin{aligned} \dot{U} &= P, \\ \dot{P} &= F = -\frac{\partial S_{QCD}}{\partial U} = -\frac{\partial S_G}{\partial U} - \phi^\dagger \frac{\partial (K[U]^\dagger K[U])^{-1}}{\partial U} \phi, \end{aligned} \quad (2.70)$$

for some length of “time”, where the single dot indicates the differentiation over the fictitious “time” τ (such a solution is known as an HMC trajectory, and is similar to a molecular dynamics (MD) evolution). Note that it is not possible to solve the above equations for continuous time.

The configuration U, P obtained at the end of the HMC trajectory is then the proposed new configuration used in the accept-reject stage. To ensure detailed balance, the proposal probability must be reversible. Hence, the discrete time version of Hamilton’s equations must be solved in a reversible way. Reversibility can be achieved using a symplectic integration scheme, such as the *leapfrog* scheme or Omelyan integration scheme [59]. In this work, the Omelyan scheme is chosen to yield an accuracy up to $O(\delta\tau^3)$, where $\delta\tau^3$ is the discretization error of integration.

Using such an MD evolution, the HMC method generates a new configuration such that δH is small, where the δH is the difference between the new Hamiltonian

after the MD step and the Hamiltonian computed before the refresh of pseudofermion and conjugate momentum fields. A small δH ensures a high acceptance probability $P_{\text{acc}} = \min(1, e^{-\delta H})$.

To compute the force term in Eq. (2.70), the first order derivative about the link variables can be rewritten using the identity $\partial(M^{-1}M)/\partial U = \partial(M^{\dagger-1}M^{\dagger})/\partial U = 0$, so that

$$\phi^{\dagger} \frac{\partial(K[U]^{\dagger}K[U])^{-1}}{\partial U} \phi = -[(K[U]^{\dagger}K[U])^{-1}\phi]^{\dagger} \frac{\partial(K[U]^{\dagger}K[U])}{\partial U} [(K[U]^{\dagger}K[U])^{-1}\phi]. \quad (2.71)$$

The derivative of the matrix $(K[U]^{\dagger}K[U])$ with respect to the gauge field is straightforward. The evaluation of $(K[U]^{\dagger}K[U])^{-1}\phi$ is costly, but unavoidable. Efficient Krylov-space solvers, such as Conjugate Gradient (CG), Generalized Conjugate Residual (GCR) and BiCGstab algorithms, are often used. Further details about linear solvers can be found in Refs. [60, 61].

2.3.5 The RHMC method

The Rational Hybrid Monte-Carlo (RHMC) algorithm [62] is an extension of the HMC method that applies for any number of quark flavors. The u and d quarks are treated in the same way as in HMC, but now the s quarks can be included. The s -quark part of the pseudofermion action is $\phi^{\dagger}(K[U]^{\dagger}K[U])^{-1/2}\phi$ (we omit the s superscript in this section), so we cannot use Eq. (2.68), but instead, we write

$$\phi = (K[U]^{\dagger}K[U])^{1/4}\chi, \quad \phi^{\dagger} = \chi^{\dagger}(K[U]K[U]^{\dagger})^{1/4}. \quad (2.72)$$

Equation (2.72) is then used to compute the pseudofermion field from Gaussian random noise for the χ, χ^{\dagger} fields. The fourth root of the Dirac matrix is approximated using a rational approximation [63],

$$(K[U]^{\dagger}K[U])^{\alpha} \approx r^{\alpha}(K[U]^{\dagger}K[U]) = \sum_i a_i (K[U]^{\dagger}K[U] + b_i)^{-1}, \quad (2.73)$$

where the coefficients a_i and b_i depend on the fraction α , and the force term is replaced by

$$\phi^\dagger \frac{\partial (K[U]^\dagger K[U])^{-1/2}}{\partial U} \phi = - [r^{-1/2} (K[U]^\dagger K[U]) \phi]^\dagger \frac{\partial (K[U]^\dagger K[U])}{\partial U} [r^{-1/2} (K[U]^\dagger K[U]) \phi]. \quad (2.74)$$

The quantity $a_i (K[U]^\dagger K[U] + b_i)^{-1} \chi$ can then be evaluated using a multi-shift solver [64]. More detail about the RHMC algorithm can be found in Ref. [29, 65].

2.3.6 Updating Improvements

A few improvements have been applied to the RHMC algorithm used in this work.

For an anisotropic lattice, a multi-scale molecular dynamics simulation [66] is useful. Different step sizes, $\delta\tau_s$, for spatial directions and $\delta\tau_t$, for the temporal direction, are used in the discretization of the MD integration to compensate for the different forces in the spatial and temporal directions due to the anisotropic lattice. The larger force in the temporal direction requires a finer integration scale. The ratio $\delta\tau_s/\delta\tau_t$ requires an extra fine-tuning, but is expected [29] to be similar to the lattice anisotropy ξ .

Another improvement we use involves separating the high and low modes of the Dirac matrix determinant [67]. For a Dirac matrix M , the determinant of such a matrix can be factorized as

$$\det M = \left(\frac{\det M}{\det M_h} \right) (\det M_h) = \det(M_h) \det(M M_h^{-1}), \quad (2.75)$$

where M_h is the Dirac matrix involving only the higher modes. One then introduces two pseudofermion fields ϕ_l and ϕ_h instead of only one, and the action is written

$$\begin{aligned} S[U, \phi] \rightarrow S[U, \phi_l, \phi_h] &= S_l[U, \phi_l] + S_h[U, \phi_h], \\ S_l[U, \phi_l] &= \phi_l M_h M^{-1} \phi_l, \\ S_h[U, \phi_h] &= \phi_h M_h^{-1} \phi_h. \end{aligned}$$

This separation of high and low modes enables the computation of determinants of smaller matrices, leading to smaller HMC “force” terms [68]. Smaller forces allow the use of larger integration step sizes $\delta\tau$, which dramatically decreases the computation

time it takes the MD evolution to reach a given integral-trajectory length. The multi-scale molecular dynamics evolution is useful for treating the multiple pseudofermion fields which involve different magnitudes of forces.

Another technique we apply is even-odd preconditioning[69]. First, the lattice is separated into so-called even (e) and odd (o) sites; every link on the lattice connects an even site with an odd site. The Dirac matrix can then be expressed in the format

$$K = \begin{pmatrix} K_{ee} & K_{eo} \\ K_{oe} & K_{oo} \end{pmatrix}, \quad (2.76)$$

where K_{ee} and K_{oo} are block diagonal matrices that include the clover term and the mass term involving only the even or odd sites, respectively, and K_{eo} and K_{oe} contain the Wilson hopping terms between the even and odd sites. One can then express K by

$$K = \begin{pmatrix} 1 & 0 \\ K_{oe}K_{ee}^{-1} & 1 \end{pmatrix} \begin{pmatrix} K_{ee} & 0 \\ 0 & K_{oo} - K_{oe}K_{ee}^{-1}K_{eo} \end{pmatrix} \begin{pmatrix} 1 & K_{ee}^{-1}K_{eo} \\ 0 & 1 \end{pmatrix}, \quad (2.77)$$

then

$$\det K = \det(K_{ee}) \det(K_{oo} - K_{oe}K_{ee}^{-1}K_{eo}). \quad (2.78)$$

The preconditioned fermion matrix $\hat{K} = K_{oo} - K_{oe}K_{ee}^{-1}K_{eo}$ typically has a smaller condition number, which dramatically speeds up its inversion. The forces produced by the K_{ee} term are much smaller [29] than the forces from \hat{K} . Again, MD evolution with such a separation of the Dirac matrix is improved using the multi-scale integration.

2.4 Action and Ensemble Parameters

The parameters in the discretized QCD action have to be carefully tuned to yield meaningful physical observables. In particular, these parameters are (a) $\beta = 6/g^2$ where g is the bare QCD coupling, (b) the bare gauge anisotropy ξ_0 , (c) the bare fermion anisotropy ν ; and (d) the bare quark mass parameters m_u , m_d and m_s . In this work, we are interested in using a spatial lattice spacing a_s about 0.1 to 0.2 fm with an anisotropy $a_s/a_t = \xi = 3.5$. These values should [29] provide enough temporal resolution for extracting excited-state energies with sufficiently small discretization errors. Values for the above parameters are determined by computing a few observables in several small-statistics, small-volume simulations for a range of

input values of the parameters to obtain desired matching conditions, as described below. These tuning runs utilize the Schrödinger functional formalism [70, 71]. See Refs. [29, 65] for more details about tuning of the QCD action parameters in this work.

The gauge anisotropy ξ_0 is tuned using the static-quark potential $V_s(r)$, as suggested in Ref. [72]. An $n_\mu \times n_\nu$ Wilson loop $W_{\mu\nu}(x_\mu, x_\nu)$ is defined by

$$W_{\mu\nu}(x_\mu, x_\nu) = \langle 0 | \sum_x \text{Tr} \left[U_\mu(x) U_\nu(x + x_\mu \hat{\mu}) U_{-\mu}(x + x_\mu \hat{\mu} + x_\nu \hat{\nu}) U_{-\nu}(x + x_\nu \hat{\nu}) \right] | 0 \rangle.$$

A ratio of spatial Wilson loops gives the potential V_s in terms of spatial lengths ya_s :

$$R_{ss}(x, y) = \frac{W_{ss}(x, y)}{W_{ss}(x + 1, y)} \rightarrow e^{-a_s V_s(ya_s)},$$

as x becomes large. The ratio of temporal Wilson loops gives the potential V_s in terms of temporal lengths ta_t :

$$R_{st}(x, t) = \frac{W_{st}(x, t)}{W_{st}(x + 1, t)} \rightarrow e^{-a_s V_s(ta_t)},$$

as x becomes large. We tune ξ_0 until the condition $R_{ss}(x, y) = R_{st}(x, \xi y)$ is satisfied for the desired renormalized gauge anisotropy $\xi = a_s/a_t$. For $\xi = 3.5$ using our action, we find $\xi_0 = 4.3$ works well [29]. We can determine the fermion anisotropy ν (defined in Eq. 2.48) from the pion dispersion relation

$$a_t^2 E^2(\mathbf{p}) = a_t^2 m^2 + \frac{1}{\xi^2} a_s^2 |\mathbf{p}|^2 \quad (2.79)$$

where \mathbf{p} are various low-lying three-momenta allowed on the lattice. Using the dispersion relation for ρ mesons and π mesons, a fermion anisotropy $\nu = 3.4$ is found to yield $\xi = 3.5$. These anisotropy parameters turn out to be fairly independent of the bare quark masses.

The two bare quark mass parameters, $m_u = m_d = m_l$ for the light quark and m_s for the s quark, are tuned [65] using the dimensionless ratios defined below, which involve the Ω baryon mass m_Ω , the kaon mass m_K , and the pion mass m_π :

$$l_\Omega = \frac{9m_\pi^2}{4m_\Omega^2},$$

$$s_\Omega = \frac{9(m_K^2 - m_\pi^2)}{4m_\Omega^2}.$$

Unfortunately, inversions of the Dirac matrix for quark masses that produce the physical value of the pion mass are too costly to be practical. Instead, we choose the pion mass to be $m_\pi \approx 240$ Mev or $m_\pi \approx 390$ Mev, which makes our computations possible with available computing resources and allows us to somewhat explore the effects of the unphysical quark masses. In this work, the bare s quark mass parameter is found to be $m_s = -0.0743$, and for $m_\pi \approx 240$ Mev and $m_\pi \approx 390$ Mev, the bare light quark mass parameters are found to be $m_l = -0.0860$ and $m_l = -0.0840$, respectively.

Tuning the parameter β has been investigated in Ref. [29, 65]. Using the experimental value of the Ω baryon mass, one finds that $\beta = 1.5$ results in a spatial lattice spacing $a_s \approx 0.12$ fm. Table 2.1 lists parameter values for different ensembles that are used for testing and for final results in this work. The $(16^3|390)$ and $(20^3|390)$ ensembles are mainly used for testing purposes and the operator selection process. This work focuses on the $(24^3|390)$ ensemble, and future work will focus on the $(32^3|240)$ ensemble. Each ensemble contains N_{cfs} configurations, as indicated in Table 2.1. Successive retained configurations are separated by N_{spacing} RHMC updates in the Markov chain.

Label	$N_s^3 \times N_t$	m_l	N_{cfs}	N_{spacing}
$(16^3 390)$	$16^3 \times 128$	-0.0840	100	40
$(20^3 390)$	$20^3 \times 128$	-0.0840	100	40
$(24^3 390)$	$24^3 \times 128$	-0.0840	551	20
$(24^3 240)$	$24^3 \times 128$	-0.0860	584	20
$(32^3 240)$	$32^3 \times 256$	-0.0860	412	20

Table 2.1: The Monte Carlo ensembles used in our investigations. In the label of each ensemble, the second number after the vertical bar indicates the pion mass of this ensemble. N_{cfs} indicates the number of configurations contained in each ensemble. Successive retained configurations are separated by N_{spacing} RHMC updates in the Markov chains. The light quark mass parameter m_l is listed for each ensemble, while the s quark mass parameter is $m_s = -0.0743$ for all ensembles. The bare gauge anisotropy parameter is $\xi_0 = 4.3$ and the bare fermion anisotropy is $\nu = 3.4$. Using the Ω baryon mass, the spatial lattice spacing is $a_s \approx 0.12$ fm.

Chapter 3

Hadronic Operators

In this chapter, we describe the hadron operators whose temporal correlations we compute using Eq. (2.13). Since we intend to extract the low-lying energy levels from these correlation functions, it is crucial to use hadron operators that couple strongly to the low-lying states. The use of smeared gauge links and quark fields to remove couplings to the high frequency modes is important, and covariant displacements of the quark fields allow us to construct a variety of different hadron operators to capture the different radial and orbital structures of the low-lying states. Hadron operators that transform irreducibly under lattice symmetries also help to factorize the correlation matrices into different symmetry channels.

In Sec. 3.1 and Sec. 3.2, we describe the link variable smearing and the quark field smearing, respectively, used throughout this work. Covariant displacements of the quark fields are described in Sec. 3.3, then the design of single-hadron operators with appropriate symmetry properties is discussed in Sec. 3.4. Finally, the construction of the multi-hadron operators using the single-hadron operators is presented in Sec. 3.5.

3.1 Smearing of Link Variables

Various link smearing methods have been proposed that yield significant noise reduction in physical observables in lattice QCD. One method for Wilson-like gauge actions is the APE smearing algorithm. By averaging the neighboring link variables and projecting back to an $SU(3)$ matrix, this algorithm can provide good gluonic operators [73] for glueball masses and the string tension of the static quark-antiquark potential. However, the final $SU(3)$ projection is not differentiable, which means

this smearing cannot be used in designing an action for a Markov chain with HMC updating. In this work, we use the stout smearing [41] procedure that does not need such projections and is analytic.

Stout smearing makes use of the weighted sum of gauge link staples, defined by

$$C_\mu(x) = \sum_{\nu \neq \mu} \rho_{\mu\nu} [U_\nu(x) U_\mu(x + \hat{\nu}) U_\nu^\dagger(x + \hat{\mu}) + U_\nu^\dagger(x - \hat{\nu}) U_\mu(x - \hat{\nu}) U_\nu(x - \hat{\nu} + \hat{\mu})], \quad (3.1)$$

where $\rho_{\mu\nu}$ is the tunable weighting factor for the sum of staple paths in the ν, μ plane that start at lattice site x and end at $x + \hat{\mu}$. Our hadron operators involve quark and gauge fields at a single time, so we only need to consider smearing the spatial links using nearby spatial links. Therefore, we use $\rho_{4\mu} = \rho_{\mu 4} = 0$. The temporal links are not smeared, and temporal links are not used in smearing the spatial links. To obtain spatial smeared links having the same symmetry properties as the original link variables, we also use a common value $\rho_{jk} = \rho$.

Using these spatial staples, we can define a Hermitian, traceless matrix $Q_\mu(x)$ by

$$\begin{aligned} Q_\mu(x) &= \frac{i}{2} [\Omega_\mu^\dagger(x) - \Omega_\mu(x)] - \frac{i}{6} \text{Tr}[\Omega_\mu^\dagger(x) - \Omega_\mu(x)], \\ \Omega_\mu(x) &= C_\mu(x) U_\mu^\dagger(x). \quad (\text{no summation over } \mu) \end{aligned} \quad (3.2)$$

The smearing matrix $e^{iQ_\mu(x)}$ is unitary and has unit determinant, so it is an element of the Lie group $SU(3)$. We perform the smearing process iteratively by applying the smearing matrix $e^{iQ_\mu(x)}$ in successive sweeps through the lattice. In other words, the smeared link variables obtained after $n + 1$ iterations are given in terms of the smeared links after n steps by

$$U_\mu^{(n+1)}(x) = e^{iQ_\mu^{(n)}(x)} U_\mu^{(n)}(x), \quad (3.3)$$

and we define $U_\mu^{(0)}(x) = U_\mu(x)$ as the original unsmeared gauge links. Since the smearing matrix is an element of $SU(3)$, explicit projection of the link variables back onto $SU(3)$ is unnecessary in this scheme. After n_ρ iterations, we end up with the stout-smeared link variables that we use throughout this work, which we express as

$$\tilde{U}_\mu \equiv U_\mu^{(n_\rho)}. \quad (3.4)$$

We choose $n_\rho = 10$ and $\rho = 0.10$ based on a series of tests presented in Ref. [41].

3.2 Smearing of Quark Fields

The smearing of the quark field is done using an equation of the form

$$\tilde{\psi}_{a\alpha}^A(x) = S_{ab}(x, y) \psi_{b\alpha}^A(y), \quad (3.5)$$

in which x, y are lattice sites, a, b are color indices, A is the flavor index and α is the Dirac spin component index. S is the smearing kernel that is used to reduce couplings to high-lying states, while preserving all of the symmetry properties of the original quark field.

A common choice of the smearing kernel is Gaussian Smearing [74] with the smearing kernel defined as

$$\mathcal{S} = \left(1 + \frac{\sigma_s^2}{n_\sigma} \tilde{\Delta}\right)^{n_\sigma}, \quad (3.6)$$

where σ_s and n_σ are tunable parameters, and n_σ is a positive integer. The Laplacian operator $\tilde{\Delta}$ is defined in terms of the smeared link variables $\tilde{U}_j(x)$ by

$$\tilde{\Delta}_{ab}(x, y; \tilde{U}) = \sum_{k=1}^3 \left\{ \tilde{U}_k^{ab}(x) \delta(y, x + \hat{k}) + \tilde{U}_k^{\dagger ab}(y) \delta(y, x - \hat{k}) - 2\delta(x, y) \delta^{ab} \right\}, \quad (3.7)$$

in which a, b are the color indices and x, y are lattice sites. This gauge-covariant Laplacian matrix is Hermitian and block-diagonal in time. It locally averages the field, but keeps all of the relevant symmetry transformation properties of the original quark field.

Since the Laplacian matrix is Hermitian, the eigenvalues of the matrix $\tilde{\Delta}$ are all real and the eigenvectors can be chosen to be orthogonal. Moreover, all of the eigenvalues of $\tilde{\Delta}$ are negative. Thus, the eigenvectors can be chosen such that $\lambda^{(k+1)} > \lambda^{(k)}$, where $\lambda^{(k)}$ are the eigenvalues of $-\tilde{\Delta}$ with corresponding k -th eigenvector $v^{(k)}$, so that all $\lambda^{(k)}$ are positive.

When n_σ is large, the Gaussian smearing kernel is approximately $e^{\sigma_s^2 \tilde{\Delta}}$, producing suppression of higher lying states via factors such as $e^{-\sigma_s^2 \lambda^{(k)}}$. However, an even

simpler scheme is Laplacian Heaviside (LapH) quark-field smearing[75], defined by

$$\mathcal{S} = \Theta(\sigma_s^2 + \tilde{\Delta}), \quad (3.8)$$

where σ_s is the smearing cutoff parameter. Let V_Δ denote the unitary matrix whose columns are the eigenvectors $v^{(k)}$ of $-\tilde{\Delta}$, and let Λ_Δ denote the diagonal matrix whose nonzero entries are the corresponding eigenvalues. Then

$$\tilde{\Delta} = V_\Delta \Lambda_\Delta V_\Delta^\dagger, \quad (3.9)$$

and the smearing matrix

$$\mathcal{S} = V_\Delta \Theta(\sigma_s^2 + \tilde{\Delta}) V_\Delta^\dagger. \quad (3.10)$$

Note that the gauge-covariant Laplacian $\tilde{\Delta}$ is block diagonal in time, which means we have to solve for eigenvalues and eigenvectors separately on each time slice. The Heaviside function removes eigenvalues $\lambda^{(k)}$ of $-\tilde{\Delta}$ that are greater than the cutoff σ_s . Let N_v denote the number of eigenvectors retained by the Heaviside function for a given time; one finds that N_v is independent of time. To simplify matters[13], we fix N_v to a single appropriate value to approximate the Heaviside function. Thus, the smearing kernel is well approximated by the Hermitian matrix

$$\mathcal{S} \approx V_s V_s^\dagger, \quad (3.11)$$

where V_s represents the matrix whose columns are the lowest-lying N_v eigenvectors in all of the time slices. On a lattice with N_t time slices and N_s spatial sites, V_s is a matrix having $N_v N_t$ columns and $N_s^3 N_c N_t$ rows, where $N_c = 3$. The values of the cutoff σ_s and the number of eigenvectors N_v will be discussed in Sec. 5.3.

3.3 Covariant Displacements

Meson annihilation operators are expected to involve a ψ field with a $\bar{\psi}$ field operator, whereas baryon annihilation operators are expected to involve three ψ fields. To better capture the radial and orbital structures of the large hadron states, one should use operators that extend over several lattice sites, suggesting the use of quark fields displaced from one another. However, local gauge invariance of the hadron opera-

tors has to be carefully maintained. Displacements involving the gauge-field parallel transporters can easily enforce gauge invariance. Such displacements are known as *gauge-covariant displacements*.

The gauge-covariant displacement operator in the j -th direction is defined in terms of the smeared gauge field as

$$\tilde{D}_j^{(p)}(x, x') = \tilde{U}_j(x) \tilde{U}_j(x + \hat{j}) \dots \tilde{U}_j(x + (p-1)\hat{j}) \delta_{x', x+p\hat{j}}, \quad (3.12)$$

where $j = \pm 1, \pm 2, \pm 3$. We use only covariant displacements restricted to spatial lattice directions. The superscript p indicate that this is a displacement of length p , assuming $p \geq 1$. Using displacements in different directions is expected to build up orbital structures, whereas using different displacement lengths can build up different radial structures.

Our meson and baryon operators are constructed using *covariantly-displaced and smeared quark fields*:

$$(\tilde{D}_{j_1}^{(p)} \dots \tilde{D}_{j_n}^{(p)} \tilde{\psi})_{a\alpha}^A, \quad (\tilde{\chi} \tilde{D}_{j_1}^{(p)\dagger} \dots \tilde{D}_{j_n}^{(p)\dagger})_{a\alpha}^A, \quad \chi = \bar{\psi} \gamma_4 \quad -3 \leq j_i \leq 3, \quad (3.13)$$

where a series of different displacement directions $j_1 \dots j_n$ acting on the same quark is used to capture orbital structures. The displacement length p is taken to be the same to simplify our operator construction. Different numbers of displacements yield the different lengths that can build up different radial structures. Also, for convenience, we define $\tilde{D}_0^{(p)}(x, x') = \delta_{x, x'}$, indicating no displacement. Explicitly, our basic building blocks are summarized by

$$q_{a\alpha j}^A = D^{(j)} \tilde{\psi}_{a\alpha}^{(A)}, \quad \bar{q}_{a\alpha j}^A = \tilde{\psi}_{a\alpha}^{(A)} \gamma_4 D^{(j)\dagger} = \tilde{\chi}_{a\alpha}^{(A)} D^{(j)\dagger}, \quad (3.14)$$

where $D^{(j)}$ is shorthand notation for

$$D^{(j)} = D_{j_1 \dots j_n}^{(p)} = \tilde{D}_{j_1}^{(p)} \dots \tilde{D}_{j_n}^{(p)}, \quad (3.15)$$

with $j = (j_1, j_2, \dots, j_n)$ defining a series of displacements along the axes of the lattice, leading to a final displacement vector $\mathbf{d} = \hat{j}_1 + \hat{j}_2 + \dots \hat{j}_n$, keeping in mind that $j = 0$ indicates no displacement.

3.4 Single-Hadron Operators

Our computations are carried out using a cubic spatial lattice with periodic boundary conditions. To simplify our spectroscopy calculations, we construct our single-hadron operators such that they transform irreducibly under the symmetries of our lattice.

3.4.1 Symmetry Transformations on the Lattice

The allowed symmetry transformations on the lattice form the cubic space group known as O_h^1 in Schönflies notation, which is a semidirect product of spatial translations \mathbb{T} and orthogonal point group O_h . The spatial translation group \mathbb{T} is an Abelian group of discrete translations on the lattice. The orthogonal point group O_h contains the allowed rotation-reflection operations on the lattice. For a spatial rotation-reflection $R \in O_h$ about the origin and a discrete translation $\mathbf{b} \in \mathbb{T}$ on the lattice, our quark fields transform as

$$U_{(R,\mathbf{b})} q_{a\alpha j}^A(\mathbf{x}) U_{(R,\mathbf{b})}^\dagger = S(R)_{\alpha\beta}^{-1} q_{a\beta Rj}^A(R\mathbf{x}+\mathbf{b}), \quad (3.16)$$

$$U_{(R,\mathbf{b})} \bar{q}_{a\alpha j}^A(\mathbf{x}) U_{(R,\mathbf{b})}^\dagger = \bar{q}_{a\beta Rj}^A(R\mathbf{x}+\mathbf{b}) S(R)_{\beta\alpha}, \quad (3.17)$$

where $U_{(R,\mathbf{b})}$ represents the unitary quantum operator that carries out the transformation corresponding to the group element (R, \mathbf{b}) , and $S(R)$ is the transformation matrix for R in Dirac spin space. It can be shown that all elements of O_h can be generated from the products of C_{4y} , C_{4z} and I_s , where C_{nj} denotes a rotation of angle $2\pi/n$ about the j direction, and I_s denotes spatial inversion, as in Ref. [76]. The transformation matrices $S(R)$ for these generating-group elements are as follows:

$$S(C_{4y}) = \frac{1}{\sqrt{2}}(1 + \gamma_1\gamma_3), \quad S(C_{4z}) = \frac{1}{\sqrt{2}}(1 + \gamma_2\gamma_1), \quad S(I_s) = \gamma_4. \quad (3.18)$$

The matrices for all other group elements are simply products of the above generating matrices. For example, we have $C_{4x} = C_{4z}^{-1}C_{4y}C_{4z}$, and it is straightforward to show that $S(C_{4x}) = S(C_{4z})^{-1}S(C_{4y})S(C_{4z})$.

For hadrons moving with definite momentum $\mathbf{p} \neq 0$, the allowed symmetry operations are those which leave the momentum \mathbf{p} invariant. These symmetries make up the subgroup known as the *little group* of \mathbf{p} . For on-axis momenta, such as $\mathbf{p} = (0, 0, 1)$, the little group is C_{4v} . For planar-diagonal momenta, such as $\mathbf{p} = (0, 1, 1)$, the little

group is C_{2v} . For cubic-diagonal momenta, such as $\mathbf{p} = (1, 1, 1)$, the little group is C_{3v} . The details of these groups and their elements as used in this work can be found in Ref. [76].

Since our QCD action uses the approximation $m_u = m_d$, there is an extra $SU(2)$ isospin rotations symmetry that convert u quarks into d quarks, and *vice versa*. For mesonic systems with zero strangeness $S = 0$, there is an additional quantum number related to a symmetry known as G -parity. A G -parity transformation is defined by

$$U_G = U_C e^{-i\pi\tau_2}, \quad (3.19)$$

where C indicates charge conjugation, and τ_2 is the second generator of the isospin rotation operator. Under the G -parity operator, our building-blocks transform according to

$$U_G q_{a\alpha j}^A(x) U_G^\dagger = \bar{q}_{a\beta j}^B(x) (\gamma_2)_{\beta\alpha} G^{BA}, \quad (3.20)$$

$$U_G \bar{q}_{a\alpha j}^A(x) U_G^\dagger = (\gamma_2)_{\alpha\beta} q_{a\beta j}^B(x) G^{BA}, \quad (3.21)$$

using the Dirac-Pauli representation for the γ matrices. The transformation matrix G is nonzero only for $G^{ud} = -G^{du} = -G^{ss} = 1$.

For fermionic systems, such as baryons, double-valued representations are needed. Double-valued irreducible representations (irreps) of O_h can be obtained from the extra single-valued irreps of the so-called double point group O_h^D as described in Ref. [77].

3.4.2 Meson Elemental Operators

Our meson annihilation operators are composed of linear superpositions of so-called *elemental* operators of the form

$$\Phi_{\alpha\beta}^{AB}(t) = \sum_{\mathbf{x}} e^{-i\mathbf{p}\cdot(\mathbf{x} + \frac{1}{2}(\mathbf{d}_\alpha + \mathbf{d}_\beta))} \delta_{ab} \bar{q}_{a\alpha}^A(\mathbf{x}, t) q_{b\beta}^B(\mathbf{x}, t), \quad (3.22)$$

where q, \bar{q} are the gauge-covariantly-displaced LapH smeared quark fields defined in Eq. (3.14), $\mathbf{d}_\alpha, \mathbf{d}_\beta$ are the displacements of the quark fields \bar{q}, q , respectively, from \mathbf{x} . A, B are the flavor indices, and α, β are compound indices that include the spin components and displacement directions. The δ_{ab} term ensures the quark and an-

quark fields form a color singlet combination that is gauge invariant. The quark and antiquark displacements in the phase factor are required to ensure these elemental operators transform properly under G parity. Similar to the meson elemental annihilation operators, the meson elemental creation operators are defined by

$$\bar{\Phi}_{\alpha\beta}^{AB}(t) = \sum_{\mathbf{x}} e^{i\mathbf{p}\cdot(\mathbf{x}+\frac{1}{2}(\mathbf{d}_\alpha+\mathbf{d}_\beta))} \delta_{ab} \bar{q}_{b\beta}^B(\mathbf{x}, t) q_{a\alpha}^A(\mathbf{x}, t). \quad (3.23)$$

One can construct different elemental operators using different displacement types. Table. 3.1 lists the five types of displacements we use for the quark-antiquark combinations. To construct the single-site (SS) operators, one simply has to place the quark and antiquark operator on the same lattice site without any displacements. In a singly-displaced operator (SD), on the other hand, the quark is displaced from the antiquark along one of the lattice directions. If we further displace the antiquark in a lattice direction different from the displacement direction of the quark, making an L-shape configuration, we call this a doubly-displaced-L (DDL) operator. More complicated displacements can be constructed if one displaces the quark field twice in different directions and displaces the antiquark parallel or vertical to the plane of quark displacement “path”. These are called triply-displaced-U (TDU) operators for parallel antiquark displacements, and triply-displaced-O (TDO) operators for vertical quark displacements. Explicit expressions for these operator types are given in Table. 3.1. For simplicity, all of the displacement operators assume the same displacement length p for all meson operators. It turns out that $p = 3a_s$ is a good choice for our meson operators.

3.4.3 Baryon Elemental Operators

Baryon annihilation operators are superpositions of elemental operators that are compositions of three quark fields given by

$$\Phi_{\alpha\beta\gamma}^{ABC}(\mathbf{p}, t) = \sum_{\mathbf{x}} e^{-i\mathbf{p}\cdot\mathbf{x}} \varepsilon_{abc} q_{a\alpha}^A(\mathbf{x}, t) q_{b\beta}^B(\mathbf{x}, t) q_{c\gamma}^C(\mathbf{x}, t), \quad (3.24)$$


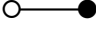
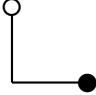
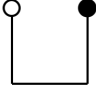
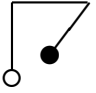
Illustration	Name	Explicit form ($ i \neq j \neq k \neq 0$)
	single-site	$\delta_{ab} \tilde{\chi}_{a\alpha}^A \tilde{\psi}_{b\beta}^B$
	singly-displaced	$\delta_{ab} \tilde{\chi}_{a\alpha}^A \left(\tilde{D}_j^{(p)} \tilde{\psi} \right)_{b\beta}^B$
	doubly-displaced-L	$\delta_{ab} \left(\tilde{\chi} \tilde{D}_j^{(p)\dagger} \right)_{a\alpha}^A \left(\tilde{D}_k^{(p)} \tilde{\psi} \right)_{b\beta}^B$
	triply-displaced-U	$\delta_{ab} \left(\tilde{\chi} \tilde{D}_j^{(p)\dagger} \right)_{a\alpha}^A \left(\tilde{D}_k^{(p)} \tilde{D}_j^{(p)} \tilde{\psi} \right)_{b\beta}^B$
	triply-displaced-O	$\delta_{ab} \left(\tilde{\chi} \tilde{D}_i^{(p)\dagger} \right)_{a\alpha}^A \left(\tilde{D}_j^{(p)} \tilde{D}_k^{(p)} \tilde{\psi} \right)_{b\beta}^B$

Table 3.1: The five types of displacements we use for our meson elementals are illustrated here. The smeared quark fields are represented by solid circles, the smeared barred antiquark fields by empty circles, and solid lines connecting them indicate displacement operators.

where the ε_{abc} term ensures that the three quark fields form a color singlet combination that is gauge invariant. The corresponding elemental creation operators have the form

$$\bar{\Phi}_{\alpha\beta\gamma}^{ABC}(\mathbf{p}, t) = \sum_{\mathbf{x}} e^{i\mathbf{p}\cdot\mathbf{x}} \varepsilon_{abc} \bar{q}_{c\gamma}^C(\mathbf{x}, t) \bar{q}_{b\beta}^B(\mathbf{x}, t) \bar{q}_{a\alpha}^A(\mathbf{x}, t). \quad (3.25)$$

We obtain single-site baryon operators by combining three quarks on the same lattice site without displacement. The singly-displaced operators have one quark displaced from the other two quarks. If two of the quarks are displaced in opposite directions, we obtain doubly-displaced-I (DDI) operators, and if two quarks are displaced in different directions, we produce doubly-displaced-L operators. All three quarks can be displaced from the color coupling site in orthogonal directions to form triply-displaced-O baryon operators. If the three quarks are displaced along three different directions


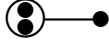

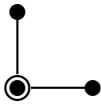
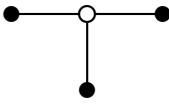
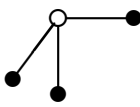
Illustration	Name	Explicit form ($ i \neq j \neq k $)
	single-site	$\varepsilon_{abc} \tilde{\psi}_{a\alpha}^A \tilde{\psi}_{b\beta}^B \tilde{\psi}_{c\gamma}^C$
	singly-displaced	$\varepsilon_{abc} \tilde{\psi}_{a\alpha}^A \tilde{\psi}_{b\beta}^B \left(\tilde{D}_j^{(p)} \tilde{\psi} \right)_{c\gamma}^C$
	doubly-displaced-I	$\varepsilon_{abc} \tilde{\psi}_{a\alpha}^A \left(\tilde{D}_{-j}^{(p)} \tilde{\psi} \right)_{b\beta}^B \left(\tilde{D}_j^{(p)} \tilde{\psi} \right)_{c\gamma}^C$
	doubly-displaced-L	$\varepsilon_{abc} \tilde{\psi}_{a\alpha}^A \left(\tilde{D}_j^{(p)} \tilde{\psi} \right)_{b\beta}^B \left(\tilde{D}_k^{(p)} \tilde{\psi} \right)_{c\gamma}^C$
	triply-displaced-T	$\varepsilon_{abc} \left(\tilde{D}_{-j}^{(p)} \tilde{\psi} \right)_{a\alpha}^A \left(\tilde{D}_j^{(p)} \tilde{\psi} \right)_{b\beta}^B \left(\tilde{D}_k^{(p)} \tilde{\psi} \right)_{c\gamma}^C$
	triply-displaced-O	$\varepsilon_{abc} \left(\tilde{D}_i^{(p)} \tilde{\psi} \right)_{a\alpha}^A \left(\tilde{D}_j^{(p)} \tilde{\psi} \right)_{b\beta}^B \left(\tilde{D}_k^{(p)} \tilde{\psi} \right)_{c\gamma}^C$

Table 3.2: The six types of displacements for our baryon elementals are illustrated here. The smeared quark fields are represented by solid circles, a hollow circle indicates a color ε_{abc} coupling, and the solid connecting lines indicate displacement operators.

in the same plane, triply-displaced-T (TDT) operators are produced. We choose $p = 2a_s$ as our displacement length for baryons. These displacement configurations are illustrated in Table 3.2.

3.4.4 Group-Theory Projections

In the previous two subsections, we defined the meson and baryon elemental operators. The elemental operators have the appropriate color and flavor structure, but they do not transform irreducibly under the O_h^1 lattice symmetry operations. We need to find

linear combinations of the elemental operators that do transform irreducibly. We express our hadron operators in the form

$$O_i^{\Lambda\lambda}(t) = c_{ij}^{\Lambda\lambda} \Phi_j(t), \quad \overline{O}_i^{\Lambda\lambda}(t) = c_{ij}^{\Lambda\lambda*} \overline{\Phi}_j(t), \quad (3.26)$$

where $\Phi_i(t)$ are the elemental operators defined in Eqs. (3.22) (3.24), and i represents all indices (spin, displacement directions, α, β , flavor A, B , momentum \mathbf{p} , and so on). We then require that our hadron operators transform under a symmetry operation R according to

$$U_R O_i^{\Lambda\lambda}(t) U_R^\dagger = \sum_{\mu} O_i^{\Lambda\mu}(t) \Gamma_{\mu\lambda}^{(\Lambda)}(R)^*, \quad (3.27)$$

$$U_R \overline{O}_i^{\Lambda\lambda}(t) U_R^\dagger = \sum_{\mu} O_i^{\Lambda\mu}(t) \Gamma_{\mu\lambda}^{(\Lambda)}(R), \quad (3.28)$$

where Λ denotes an irreducible representation, λ, μ indicate irrep rows, and $\Gamma_{\mu\nu}^{(\Lambda)}(R)$ is the representation matrix for group element R in irrep Λ .

In order to determine the coefficients $c_{ij}^{\Lambda\lambda}$ that produce irreducible operators, one can exploit a group-theoretical projection procedure. The procedure for baryon elemental operators is described in detail in Ref. [77], and can be easily generalized to meson operators. The procedure is summarized below.

Given a set of M linearly-independent elemental hadron operators $\{\Phi_i(t)\}$ at time t that transform among one another, we first obtain the $M \times M$ representation matrix $W_{ij}(R)$ that describes the transformation of the elemental operators $\Phi_i(t)$ under symmetry transformation R as

$$U_R \Phi_i(t) U_R^\dagger = \sum_{j=1}^M \Phi_j(t) W_{ji}(R), \quad (3.29)$$

$$U_R \overline{\Phi}_i(t) U_R^\dagger = \sum_{j=1}^M \overline{\Phi}_j(t) W_{ji}(R)^*. \quad (3.30)$$

We determine the transformations of the hadron elemental operators $U_R \Phi_i(t) U_R^\dagger$ from the transformations of the building-block quark fields using Eqs. (3.16) (3.17), and obtain the matrix $W_{ij}(R)$ using a Moore-Penrose pseudoinverse [78]. With this matrix $W_{ij}(R)$, the next step is to find a change of basis such that the representation

matrix is block diagonal, with the blocks matching the irreducible representation matrices of the symmetry group.

The following group-theoretical projections give us sets of operators that transform according to irrep Λ :

$$O_i^{\Lambda\lambda}(t) = \frac{d_\Lambda}{g_{\mathbb{G}^D}} \sum_{R \in \mathbb{G}^D} \Gamma_{\lambda\lambda}^{(\Lambda)}(R) U_R \Phi_i(t) U_R^\dagger, \quad (3.31)$$

where d_Λ is the dimension of the Λ irreducible representation, $g_{\mathbb{G}^D}$ is the number of elements in group \mathbb{G}^D . This gives us a projection matrix

$$P_{ij}^{\Lambda\lambda} = \frac{d_\Lambda}{g_{\mathbb{G}^D}} \sum_{R \in \mathbb{G}^D} \Gamma_{\lambda\lambda}^{(\Lambda)}(R) W_{ji}(R), \quad (3.32)$$

and the group-theoretical projected operators are $O_i^{\Lambda\lambda}(t) = \sum_j P_{ij}^{\Lambda\lambda} O_j(t)$. However, the resulting projected operators may not be all linearly independent. One final step is to choose suitable linear combinations of these projected operators to form independent hadron operators. A Gram-Schmidt procedure, as described in Ref. [77], yields the coefficients $c_{ij}^{\Lambda\lambda}$ for $i = 1, \dots, r$, for the r linearly independent hadron operators that we use.

The above procedure is used to construct the operators in the first row $\lambda = 1$ of irrep Λ . However, to increase statistics, we can also perform calculations using operators in the other irrep rows. The coefficients $c_{ij}^{\Lambda\mu}$ for $\mu \neq \lambda$ can be obtained from

$$c_{ik}^{\Lambda\mu} = \sum_{j=1}^M c_{ij}^{\Lambda\lambda} \frac{d_\Lambda}{g_{\mathbb{G}^D}} \sum_{R \in \mathbb{G}^D} \Gamma_{\mu\lambda}^{(\Lambda)}(R) W_{kj}(R), \quad (3.33)$$

using the previously-determined coefficients $c_{ij}^{\Lambda\lambda}$ for $\lambda = 1$.

Table 3.3 lists the irreducible representations of the double point group O_h^D . Here, A denotes the one-dimensional single-value irreps, E is used for two-dimensional irreps, and T indicates three-dimensional irreps. The spinor irreps used for fermions are labeled by G for two-dimensional irreps and H for four dimensional irreps. The subscripts g, u are used to label the parity, where g denotes even-parity and u denotes odd-parity. Note that parity is a symmetry only for $\mathbf{p} = 0$, since the parity operation reverses the direction of the momentum when $\mathbf{p} \neq 0$.

An alternative way to construct hadron operators of nonzero definite momentum

\mathbf{p} is to boost the zero-momentum irrep operators such that the resulting operators have momentum \mathbf{p} . In general, such operators will not transform irreducibly under the little group of \mathbf{p} , but rather, they carry a reducible representation. This reducible representation is said to be *subduced* from the irrep of O_h^D to the little group. The little group irrep content of the subduced representation can then be determined by the usual group-theory methods using character vectors. The so-called subductions of the O_h^D irreps onto the little groups C_{4v}^D , C_{2v}^D and C_{3v}^D are shown in Table 3.3.

$\Lambda(O_h^D)$	C_{4v}^D	C_{2v}^D	C_{3v}^D
A_{1g}	A_1	A_1	A_1
A_{1u}	A_2	A_2	A_2
A_{2g}	B_1	B_2	A_2
A_{2u}	B_2	B_1	A_1
E_g	$A_1 \oplus B_1$	$A_1 \oplus B_2$	E
E_u	$A_2 \oplus B_2$	$A_2 \oplus B_1$	E
T_{1g}	$A_2 \oplus E$	$A_2 \oplus B_1 \oplus B_2$	$A_2 \oplus E$
T_{1u}	$A_1 \oplus E$	$A_1 \oplus B_1 \oplus B_2$	$A_1 \oplus E$
T_{2g}	$B_2 \oplus E$	$A_1 \oplus A_2 \oplus B_1$	$A_1 \oplus E$
T_{2u}	$B_1 \oplus E$	$A_1 \oplus A_2 \oplus B_2$	$A_2 \oplus E$
$G_{1g/u}$	G_1	G	G
$G_{2g/u}$	G_2	G	G
$H_{g/u}$	$G_1 \oplus G_2$	$2G$	$F_1 \oplus F_2 \oplus G$

Table 3.3: The irreducible representations of O_h^D are listed, and the little group irrep content of their subductions to the little groups C_{4v}^D , C_{2v}^D , and C_{3v}^D are also presented.

The above operator construction is tedious and has been carried out using a well-tested MAPLE program. Our choices of the representation matrices $\Gamma^\Lambda(R)$ for all irreps Λ can be found in Ref. [76].

Ultimately, we are interested in the continuum limit. Thus, it would be useful to know which J irreps of the $SO(3)$ continuous group of rotations map into which irreps of the point group O . This can be determined by *subduction*. For each J irrep of $SO(3)$, we restrict the group elements to the subgroup of 24 elements contained in O and obtain the corresponding character vector. We can then use the orthogonality

relations to determine the number of times this subduced representation occurs in each irrep of O . Table 3.4 shows the subductions of the J irreps onto the irreps of the octahedral group O . This information will be needed to compare our lattice results with experimental measurements.

$\Lambda (O_h^D)$	Spin J irreps of $SU(2)$
A_{1g}, A_{1u}	0, 4, 6, 8, 9, ...
A_{2g}, A_{2u}	3, 6, 7, 9, ...
E_g, E_u	2, 4, 5, 6, 7, 8, 9, ...
T_{1g}, T_{1u}	1, 3, 4, 5, 6, 7, 8, 9, ...
T_{2g}, T_{2u}	2, 3, 4, 5, 6, 7, 8, 9, ...
G_{1g}, G_{1u}	$\frac{1}{2}, \frac{7}{2}, \frac{9}{2}, \frac{11}{2}, \frac{13}{2}, \frac{15}{2}, \dots$
G_{2g}, G_{2u}	$\frac{5}{2}, \frac{7}{2}, \frac{11}{2}, \frac{13}{2}, \frac{15}{2}, \dots$
H_g, H_u	$\frac{3}{2}, \frac{5}{2}, \frac{7}{2}, \frac{9}{2}, \frac{11}{2}, \frac{13}{2}, \frac{15}{2}, \dots$

Table 3.4: The continuum spin J irreps contained in each irrep Λ of O_h .

3.4.5 Flavor and G Parity Considerations

Because we use the approximation $m_u = m_d$, $SU(2)$ isospin rotations are an exact symmetry of our lattice QCD action. In the isospin formalism, the u and d quarks are regarded as two different states of a common object having total isospin $I = \frac{1}{2}$. The state $\bar{u}|0\rangle$ can be viewed as an eigenstate of the 3-projection of isospin with eigenvalue $I_3 = +\frac{1}{2}$, and $\bar{d}|0\rangle$ corresponds to an eigenstate with eigenvalue $I_3 = -\frac{1}{2}$.

Let τ_1, τ_2, τ_3 denote the three orthogonal generators of the isospin symmetry, and define $\tau_{\pm} = \tau_1 \pm i\tau_2$. The commutation relation of the operators τ_3, τ_{\pm} with the quark creation operators are given by

$$[\tau_3, \bar{O}_{I_3}^{(I)}] = I_3 \bar{O}_{I_3}^{(I)}, \quad (3.34)$$

$$[\tau_{\pm}, \bar{O}_{I_3}^{(I)}] = \sqrt{(I \mp I_3)(I \pm I_3 + 1)} \bar{O}_{I_3 \pm 1}^{(I)}, \quad (3.35)$$

$$[\tau_3, [\tau_3, \bar{O}_{I_3}^{(I)}]] + \frac{1}{2}[\tau_+, [\tau_-, \bar{O}_{I_3}^{(I)}]] + \frac{1}{2}[\tau_-, [\tau_+, \bar{O}_{I_3}^{(I)}]] = I(I+1) \bar{O}_{I_3}^{(I)}, \quad (3.36)$$

where $\overline{O}_{1/2}^{(1/2)} = \overline{u}$, $\overline{O}_{-1/2}^{(1/2)} = \overline{d}$, and $\overline{O}_0^{(0)} = \overline{s}$. Similarly, for the annihilation operators, we have

$$[\tau_3, O_{I_3}^{(I)}] = -I_3 O_{I_3}^{(I)}, \quad (3.37)$$

$$[\tau_{\pm}, O_{I_3}^{(I)}] = -\sqrt{(I \pm I_3)(I \mp I_3 + 1)} O_{I_3 \pm 1}^{(I)}, \quad (3.38)$$

$$[\tau_3, [\tau_3, O_{I_3}^{(I)}]] + \frac{1}{2}[\tau_+, [\tau_-, O_{I_3}^{(I)}]] + \frac{1}{2}[\tau_-, [\tau_+, O_{I_3}^{(I)}]] = I(I+1) O_{I_3}^{(I)}. \quad (3.39)$$

These relations are useful for constructing the flavor content of our hadron operators. In fact, the above relations are not restricted to just the u and d quark operators, but apply to any set of hadron operators $O_{I_3}^{(I)}$ with definite isospin I and I_3 .

Now consider single-baryon operators, which are composed of three quark-field operators. We restrict our attention to the u , d , and s quarks. Combining three light-quark operators forms either $I = \frac{3}{2}$ operators that create Δ baryons or $I = \frac{1}{2}$ operators that create nucleon (N) states. Combining two light quark fields with one s quark operator produces either $I = 1$ operators that create Σ baryons or $I = 0$ operators that create Λ baryons. Two s quark operators with one light quark produce $I = \frac{1}{2}$ operators that create Ξ baryons, and three s quarks form $I = 0$ operators that create the Ω baryons.

For the N and Δ sectors, there are actually eight flavor combinations of u and d quarks: four of them correspond to $I = \frac{3}{2}$ states with $I_3 = \frac{3}{2}, \frac{1}{2}, -\frac{1}{2}, -\frac{3}{2}$, two other combinations correspond to two states with total isospin $I = \frac{1}{2}$ and $I_3 = \frac{1}{2}$, and the remaining two combinations form $I = \frac{1}{2}$ and $I_3 = -\frac{1}{2}$ states. The redundancy comes from the two ways to build an $I = \frac{1}{2}$ state since the first two quarks can form an isospin singlet or triplet state. Similarly, for the Λ and Σ sectors, four combinations of light quarks form three $I = 1$ states and one $I = 0$ state, keeping in mind that the s quark does not change flavor under isospin rotation. Using Eq. (3.34) to Eq. (3.39) with the above flavor considerations, we can determine the proper Clebsch-Gordan coefficients for these operator combinations. Our choice of baryon flavor-structure can be found in Table 3.5. Since the electromagnetic interaction is ignored in our calculations, states with the same I but different I_3 are expected to have the same energies. The calculation of the hadron spectrum only needs to include operators with the highest I_3 value. Note that when constructing multi-hadron operators, other I_3 values of the individual single-hadron operators are needed.

A single-meson operator is an assemblage of a quark-antiquark pair. For u, d, s

quarks, there are a total of nine flavor combinations, and four of them involve only combinations of the light u, d quarks. These four combinations form three $I = 1$ states with $I_3 = 1, 0, -1$, and one $I = 0$ state with $I_3 = 0$. Conventionally, $I = 1$ states are called *isovector* mesons. The $I = 0$ states (such as $\eta, \omega \dots$) are called *isoscalar* mesons. There are four other flavor combinations that involve one light quark and one strange quark. Two of them are isospin $I = \frac{1}{2}$ and strangeness $S = 1$ states with $I_3 = \frac{1}{2}, -\frac{1}{2}$, called *kaons*. The other two states with strangeness $S = -1$ are antikaon states; we use K^c to denote their annihilation operators. These antikaon operators are needed when constructing kaon-antikaon multi-hadron states. The K and K^c operators are related by a G -parity transformation. Our choices of meson flavor structures are summarized in Table 3.5. To simplify notation, we always assume the first quark A in the notation $\Phi_{\alpha\beta}^{AB}$ is the barred field operator.

Quark flavor combinations are often chosen to transform irreducibly under flavor $SU(3)$ transformations due to the approximate $SU(3)$ symmetry of u, d, s quarks. However, in this work, we construct hadron operators that respect only the isospin symmetry involving the u, d quarks. The states that transform irreducibly under $SU(3)$ are simply linear combinations of operators formed using $SU(2)$ flavor structure. For example, the η meson is often considered to be created by an operator of the form $\bar{u}u + \bar{d}d + \bar{s}s$. However, we can compute the isoscalar operator with flavor content $\bar{u}u + \bar{d}d$ and $\bar{s}s$ separately, then allow these operators to mix in the correlation matrix.

Meson operators with zero strangeness $S = 0$ have an additional symmetry known as G parity. Such operators can be either symmetric or antisymmetric under a G -parity transformation, and are constructed using

$$O^{\Lambda^\eta} = O^\Lambda + \eta U_G O^\Lambda U_G^\dagger, \quad (3.40)$$

where U_G represents the G -parity operator as defined in Eq. (3.19), and $\eta = +1$ for positive G -parity operators and $\eta = -1$ for negative G -parity operators. The operator O^Λ refers to a zero-strangeness meson operator designed without taking G -parity into consideration. We use a superscript label “+” for an irrep spanned by states that are even under G parity and “−” for odd G -parity irreps. For example, the irrep A_{1u} can be projected into two irreps A_{1u}^+ and A_{1u}^- with positive and negative G -parities, respectively.

Operator	I	I_3	S	Annihilation Operators	PDG Name
$N_{\frac{1}{2}}$	$\frac{1}{2}$	$\frac{1}{2}$	0	$c_{\alpha\beta\gamma}^{(l)}(\Phi_{\alpha\beta\gamma}^{uud} - \Phi_{\alpha\beta\gamma}^{duu})$	N^+, p
$N_{-\frac{1}{2}}$	$\frac{1}{2}$	$-\frac{1}{2}$	0	$c_{\alpha\beta\gamma}^{(l)}(\Phi_{\alpha\beta\gamma}^{udd} - \Phi_{\alpha\beta\gamma}^{ddu})$	N^0, n
$\Delta_{\frac{3}{2}}$	$\frac{3}{2}$	$\frac{3}{2}$	0	$c_{\alpha\beta\gamma}^{(l)} \Phi_{\alpha\beta\gamma}^{uuu}$	Δ^{++}
$\Delta_{\frac{1}{2}}$	$\frac{3}{2}$	$\frac{1}{2}$	0	$\frac{1}{\sqrt{3}} c_{\alpha\beta\gamma}^{(l)}(\Phi_{\alpha\beta\gamma}^{uud} + \Phi_{\alpha\beta\gamma}^{udu} + \Phi_{\alpha\beta\gamma}^{duu})$	Δ^+
$\Delta_{-\frac{1}{2}}$	$\frac{3}{2}$	$-\frac{1}{2}$	0	$\frac{1}{\sqrt{3}} c_{\alpha\beta\gamma}^{(l)}(\Phi_{\alpha\beta\gamma}^{ddu} + \Phi_{\alpha\beta\gamma}^{dud} + \Phi_{\alpha\beta\gamma}^{udd})$	Δ^0
$\Delta_{-\frac{3}{2}}$	$\frac{3}{2}$	$-\frac{3}{2}$	0	$c_{\alpha\beta\gamma}^{(l)} \Phi_{\alpha\beta\gamma}^{ddd}$	Δ^-
Λ_0	0	0	-1	$c_{\alpha\beta\gamma}^{(l)}(\Phi_{\alpha\beta\gamma}^{uds} - \Phi_{\alpha\beta\gamma}^{dus})$	Λ^0
Σ_1	1	1	-1	$c_{\alpha\beta\gamma}^{(l)} \Phi_{\alpha\beta\gamma}^{uus}$	Σ^+
Σ_0	1	0	-1	$\frac{1}{\sqrt{2}} c_{\alpha\beta\gamma}^{(l)}(\Phi_{\alpha\beta\gamma}^{uds} + \Phi_{\alpha\beta\gamma}^{dus})$	Σ^0
Σ_{-1}	1	-1	-1	$c_{\alpha\beta\gamma}^{(l)} \Phi_{\alpha\beta\gamma}^{dds}$	Σ^-
$\Xi_{\frac{1}{2}}$	$\frac{1}{2}$	$\frac{1}{2}$	-2	$c_{\alpha\beta\gamma}^{(l)} \Phi_{\alpha\beta\gamma}^{ssu}$	Ξ^0
$\Xi_{-\frac{1}{2}}$	$\frac{1}{2}$	$-\frac{1}{2}$	-2	$c_{\alpha\beta\gamma}^{(l)} \Phi_{\alpha\beta\gamma}^{ssd}$	Ξ^-
Ω_0	0	0	-3	$c_{\alpha\beta\gamma}^{(l)} \Phi_{\alpha\beta\gamma}^{sss}$	Ω^-
η_0	0	0	0	$c_{\alpha\beta}^{(l)}(\Phi_{\alpha\beta}^{uu} + \Phi_{\alpha\beta}^{dd})$	$\eta, \eta', f, h, \omega$
ϕ_0	0	0	0	$c_{\alpha\beta}^{(l)} \Phi_{\alpha\beta}^{ss}$	$\eta, \eta', f, h, \omega$
π_1	1	1	0	$c_{\alpha\beta}^{(l)} \Phi_{\alpha\beta}^{du}$	$\pi^+, b, \rho, a,$
π_0	1	0	0	$-\frac{1}{\sqrt{2}} c_{\alpha\beta}^{(l)}(\Phi_{\alpha\beta}^{uu} - \Phi_{\alpha\beta}^{dd})$	π^0
π_{-1}	1	-1	0	$-c_{\alpha\beta}^{(l)} \Phi_{\alpha\beta}^{ud}$	π^-
$K_{\frac{1}{2}}$	$\frac{1}{2}$	$\frac{1}{2}$	1	$c_{\alpha\beta}^{(l)} \Phi_{\alpha\beta}^{su}$	K^+
$K_{-\frac{1}{2}}$	$\frac{1}{2}$	$-\frac{1}{2}$	1	$c_{\alpha\beta}^{(l)} \Phi_{\alpha\beta}^{sd}$	K^-
$K_{\frac{1}{2}}^c$	$\frac{1}{2}$	$\frac{1}{2}$	-1	$c_{\alpha\beta}^{(l)} \Phi_{\alpha\beta}^{ds}$	-
$K_{-\frac{1}{2}}^c$	$\frac{1}{2}$	$-\frac{1}{2}$	-1	$-c_{\alpha\beta}^{(l)} \Phi_{\alpha\beta}^{us}$	-

Table 3.5: The flavor structures of our single-hadron annihilation operators. The subscripts in the hadron labels of the first column indicate I_3 . The last column shows the particle names as given in by Particle Data Group [6]. To simplify notation, we always assume the first quark A in $\Phi_{\alpha\beta}^{AB}$ is the barred field in the meson operator. G -parity projections for the zero-strangeness mesons are not shown.

3.4.6 Summary of Single-Hadron Operators

To summarize, the single-hadron operators which we construct can be expressed as $O_{\mathbf{p}\Lambda\lambda i}^{II_3 S}(t)$, with total isospin I , isospin projection I_3 , strangeness S , momentum \mathbf{p} , irrep Λ including G -parity when necessary, irrep row λ , and an extra identifier i for all other identifying information, such as displacement type, and so on. These operators transform under lattice translations, rotations, and reflections according to

$$\begin{aligned} U_{(R,\mathbf{b})} O_{\mathbf{p}\Lambda\lambda i}^{II_3 S}(t) U_{(R,\mathbf{b})}^\dagger &= O_{R\mathbf{p}\Lambda\mu i}^{II_3 S}(t) \Gamma_{\mu\lambda}^{(\Lambda)}(R_W^\mathbf{p})^* e^{i\mathbf{b}\cdot R\mathbf{p}}, \\ U_{(R,\mathbf{b})} \overline{O}_{\mathbf{p}\Lambda\lambda i}^{II_3 S}(t) U_{(R,\mathbf{b})}^\dagger &= \overline{O}_{R\mathbf{p}\Lambda\mu i}^{II_3 S}(t) \Gamma_{\mu\lambda}^{(\Lambda)}(R_W^\mathbf{p}) e^{-i\mathbf{b}\cdot R\mathbf{p}}, \end{aligned} \quad (3.41)$$

where the Wigner rotation is the element of the little group of \mathbf{p} given by

$$R_W^\mathbf{p} = (R_{\text{ref}}^{R\mathbf{p}})^{-1} R R_{\text{ref}}^\mathbf{p}. \quad (3.42)$$

In the above expression, one must first pick a reference momentum \mathbf{p}_{ref} , then for any required momentum \mathbf{p} , phases are determined by choosing a reference rotation $R_{\text{ref}}^\mathbf{p}$ that rotates the reference momentum into \mathbf{p} . These operators transform under an isospin rotation R_τ according to

$$\begin{aligned} U_{R_\tau} O_{\mathbf{p}\Lambda\lambda i}^{II_3 S}(t) U_{R_\tau}^\dagger &= O_{\mathbf{p}\Lambda\lambda i}^{II_3 S}(t) D_{I_3' I_3}^{(I)}(R_\tau)^*, \\ U_{R_\tau} \overline{O}_{\mathbf{p}\Lambda\lambda i}^{II_3 S}(t) U_{R_\tau}^\dagger &= \overline{O}_{\mathbf{p}\Lambda\lambda i}^{II_3 S}(t) D_{I_3' I_3}^{(I)}(R_\tau), \end{aligned} \quad (3.43)$$

where $D^{(I)}(R_\tau)$ are the rotation matrices of isospin. Under G parity, these operators transform as

$$\begin{aligned} U_G O_{\mathbf{p}\Lambda\lambda i}^{II_3, S}(t) U_G^\dagger &= \eta_\Lambda O_{\mathbf{p}\Lambda\lambda i}^{II_3, -S}(t), \\ U_G \overline{O}_{\mathbf{p}\Lambda\lambda i}^{II_3, S}(t) U_G^\dagger &= \eta_\Lambda \overline{O}_{\mathbf{p}\Lambda\lambda i}^{II_3, -S}(t), \end{aligned} \quad (3.44)$$

where $\eta_\Lambda = \pm 1$ for even or odd G parity operators.

3.5 Multi-hadron Operators

In this work, our goal is to determine the low-lying spectrum of the stationary states of QCD. In some channels, single-hadron states dominate the lowest lying states.

However, in most channels, multi-hadron states are expected to have lower energies than the single-hadron states. The use of good multi-hadron operators is necessary for extracting the energies of such states. In this work, we restrict attention to only two-meson and meson-baryon systems. Generalization to three hadron systems can be done using the same methods described below.

With the single-hadron operators $O_{\mathbf{p}\Lambda\lambda i}^{II_3 S}(t)$ and their transformation properties defined in Eq. (3.42), Eq. (3.43) and Eq. (3.44), we can construct two-hadron annihilation elemental operators as combinations of two single-hadron operators as

$$O_{\mathbf{p}_a \Lambda_a \lambda_a i_a}^{I_a I_{3a} S_a} O_{\mathbf{p}_b \Lambda_b \lambda_b i_b}^{I_b I_{3b} S_b}, \quad (3.45)$$

where a, b represent the separate single hadrons. We then need to find the linear combinations of such two-hadron elemental operators that transform irreducibly under all lattice symmetries.

3.5.1 Group-Theory Projections

The transformation properties of the single-hadron operators are defined in Eq. (3.42) to Eq. (3.44). We start by considering combinations of two-hadron operators that annihilate the same total momentum $\mathbf{p} = \mathbf{p}_a + \mathbf{p}_b$, then we identify the little group that leaves \mathbf{p} invariant.

For any transformation R that is an element of the symmetry group of the lattice, the irreps of the individual single-hadron operators in the two-hadron elemental operators do not change, nor do the displacement types, and so on. In other words, $\Lambda_a, \Lambda_b, i_a, i_b$ are invariant under R . However, the irrep row λ_a, λ_b are not invariant. The separate momentum \mathbf{p}_a and \mathbf{p}_b will also change to different momentum directions $R\mathbf{p}_a$ and $R\mathbf{p}_b$. Therefore, our irreducible two-particle operators have the form

$$O_{\mathbf{p}}^{\Lambda\lambda i} = g_{\mathbf{p}_a \lambda_a \mathbf{p}_b \lambda_b}^{\Lambda\lambda} O_{\mathbf{p}_a \lambda_a}^{\Lambda_a i_a} O_{\mathbf{p}_b \lambda_b}^{\Lambda_b i_b}, \quad (3.46)$$

keeping fixed $\mathbf{p} = \mathbf{p}_a + \mathbf{p}_b$. The index i in $O_{\mathbf{p}}^{\Lambda\lambda i}$ here is a compound index that includes $(\Lambda_a, i_a, \Lambda_b, i_b)$. The coefficients $g_{\mathbf{p}_a \lambda_a \mathbf{p}_b \lambda_b}^{\Lambda\lambda}$ are again obtained using group theoretical projections as described in Sec. 3.4.4. These are computed using MAPLE. Flavor indices and G -parity are ignored here since they do not change under O_h^1 transformations (rotations and reflections).

3.5.2 Flavor Consideration of Multi-hadrons

We have already constructed the flavor structures of our single-hadron operators with different isospin I and I_3 in Sec. 3.4.5, which are summarized in Table 3.5. Here, we use these flavor structures as our building blocks for the multi-hadron operator flavor structures.

First, consider the *bosonic* sector. Using the single-hadron operators in Table 3.5, we can produce two-meson states with total strangeness $S = 0$ with total isospin $I = 0, 1, 2$, as well as $S = 1$ states with $I = \frac{1}{2}, \frac{3}{2}$, and $S = 2$ states with $I = 0, 1$. The different flavor combinations that must be considered are summarized in Table 3.6. In this table, π refers to *any* isovector quark-antiquark meson operator with flavor content such as $\bar{d}u$ (such as a , b , π , and ρ mesons), η refers to any $\bar{u}u + \bar{d}d$ isoscalar meson operator, ϕ refers to any $\bar{s}s$ isoscalar meson operator, K refers to any quark-antiquark operator having flavor content $\bar{s}u$ or $\bar{s}d$ such that its strangeness is $S = 1$, and K^c is any quark-antiquark operator having flavor content $\bar{u}s$ or $\bar{d}s$ such that its strangeness is $S = -1$. Since the energy spectrum is independent of total I_3 , we only study sectors with maximal total $I_3 = I$ in this work. Note that various values of I_3 are needed for the individual mesons used to construct the two-meson operators. The QCD stationary-state energies do not depend on the sign of the total strangeness, so we focus only on sectors involving non-negative strangeness. For *fermionic* sectors, the different flavor combinations that must be considered are summarized in Table 3.7. Only sectors of zero or negative total strangeness are investigated.

Determining the two-meson flavor combinations that transform irreducibly under isospin rotations follows the same procedure using Eq. (3.34) to Eq. (3.39), as described in Sec. 3.4.5. Individual meson operators of different I_3 values are required to construct such multi-hadron operators. For example, consider the combination of two π -type operators. For a single π , there are $I_3 = 1, 0, -1$ states, denoted by π_1, π_0, π_{-1} , respectively. Using Eq. (3.34) to Eq. (3.39), the $\pi\pi$ combinations that transform irreducibly under isospin rotations are

$$\begin{aligned} \pi_1\pi_1 & \quad \text{for} \quad I = I_3 = 2, \\ \pi_1\pi_0 - \pi_0\pi_1 & \quad \text{for} \quad I = I_3 = 1, \\ \pi_1\pi_{-1} - \pi_0\pi_0 + \pi_{-1}\pi_1 & \quad \text{for} \quad I = I_3 = 0. \end{aligned}$$

Consideration of G parity is required for operators in bosonic sectors with $S = 0$.

The G parities of single-meson operators were already discussed in Sec. 3.4.5. Using the single-meson operators of definite G parity to construct two-meson operators of definite G parity is straightforward. Combinations of two single-meson operators of the same G parity produces even G -parity two-meson operators, whereas combinations of two single-meson operators of opposite G parity results in odd G -parity two-meson operators. Special care needs to be taken when considering the kaon-antikaon states with total strangeness $S = 0$. By construction, the flavor combination of KK^c does not have definite G parity since under a G parity transformation U_G :

$$\begin{aligned} U_G K U_G^\dagger &= K^c, \\ U_G K^c U_G^\dagger &= -K. \end{aligned}$$

We can use the same G -parity projection technique as defined in Eq. (3.40) to construct kaon-antikaon operators of definite G parity.

$I = I_3$	S	Flavor Content
0	0	$\eta, \phi, G, \eta\eta, \eta\phi, \phi\phi, \pi\pi, KK^c$
1	0	$\pi, \pi\pi, \eta\pi, \phi\pi, KK^c$
2	0	$\pi\pi$
$\frac{1}{2}$	1	$K, K\pi, K\eta, K\phi$
$\frac{3}{2}$	1	$K\pi$
0	2	KK
1	2	KK

Table 3.6: The flavor content for bosonic states of single meson or meson-meson state categorized by total isospin I and strangeness S . Here, π refers to *any* isovector quark-antiquark meson operator with flavor content such as $\bar{d}u$ (such as a, b, π , and ρ mesons), η refers to any $\bar{u}u + \bar{d}d$ isoscalar meson operator, ϕ refers to any $\bar{s}s$ isoscalar meson operator, K refers to any quark-antiquark operator having flavor content $\bar{s}u$ or $\bar{s}d$ such that its strangeness is $S = 1$, and K^c is any quark-antiquark operator having flavor content $\bar{u}s$ or $\bar{d}s$ such that its strangeness is $S = -1$.

$I = I_3$	S	Flavor Content
$\frac{1}{2}$	0	$N, N\eta, N\phi, N\pi, \Delta\pi, \Lambda K, \Sigma K$
$\frac{3}{2}$	0	$\Delta, \Delta\eta, \Delta\phi, \Delta\pi, N\pi, \Sigma K$
$\frac{5}{2}$	0	$\Delta\pi$
0	-1	$\Lambda, \Lambda\eta, \Lambda\phi, NK^c, \Sigma\pi, \Xi K$
1	-1	$\Sigma, \Sigma\eta, \Sigma\phi, \Sigma\pi, NK^c, \Delta K^c, \Lambda\pi, \Xi K$
2	-1	$\Delta K^c, \Sigma\pi$
$\frac{1}{2}$	-2	$\Xi, \Lambda K^c, \Xi\eta, \Xi\phi, \Xi\pi, \Sigma K^c, \Omega K$
$\frac{3}{2}$	-2	$\Sigma K^c, \Xi\pi$
0	-3	$\Omega, \Xi K^c, \Omega\eta, \Omega\phi$
1	-3	$\Omega\pi, \Xi K^c$

Table 3.7: The flavor content for fermionic states as the combination of single baryon or meson-baryon state categorized by total isospin I and strangeness S . Here, π refers to *any* isovector quark-antiquark meson operator with flavor content such as $\bar{d}u$ (such as a , b , π , and ρ mesons), η refers to any $\bar{u}u + \bar{d}d$ isoscalar meson operator, ϕ refers to any $\bar{s}s$ isoscalar meson operator, K refers to any quark-antiquark operator having flavor content $\bar{s}u$ or $\bar{s}d$ such that its strangeness is $S = 1$, and K^c is any quark-antiquark operator having flavor content $\bar{u}s$ or $\bar{d}s$ such that its strangeness is $S = -1$.

Chapter 4

Hadronic Correlators

Hadron correlation functions are ratios of path integrals

$$\begin{aligned}
 C_{ij}(t_F - t_0) &= \langle 0 | O_i(t_F) \bar{O}_j(t_0) | 0 \rangle \\
 &= \frac{\int \mathcal{D}(\chi, \psi, U) O_i[\chi(t), \psi(t), U(t)] \bar{O}_j[\chi(t_0), \psi(t_0), U(t_0)] \exp(-\chi \Omega[U] \psi - S_G[U])}{\int \mathcal{D}(\chi, \psi, U) \exp(-\chi \Omega[U] \psi - S_G[U])},
 \end{aligned} \tag{4.1}$$

where $\chi \equiv \bar{\psi} \gamma_4$, $\Omega = \gamma_4 K$, and K is the Dirac matrix. The O_i and \bar{O}_j meson/baryon operators are combinations of the gauge-covariantly-displaced LapH smeared quark fields q^A and \bar{q}^A , defined in Eq. (3.14) by

$$q_{a\alpha j}^A = D^{(j)} \tilde{\psi}_{a\alpha}^{(A)}, \quad \bar{q}_{a\alpha j}^A = \tilde{\bar{\psi}}_{a\alpha}^{(A)} \gamma_4 D^{(j)\dagger} = \tilde{\chi}_{a\alpha}^{(A)} D^{(j)\dagger}, \tag{4.2}$$

where $D^{(j)}$ is the displacement of type j defined in Eq. (3.15). To evaluate path integrals of the type shown above, we first integrate over the Grassmann-valued quark fields. The quark fields appear quadratically in the action, so the integrals over the quark fields can be done exactly. The remaining integration over the gauge-field (link variables) is estimated using the Monte Carlo method. In this chapter, we discuss how we evaluate our estimates of the hadronic correlation functions.

First, integration over the quark fields is discussed in Sec. 4.1, which leads to the concept of quark lines describing propagation of the quarks. Our method of estimating the quark lines using the stochastic LapH method is then described in Sec. 4.2. This method exploits stochastic estimates of the inverse of the Dirac matrix, with variance

reduction through noise dilution. Correlator evaluations using the stochastic LapH method are then detailed in Sec. 4.3.

4.1 Quark Propagators and the LapH Subspace

To proceed, a brief review of Grassmann variables is helpful. Grassmann variables mutually anticommute. Let ψ_a and $\bar{\psi}_a$ denote a set of $2N$ independent Grassmann variables, for $a = 1, \dots, N$. These variables satisfy the following properties:

- Mutually anticommute: $\psi_a \psi_b + \psi_b \psi_a = 0$, $\psi_a \bar{\psi}_b + \bar{\psi}_b \psi_a = 0$, $\bar{\psi}_a \bar{\psi}_b + \bar{\psi}_b \bar{\psi}_a = 0$.
- Vanishing squares: $\psi_a^2 = \bar{\psi}_a^2 = 0$.
- Commute with ordinary numbers: $x \psi_a = \psi_a x$ where x is an ordinary real or complex number.
- Zero is considered both an ordinary c -number and a Grassmann variable.
- A product of an even number of Grassmann variables commutes with all *other* Grassmann variables.
- A product of an odd number of Grassmann variables anticommutes with all *other* Grassmann variables.

Differentiation is defined by

$$\frac{\partial \psi_b}{\partial \psi_a} = \delta_{ab}.$$

The chain rule must be carefully applied taking signs into account:

$$\begin{aligned} \frac{\partial}{\partial \psi_a}(\psi_b \psi_c \psi_d) &= \frac{\partial \psi_b}{\partial \psi_a} \psi_c \psi_d - \psi_b \frac{\partial \psi_c}{\partial \psi_a} \psi_d + \psi_b \psi_c \frac{\partial \psi_d}{\partial \psi_a} \\ &= \delta_{ab} \psi_c \psi_d - \delta_{ac} \psi_b \psi_d + \delta_{ad} \psi_b \psi_c. \end{aligned}$$

We also have

$$\begin{aligned} \frac{\partial}{\partial \psi_a} \psi_b &= \delta_{ab}, & \frac{\partial}{\partial \psi_a} \bar{\psi}_b &= 0, \\ \frac{\partial}{\partial \bar{\psi}_a} \bar{\psi}_b &= \delta_{ab}, & \frac{\partial}{\partial \bar{\psi}_a} \psi_b &= 0, \end{aligned}$$

$$\frac{\partial}{\partial \psi_a}(\bar{\psi}_b \psi_c) = -\bar{\psi}_b \delta_{ac} \quad \frac{\partial}{\partial \bar{\psi}_a}(\bar{\psi}_b \psi_c) = \psi_c \delta_{ab}.$$

Given that $\psi_a^2 = \bar{\psi}_a^2 = 0$, then for an $N \times N$ matrix A of ordinary c -numbers,

$$\exp(\bar{\psi}^T A \psi) = 1 + \bar{\psi}^T A \psi + \frac{1}{2!} (\bar{\psi}^T A \psi)^2 + \cdots + \frac{1}{N!} (\bar{\psi}^T A \psi)^N,$$

and it is not difficult to show that

$$\frac{\partial}{\partial \psi_a} e^{\bar{\psi}^T A \psi} = -\bar{\psi}_b A_{ba} e^{\bar{\psi}^T A \psi}, \quad (4.3)$$

$$\frac{\partial}{\partial \bar{\psi}_a} e^{\bar{\psi}^T A \psi} = A_{ab} \psi_b e^{\bar{\psi}^T A \psi}. \quad (4.4)$$

Because Grassmann numbers are neither ordinal nor quantal, integration cannot be understood in terms of a Riemann sum nor as a definite integral with limits of integration. Integration is defined by

$$\begin{aligned} \int d\psi_a &= 0, & \int d\bar{\psi}_a &= 0, & \int d\psi_a \psi_b &= \delta_{ab}, & \int d\bar{\psi}_a \bar{\psi}_b &= \delta_{ab}, \\ \int d\psi_a \bar{\psi}_b &= 0, & \int d\bar{\psi}_a \psi_b &= 0, & \int d\bar{\psi}_a d\psi_b \bar{\psi}_c \psi_d &= -\int (d\bar{\psi}_a \bar{\psi}_c)(d\psi_b \psi_d) = -\delta_{ac} \delta_{bd}, \end{aligned}$$

so as to respect translational invariance, that is, invariance under a shift of integration variable. Note that the differential is a Grassmann variable $\{d\psi_a, \psi_b\} = 0$, so that in performing multi-dimensional integrals, one must carefully re-order the variables to get each variable next to its differential:

$$\int d\psi_a d\psi_b \psi_c \psi_b \psi_a = - \int (d\psi_a \psi_a) d\psi_b \psi_c \psi_b = \int (d\psi_a \psi_a)(d\psi_b \psi_b) \psi_c = \psi_c.$$

Now consider the integral:

$$\int \left(\prod_{a=1}^N d\bar{\psi}_a d\psi_a \right) \exp \left(- \sum_{b,c=1}^N \bar{\psi}_b M_{bc} \psi_c - \sum_{b=1}^N \bar{\psi}_b \xi_b - \sum_{b=1}^N \bar{\xi}_b \psi_b \right),$$

where M is a diagonalizable and invertible $N \times N$ matrix of ordinary numbers and $\bar{\xi}_b, \xi_b$ are Grassmann variables. Shift the variables of integration

$$\psi_a = \varrho_a - M_{ab}^{-1} \xi_b, \quad \bar{\psi}_a = \bar{\varrho}_a - \bar{\xi}_b M_{ba}^{-1},$$

then the integral becomes

$$\int \left(\prod_{a=1}^N d\bar{\varrho}_a d\varrho_a \right) \exp \left(- \sum_{b,c=1}^N \bar{\varrho}_b M_{bc} \varrho_c \right) \exp \left(\sum_{b,c=1}^N \bar{\xi}_b M_{bc}^{-1} \xi_c \right).$$

Now write $M = V \Lambda^M V^{-1}$, where Λ^M is a diagonal matrix, and do another change of variables of integration: $\varrho_a = V_{ab} \nu_b$, $\bar{\varrho}_a = \bar{\nu}_b V_{ba}^{-1}$, to obtain

$$\prod_{a=1}^N \left(\int d\bar{\nu}_a d\nu_a e^{-\bar{\nu}_a \Lambda_{aa}^M \nu_a} \right) \exp \left(\sum_{b,c=1}^N \bar{\xi}_b M_{bc}^{-1} \xi_c \right) = \det M \exp \left(\bar{\xi}^T M^{-1} \xi \right).$$

So to summarize,

$$\int \mathcal{D}(\bar{\psi}, \psi) \exp \left(-\bar{\psi}^T M \psi - \bar{\psi}^T \xi - \bar{\xi}^T \psi \right) = \det M \exp \left(\bar{\xi}^T M^{-1} \xi \right). \quad (4.5)$$

We can now use Eqs. (4.3) and (4.4) with Eq. (4.5) to evaluate integrals of the form

$$\int \mathcal{D}(\bar{\psi}, \psi) \psi_{a_1} \dots \psi_{a_n} \bar{\psi}_{b_1} \dots \bar{\psi}_{b_m} \exp \left(-\bar{\psi}^T M \psi \right).$$

For example,

$$\int \mathcal{D}(\bar{\psi}, \psi) \psi_a \exp \left(-\bar{\psi}^T M \psi \right) = 0.$$

The Feynman propagator is related to the following integral:

$$\int \mathcal{D}(\bar{\psi}, \psi) \psi_a \bar{\psi}_b \exp \left(-\bar{\psi}^T M \psi \right) = M_{ab}^{-1} \det M.$$

Another example is

$$\int \mathcal{D}(\bar{\psi}, \psi) \psi_a \psi_b \bar{\psi}_c \bar{\psi}_d \exp \left(-\bar{\psi}^T M \psi \right) = (M_{ad}^{-1} M_{bc}^{-1} - M_{ac}^{-1} M_{bd}^{-1}) \det M.$$

Similarly, one finds that the only integrals of the type above which do not vanish are those consisting of an equal number of ψ and $\bar{\psi}$ variables. For the three-quark baryon operators, the Grassmann integral of most relevance is

$$\begin{aligned} & \int \mathcal{D}(\bar{\psi}, \psi) \psi_{a_1} \psi_{a_2} \psi_{a_3} \bar{\psi}_{b_1} \bar{\psi}_{b_2} \bar{\psi}_{b_3} \exp \left(-\bar{\psi}^T M \psi \right) \\ &= \left(-M_{a_1 b_1}^{-1} M_{a_2 b_2}^{-1} M_{a_3 b_3}^{-1} + M_{a_1 b_1}^{-1} M_{a_2 b_3}^{-1} M_{a_3 b_2}^{-1} + M_{a_1 b_2}^{-1} M_{a_2 b_1}^{-1} M_{a_3 b_3}^{-1} \right. \\ & \quad \left. - M_{a_1 b_2}^{-1} M_{a_2 b_3}^{-1} M_{a_3 b_1}^{-1} - M_{a_1 b_3}^{-1} M_{a_2 b_1}^{-1} M_{a_3 b_2}^{-1} + M_{a_1 b_3}^{-1} M_{a_2 b_2}^{-1} M_{a_3 b_1}^{-1} \right) \det M. \end{aligned} \quad (4.6)$$

Next, we know that our quark fields are smeared and covariantly displaced. Hence, the Grassmann integrals we really need to compute have the form

$$\int \mathcal{D}(\bar{\psi}, \psi) \sum_{cd} f_{ac} \psi_c \bar{\psi}_d g_{db} \exp \left(-\bar{\psi}^T M \psi \right) = \sum_{cd} f_{ac} M_{cd}^{-1} g_{db} \det M = Q_{ab}^{-1} \det M,$$

where f_{ac} and g_{db} are c -number coefficients, and we have defined

$$Q_{ab}^{-1} = \sum_{cd} f_{ac} M_{cd}^{-1} g_{db}.$$

The original path integral is defined in terms of ψ and $\bar{\psi}$, and the fermion action is defined in terms of a matrix K by $\bar{\psi} K \psi$. When we consider Hermiticity, we will find that the use of the field $\chi = \bar{\psi} \gamma_4$ will be more convenient. Changing the integration variable from $\bar{\psi}$ to χ is trivial since the Jacobian of the transformation is unity. The integration over the Grassmann fields leads to an Ω^{-1} factor for each coupling of one ψ to one χ field:

$$\int \mathcal{D}(\chi, \psi) \psi_a \chi_b \exp \left(-\chi^T \Omega \psi \right) = \Omega_{ab}^{-1} \det \Omega. \quad (4.7)$$

We refer to each such coupling as a *quark line*, which can be drawn as a directed line originating at the χ field and terminating at the ψ . Since our building blocks are gauge-covariantly displaced, smeared quark fields, our quark lines always have the form

$$\mathcal{Q} = \int \mathcal{D}(\chi, \psi) [D^{(j)} \tilde{\psi} \tilde{\chi} D^{(k)\dagger}] e^{(-\chi \Omega \psi)} = D^{(j)} S \Omega^{-1} S D^{(k)\dagger}, \quad (4.8)$$

Table 4.1: Three Types of Quark Lines

Type	Description	Diagram
forward-time quark line	A quark line which starts from χ field at early time t_0 and ends at ψ field at later time t	
backward-time quark line	A quark line which starts from χ field at later time t and ends at ψ field at earlier time t_0	
same-time quark line	A quark line which starts from χ field and ends at ψ field at the same time, either t or t_0	

where S is the smearing matrix. Quark lines can be drawn diagrammatically as a directed line originated from the creation operator χ and terminating at the annihilation operator ψ . There are three types of quark lines classified according to the starting and ending times as shown in Table 4.1.

If we write out the indices explicitly and use $S = V_s V_s^\dagger$, the quark line is

$$\mathcal{Q}_{ad} = D^{(j)} [V_s]_{al'} ([V_s^\dagger]_{l'b} \Omega_{bc}^{-1} [V_s]_{cm'}) [V_s^\dagger]_{m'd} D^{(k)\dagger}. \quad (4.9)$$

where a, b, c and d are the full indices with space, time, color and spin, l', m' are LapH eigenvector, time and spin indices. The term in parentheses $Q = V_s^\dagger \Omega^{-1} V_s$ is known as a *perambulator*, which describes the quark propagation in the subspace of states spanned by the retained eigenvectors of the Laplacian, that is, the LapH subspace. It is a matrix of size $N_P \times N_P$, where $N_P = N_v N_d N_t$, and N_v is the number of LapH eigenvectors used in the quark-smearing process, N_d is the number of quark spin indices, and N_t is the number of time slices on the lattice. A method that solves for these perambulators exactly to evaluate the quark lines is known as the *distillation* method[75], which has been used in Ref. [79] on a small $16^3 \times 128$ lattice. However, as shown in Fig. 4.1, the number of retained eigenvectors below the cutoff σ_s grows rapidly with the spatial lattice-volume. The number of retained eigenvectors N_v is proportional to N_s^3 on an N_s^3 lattice, and the computational resources required to invert the Dirac matrix are also proportional to N_s^3 . On a $(16^3|390)$ ensemble, one

finds that $N_v = 32$. For the $(24^3|390)$ ensemble, $N_v = 112$ is required, whereas for the $(32^3|240)$ ensemble, $N_v = 264$ is needed. The distillation method is not feasible for the $(32^3|240)$ ensemble.

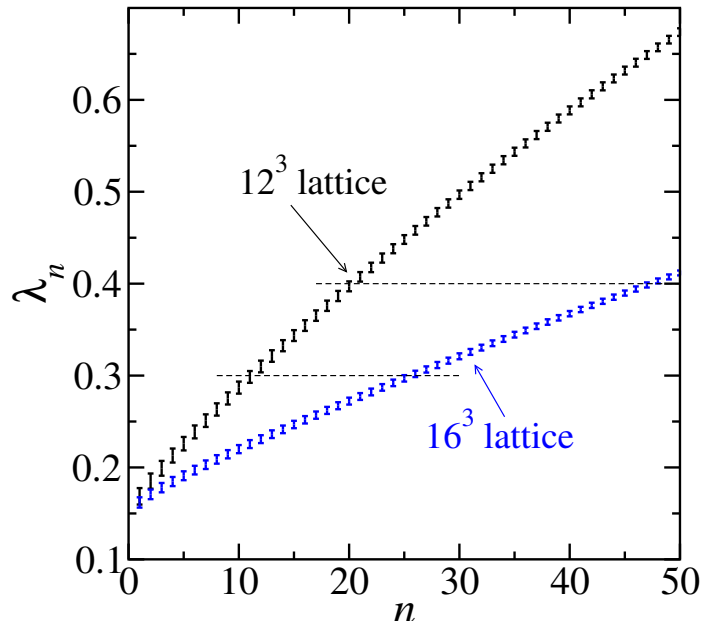


Figure 4.1: Volume dependence of the LapH eigenvalues on a set of configurations of the 12^3 and 16^3 lattice. In this figure, λ_n is the n -th lowest eigenvalue of the Laplacian operator $-\tilde{\Delta}$ on a given time slice. There are 9 eigenvalues between 0.3 and 0.4 for the 12^3 , compared to the 16^3 lattice which has 22 eigenvalues. This demonstrates the argument that $N_v \sim N_s^3$.

Since we are approximating our path integrals over the gauge field using the Monte Carlo method, we do not need to evaluate the quark lines exactly. In fact, it is quite wasteful to do so. We only need to determine the quark lines to within the precision of our Monte Carlo estimates. Thus, we can greatly improve the efficiency of our calculations by using stochastic estimates of the quark lines, as described in the next section.

4.2 Stochastic LapH Method with Noise Dilution

Inversion of the Dirac matrix within the accuracy of the gauge noise from Monte Carlo Method is accomplished with a method known as the stochastic LapH method [13]. In this method, we use Monte Carlo estimates of the inverse of the Dirac matrix. We

first introduce a set of random noises $\rho_{t\alpha m}$, where the subscript t indicates time, α is a Dirac spin component, and m is a LapH eigenvector number. Each noise component is chosen randomly from the elements of the group Z_4 . There are four elements in Z_4 , namely, $1, -1, i, -i$, so we choose one of these values for each component of the noise with equal probability. These noises satisfy

$$E(\rho) = 0, \quad E(\rho\rho^\dagger) = I_d, \quad (4.10)$$

where $E(\rho)$ indicates the statistical expectation value of ρ in probability theory, and I_d is the identity matrix. A stochastic estimate of a perambulator is then obtained from

$$\begin{aligned} Q &= V_s^\dagger \Omega^{-1} V_s \\ &= V_s^\dagger \Omega^{-1} V_s E(\rho\rho^\dagger) \\ &= V_s^\dagger E(\Omega^{-1} V_s \rho\rho^\dagger) \\ &= V_s^\dagger E(\phi\rho^\dagger) \\ &= E(\varphi\rho^\dagger), \end{aligned} \quad (4.11)$$

where $\Omega\phi = V_s\rho$ and $\varphi = V_s^\dagger\phi$. We then use a Monte Carlo estimate for the expectation value:

$$E(\varphi\rho^\dagger) \approx \frac{1}{N_r} \sum_r^{N_r} \varphi^r \rho^{r\dagger}. \quad (4.12)$$

In practice, the variance of such an estimate is too large to be useful [80], requiring a very large N_r for adequate precision. However, a significant noise reduction can be achieved through noise *dilution* in the LapH subspace. Define a dilution projection operator $P^{(b)}$ which satisfies

$$P^{(a)} P^{(b)} = \delta^{ab} P^{(b)}, \quad \sum_b P^{(b)} = I_d, \quad P^{(b)\dagger} = P^{(b)}. \quad (4.13)$$

Let $\rho^{[b]} = P^{(b)}\rho$ and

$$\Omega\phi^{[b]} = V_s\rho^{[b]}, \quad \varphi^{[b]} = V_s^\dagger\phi^{[b]} = V_s^\dagger\Omega^{-1}V_s\rho^{[b]}. \quad (4.14)$$

Then the Monte Carlo estimate of a perambulator is given by

$$Q = V_s^\dagger \Omega^{-1} V_s = E(\varphi \rho^\dagger) \approx \frac{1}{N_r} \sum_r \sum_b^{N_r} \varphi^{r[b]} \rho^{r[b]\dagger}. \quad (4.15)$$

The quark line can then be expressed as

$$\begin{aligned} \mathcal{Q} &= D^{(j)} V_s (V_s^\dagger \Omega^{-1} V_s) V_s^\dagger D^{(k)\dagger} \\ &\approx \frac{1}{N_r} \sum_r \sum_b^{N_r} (D^{(j)} V_s \varphi^{r[b]}) (D^{(k)} V_s \rho^{r[b]})^\dagger. \end{aligned} \quad (4.16)$$

Define *quark sink* and *quark source* vectors by

$$\varrho^{[b]}(\rho) = D^{(j)} V_s P^{(b)} \rho, \quad \text{quark source,} \quad (4.17)$$

$$\varphi^{[b]}(\rho) = D^{(j)} S \Omega^{-1} V_s P^{(b)} \rho, \quad \text{quark sink,} \quad (4.18)$$

then we have

$$\mathcal{Q}_{uv}^{(AB)} \approx \frac{1}{N_r} \delta_{AB} \sum_r \sum_b^{N_r} \varphi_u^{[b]}(\rho^r) \varrho_v^{[b]}(\rho^r)^*, \quad (4.19)$$

where u, v are compound indices combining space, time, color, spin and quark displacement type, and A, B are flavor indices. The quark sink φ has flavor A , and quark source ϱ has flavor B . The δ_{AB} function ensures that only contractions of the same flavor are performed.

When computing correlators for meson operators, it is sometimes useful to estimate a backward quark line using γ_5 -Hermiticity. Recall that $K^\dagger = \gamma_5 K \gamma_5$, then the quark line can be expressed as

$$\mathcal{Q}_{uv}^{(AB)} \approx \frac{1}{N_r} \delta_{AB} \sum_r \sum_b^{N_r} \bar{\varrho}_u^{[b]}(\rho^r) \bar{\varphi}_v^{[b]}(\rho^r)^*, \quad (4.20)$$

defining

$$\bar{\varrho}(\rho) = -\gamma_5 \gamma_4 \varrho(\rho), \quad \bar{\varphi}(\rho) = \gamma_5 \gamma_4 \varphi(\rho). \quad (4.21)$$

This effectively switches the quark sources and quark sinks such that we can group the quark sinks for the meson at sink time t_F and quark sources at source time t_0 , which can simplify the computation and storage.

Eq. (4.19) is used inside Eq. (4.1). Hence, the sums over noises are Monte Carlo estimates within the Monte Carlo estimate defined in terms of an average over gauge configurations. These various summations can be viewed as one grand Monte Carlo estimate involving averages over both gauge configurations and noise vectors. This allows us to set $N_r = 1$ and achieve multiple noises via the multiple gauge configurations. We must make sure to use a different random noise vector for each gauge configuration. On the other hand, for a correlator involving more than one quark line, a different noise vector must be used for each different quark line.

The dilution projection operator we use can be decomposed into the product of three dilution operators in time(T), spin(S) and LapH eigenvector(L) subspaces with the projection indices labeled by b_T , b_S and b_L respectively. In other words, the projection operator can be written as

$$P_{t\alpha n|t'\alpha'n'}^{(b)} = P_{tt'}^{(b_T)} P_{\alpha\alpha'}^{(b_S)} P_{nn'}^{(b_L)}, \quad (4.22)$$

where each operator is applied to different subspaces separately. Let N be the dimension of each subspace, then $P_{tt'}^{(b_T)}$ is a $N \times N$ matrix that acts on time indices t, t' with $N = N_t$, $P_{\alpha\alpha'}^{(b_S)}$ is a $N \times N$ matrix that acts on spin indices α, α' with $N = 4$ and $P_{nn'}^{(b_L)}$ is a $N \times N$ matrix that acts on LapH eigenvector indices n, n' with $N = N_v$ being the number of LapH smearing eigenvectors. For a dilution projection operator $P_{ij}^{(b)}$ applied to a particular subspace, we have defined four dilution schemes to be studied:

$$\begin{aligned} P_{ij}^{(b)} &= \delta_{ij}, & b &= 0, & \text{(no dilution)} \\ P_{ij}^{(b)} &= \delta_{ij} \delta_{bi}, & b &= 0, \dots, N-1, & \text{(full dilution)} \\ P_{ij}^{(b)} &= \delta_{ij} \delta_{b, Ji/N} & b &= 0, \dots, J-1, & \text{(block-} J \text{)} \\ P_{ij}^{(b)} &= \delta_{ij} \delta_{a, i \bmod J} & b &= 0, \dots, J-1, & \text{(interlace-} J \text{)} \end{aligned}$$

where J is tunable and for simplicity we always choose N/J to be an integer. Note that δ_{ij} appearing in each projection operator ensures that the dilution operators are diagonal. The second δ function produces a matrix with some of the diagonal elements set to zero for some b dilution indices. This effectively “dilutes” the original source random vector ρ such that for a given dilution combination $b = (b_T, b_S, b_L)$, only some small parts of the random vector ρ are nonzero. To simplify notation, we can define a triplet (T, S, L) to represent the dilution scheme on (time, spin, LapH) subspaces. Furthermore, for simplicity, we use 1 for no dilution, F for full dilution, BJ

for the block-J scheme and IJ for the interlace-J scheme. A dilution scheme labeled as (TF, SF, LI8) represents full time dilution, full spin dilution and interlace-8 LapH dilution. The dilution scheme used is crucial for reducing the statistical uncertainties in our Monte Carlo estimates. Testing different dilution schemes is described later in Chapter 5.

4.3 Correlator Construction of Hadrons

The application of the stochastic LapH method to compute the hadronic correlators is described in this section.

4.3.1 Meson to Meson Correlators

The simplest correlators to compute involve a single meson at the source and a single meson at the sink. Our meson operators have the form

$$M_l(t) = f^{AB} c_{\alpha\beta}^{(l)} \Phi_{\alpha\beta}^{AB}(t), \quad (4.23)$$

where l is a short-hand index representing momentum \mathbf{p} , the irreducible representation(irrep) Λ , the row λ of the irrep, total isospin I , isospin projection I_3 and strangeness S . The corresponding source operators have the form

$$\overline{M}_l(t) = f^{AB} c_{\alpha\beta}^{(l)*} \overline{\Phi}_{\alpha\beta}^{AB}(t). \quad (4.24)$$

Thus, the meson correlation functions are given by

$$C_{\bar{l}l}(t_F - t_0) = \langle M_l(t_F) \overline{M}_{\bar{l}}(t_0) \rangle = f^{AB} f^{\overline{AB}} c_{\alpha\beta}^{(l)} c_{\bar{\alpha}\bar{\beta}}^{(\bar{l})*} \langle \Phi_{\alpha\beta}^{AB}(t_F) \overline{\Phi}_{\bar{\alpha}\bar{\beta}}^{\overline{AB}}(t_0) \rangle, \quad (4.25)$$

where $\langle \dots \rangle$ indicates the vacuum expectation value, evaluated as a ratio of path integrals over the quark and gluon fields. With the definition of meson elementals from Eq. (3.22) and Eq. (3.23), we can expand the meson correlator in terms of the covariantly-displaced smeared quark fields

$$\begin{aligned} C_{\bar{l}l}(t_F - t_0) &= f^{AB} f^{\overline{AB}} c_{\alpha\beta}^{(l)} c_{\bar{\alpha}\bar{\beta}}^{(\bar{l})*} \sum_{\mathbf{x}\overline{\mathbf{x}}} e^{-i\mathbf{p}\cdot(\mathbf{x} + \frac{1}{2}(\mathbf{d}_\alpha + \mathbf{d}_\beta))} e^{i\mathbf{p}\cdot(\overline{\mathbf{x}} + \frac{1}{2}(\mathbf{d}_{\bar{\alpha}} + \mathbf{d}_{\bar{\beta}}))} \\ &\quad \times \langle \overline{q}_{a\alpha}^A(\mathbf{x}, t_F) q_{a\beta}^B(\mathbf{x}, t_F) \overline{q}_{\bar{a}\bar{\beta}}^{\overline{B}}(\overline{\mathbf{x}}, t_0) q_{\bar{a}\bar{\alpha}}^{\overline{A}}(\overline{\mathbf{x}}, t_0) \rangle. \end{aligned}$$

Using Wick's theorem, the integration over the quark fields yields

$$C_{\bar{l}l}(t_F - t_0) = f^{AB} f^{\bar{A}\bar{B}} c_{\alpha\beta}^{(l)} c_{\bar{\alpha}\bar{\beta}}^{(\bar{l})*} \sum_{\mathbf{x}\bar{\mathbf{x}}} e^{-i\mathbf{p}\cdot(\mathbf{x}+\frac{1}{2}(\mathbf{d}_\alpha+\mathbf{d}_\beta))} e^{i\mathbf{p}\cdot(\bar{\mathbf{x}}+\frac{1}{2}(\mathbf{d}_{\bar{\alpha}}+\mathbf{d}_{\bar{\beta}}))} \\ \times \left\langle -\mathcal{Q}_{\bar{a}\alpha\bar{\mathbf{x}}t_0;a\alpha\mathbf{x}t_F}^{(\bar{A}A)} \mathcal{Q}_{a\beta\mathbf{x}t_F;\bar{a}\bar{\beta}\bar{\mathbf{x}}t_0}^{(B\bar{B})} + \mathcal{Q}_{a\beta\mathbf{x}t_F;a\alpha\mathbf{x}t_F}^{(BA)} \mathcal{Q}_{\bar{a}\alpha\bar{\mathbf{x}}t_0;\bar{a}\bar{\beta}\bar{\mathbf{x}}t_0}^{(\bar{A}\bar{B})} \right\rangle_U. \quad (4.26)$$

The subscript U indicates that only the integration over the gauge field is left in the path integral. Since we use the stochastic LapH method with dilution to evaluate the quark lines, each quark line in Eq. (4.26) can be expressed as

$$\mathcal{Q}_{\bar{a}\alpha\bar{\mathbf{x}}t_0;a\alpha\mathbf{x}t_F}^{(\bar{A}A)} \approx \delta_{\bar{A}A} \sum_{b_1} \bar{\varrho}_{\bar{a}\alpha\bar{\mathbf{x}}t_0}^{[b_1]}(\rho_1) \bar{\varphi}_{a\alpha\mathbf{x}t_F}^{[b_1]}(\rho_1)^*, \quad (4.27)$$

$$\mathcal{Q}_{a\beta\mathbf{x}t_F;\bar{a}\bar{\beta}\bar{\mathbf{x}}t_0}^{(B\bar{B})} \approx \delta_{B\bar{B}} \sum_{b_2} \varphi_{a\beta\mathbf{x}t_0}^{[b_2]}(\rho_2) \varrho_{\bar{a}\bar{\beta}\bar{\mathbf{x}}t_F}^{[b_2]}(\rho_2)^*, \quad (4.28)$$

$$\mathcal{Q}_{a\beta\mathbf{x}t_F;a\alpha\mathbf{x}t_F}^{(BA)} \approx \delta_{BA} \sum_{b_1} \varphi_{a\beta\mathbf{x}t_F}^{[b_1]}(\rho_1) \varrho_{a\alpha\mathbf{x}t_F}^{[b_1]}(\rho_1)^*, \quad (4.29)$$

$$\mathcal{Q}_{\bar{a}\alpha\bar{\mathbf{x}}t_0;\bar{a}\bar{\beta}\bar{\mathbf{x}}t_0}^{(\bar{A}\bar{B})} \approx \delta_{\bar{A}\bar{B}} \sum_{b_2} \varphi_{\bar{a}\alpha\bar{\mathbf{x}}t_0}^{[b_2]}(\rho_2) \varrho_{\bar{a}\bar{\beta}\bar{\mathbf{x}}t_0}^{[b_2]}(\rho_2)^*, \quad (4.30)$$

where Eq. (4.27) uses Eq. (4.20) and the other three quark lines use Eq. (4.19), omitting the summation over different noises since this can be incorporated into the summation over the gauge configurations. Using γ_5 -Hermiticity for the backward quark lines enables the separation of the meson correlator into a function involving only the sink time t_F and another function involving only the source time t_0 . Define the meson function

$$\mathcal{M}_l^{[b_1 b_2]}(\varrho_1, \varphi_2; t) = c_{\alpha\beta}^{(l)} \sum_{\mathbf{x}} e^{-i\mathbf{p}\cdot(\mathbf{x}+\frac{1}{2}(\mathbf{d}_\alpha+\mathbf{d}_\beta))} \varrho_{a\alpha\mathbf{x}t}^{[b_1]}(\rho_1)^* \varphi_{a\beta\mathbf{x}t}^{[b_2]}(\rho_2), \quad (4.31)$$

where b_1, b_2 are noise dilution indices, and the short-hand notation $\varphi_i \equiv \varphi(\rho_i)$ and $\varrho_i \equiv \varrho(\rho_i)$ are used. The meson correlator is given by:

$$C_{\bar{l}l}(t_F - t_0) = f^{AB} f^{\bar{A}\bar{B}} \left\langle -\delta_{\bar{A}\bar{B}} \mathcal{M}_l^{[b_1 b_2]}(\bar{\varphi}_1, \varphi_2; t_F) \mathcal{M}_{\bar{l}}^{[b_1 b_2]}(\bar{\varrho}_1, \varrho_2; t_0)^* \right. \\ \left. + \delta_{\bar{A}\bar{B}} \mathcal{M}_l^{[b_1 b_1]}(\varrho_1, \varphi_1; t_F) \mathcal{M}_{\bar{l}}^{[b_2 b_2]}(\varphi_2, \varrho_2; t_0)^* \right\rangle_{U, \rho}, \quad (4.32)$$

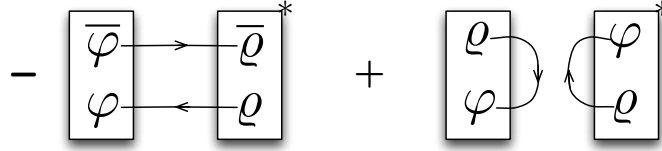


Figure 4.2: Quark line diagrams for a meson to meson correlator. The lines indicate contractions over dilution indices. The second term is needed only for isoscalar mesons.

with definition $\delta_{AB}^{CD} \equiv \delta_{AC}\delta_{BD}$. The subscripts U and ρ indicate that quantity inside the angle brackets is computed using Monte Carlo integration over different gauge field configurations with a different noise vector ρ for each configuration. The factorization of the meson correlators into meson functions at the sink time and the source time helps to dramatically simplify the calculations, especially when making a large matrix of such correlators. Usually one has to use Eq. (4.26) and perform the spatial sums over \mathbf{x} , $\bar{\mathbf{x}}$ many times for every pair of meson operators of types l , \bar{l} . These spatial sums are very costly and not reusable. Using the stochastic LapH method with dilution, the summations over color, spin and space for different types of operators at t_0 and t_F can be computed and stored separately. To compute a correlator matrix with operator type l , \bar{l} , one only needs to reuse these meson functions to perform the summations over the leftover dilution indices.

Equation (4.32) can be diagrammatically represented as in Fig. 4.2. In each diagram, the quark sinks are represented by φ and the quark sources are represented by ϱ . For the γ_5 -Hermiticity mode, the quark sinks are represented by $\bar{\varphi}$ and quark sources by $\bar{\varrho}$. Each meson function is grouped into a box at either the source time t_0 or the sink time t_F , where our convention assumes the right boxes are at time t_0 and the left boxes are at later time t_F . Connections between these quark sinks/sources indicate summations over dilution indices. The boxes take into account the superposition coefficients that define each meson, and the complex conjugate of the source function is needed in the correlator expression. Flavor coefficients f^{AB} must also be carefully handled.

4.3.2 Baryon to Baryon Correlators

Baryon sink operators can be expressed as

$$B_l(t) = f^{ABC} c_{\alpha\beta\gamma}^{(l)} \Phi_{\alpha\beta\gamma}^{ABC}(t), \quad (4.33)$$

where the coefficients $c_{\alpha\beta\gamma}^{(l)}$ and the flavor structure coefficients f^{ABC} were discussed earlier in Sec. 3.4. The corresponding source operators are

$$\overline{B}_l(t) = f^{ABC} c_{\alpha\beta\gamma}^{(l)*} \overline{\Phi}_{\alpha\beta\gamma}^{ABC}(t). \quad (4.34)$$

Therefore, baryon correlation functions are given by

$$C_{\bar{l}l}(t_F - t_0) = \langle B_l(t_F) \overline{B}_{\bar{l}}(t_0) \rangle = f^{ABC} f^{\overline{ABC}} c_{\alpha\beta\gamma}^{(l)} c_{\bar{\alpha}\bar{\beta}\bar{\gamma}}^{(\bar{l})*} \langle \Phi_{\alpha\beta\gamma}^{ABC}(t_F) \overline{\Phi}_{\bar{\alpha}\bar{\beta}\bar{\gamma}}^{\overline{ABC}}(t_0) \rangle. \quad (4.35)$$

Again, we can replace the baryon elementals defined in Eq. (3.24) and Eq. (3.25) with their expressions in terms of covariantly-displaced smeared quark fields

$$\begin{aligned} C_{\bar{l}l}(t_F - t_0) &= f^{ABC} f^{\overline{ABC}} c_{\alpha\beta\gamma}^{(l)} c_{\bar{\alpha}\bar{\beta}\bar{\gamma}}^{(\bar{l})*} \sum_{\mathbf{x}\overline{\mathbf{x}}} \varepsilon_{abc} \varepsilon_{\bar{a}\bar{b}\bar{c}} e^{-i\mathbf{p}\cdot(\mathbf{x}-\overline{\mathbf{x}})} \\ &\quad \times \langle q_{a\alpha}^A(\mathbf{x}, t_F) q_{b\beta}^B(\mathbf{x}, t_F) q_{c\gamma}^C(\mathbf{x}, t_F) \overline{q}_{\bar{c}\bar{\gamma}}^{\overline{C}}(\overline{\mathbf{x}}, t_0) \overline{q}_{\bar{b}\bar{\beta}}^{\overline{B}}(\overline{\mathbf{x}}, t_0) \overline{q}_{\bar{a}\bar{\alpha}}^{\overline{A}}(\overline{\mathbf{x}}, t_0) \rangle. \end{aligned}$$

The next step is to integrate out the quark fields via Wick contractions and express the baryon correlator in terms of quark lines, defined in Eq. (4.8), as

$$\begin{aligned} C_{\bar{l}l}(t_F - t_0) &= f^{ABC} f^{\overline{ABC}} c_{\alpha\beta\gamma}^{(l)} c_{\bar{\alpha}\bar{\beta}\bar{\gamma}}^{(\bar{l})*} \sum_{\mathbf{x}\overline{\mathbf{x}}} \varepsilon_{abc} \varepsilon_{\bar{a}\bar{b}\bar{c}} e^{-i\mathbf{p}\cdot(\mathbf{x}-\overline{\mathbf{x}})} \\ &\quad \times \left\langle \mathcal{Q}_{a\alpha\mathbf{x}t_F;\overline{a}\alpha\overline{\mathbf{x}}t_0}^{(A\overline{A})} \mathcal{Q}_{b\beta\mathbf{x}t_F;\overline{b}\beta\overline{\mathbf{x}}t_0}^{(B\overline{B})} \mathcal{Q}_{c\gamma\mathbf{x}t_F;\overline{c}\gamma\overline{\mathbf{x}}t_0}^{(C\overline{C})} - \mathcal{Q}_{a\alpha\mathbf{x}t_F;\overline{a}\alpha\overline{\mathbf{x}}t_0}^{(A\overline{A})} \mathcal{Q}_{b\beta\mathbf{x}t_F;\overline{c}\gamma\overline{\mathbf{x}}t_0}^{(B\overline{C})} \mathcal{Q}_{c\gamma\mathbf{x}t_F;\overline{b}\beta\overline{\mathbf{x}}t_0}^{(C\overline{B})} \right. \\ &\quad - \mathcal{Q}_{a\alpha\mathbf{x}t_F;\overline{b}\beta\overline{\mathbf{x}}t_0}^{(A\overline{B})} \mathcal{Q}_{b\beta\mathbf{x}t_F;\overline{a}\alpha\overline{\mathbf{x}}t_0}^{(B\overline{A})} \mathcal{Q}_{c\gamma\mathbf{x}t_F;\overline{c}\gamma\overline{\mathbf{x}}t_0}^{(C\overline{C})} - \mathcal{Q}_{a\alpha\mathbf{x}t_F;\overline{c}\gamma\overline{\mathbf{x}}t_0}^{(A\overline{C})} \mathcal{Q}_{b\beta\mathbf{x}t_F;\overline{b}\beta\overline{\mathbf{x}}t_0}^{(B\overline{B})} \mathcal{Q}_{c\gamma\mathbf{x}t_F;\overline{a}\alpha\overline{\mathbf{x}}t_0}^{(C\overline{A})} \\ &\quad \left. + \mathcal{Q}_{a\alpha\mathbf{x}t_F;\overline{c}\gamma\overline{\mathbf{x}}t_0}^{(A\overline{C})} \mathcal{Q}_{b\beta\mathbf{x}t_F;\overline{a}\alpha\overline{\mathbf{x}}t_0}^{(B\overline{A})} \mathcal{Q}_{c\gamma\mathbf{x}t_F;\overline{b}\beta\overline{\mathbf{x}}t_0}^{(C\overline{B})} + \mathcal{Q}_{a\alpha\mathbf{x}t_F;\overline{b}\beta\overline{\mathbf{x}}t_0}^{(A\overline{B})} \mathcal{Q}_{b\beta\mathbf{x}t_F;\overline{c}\gamma\overline{\mathbf{x}}t_0}^{(B\overline{C})} \mathcal{Q}_{c\gamma\mathbf{x}t_F;\overline{a}\alpha\overline{\mathbf{x}}t_0}^{(C\overline{A})} \right\rangle_U. \end{aligned} \quad (4.36)$$

We then approximate each quark line using the stochastic LapH method with noise dilution, and group the quark sinks φ from Eq. (4.18) and quark sources ϱ from Eq. (4.17) into source and sink baryon functions. Define a baryon function by

$$\mathcal{B}_l^{[b_1 b_2 b_3]}(\varphi_1, \varphi_2, \varphi_3; t) = c_{\alpha\beta\gamma}^{(l)} \sum_{\mathbf{x}} e^{-i\mathbf{p}\cdot\mathbf{x}} \varepsilon_{abc} \varphi_{a\alpha\mathbf{x}t}^{[b_1]}(\rho_1) \varphi_{b\beta\mathbf{x}t}^{[b_2]}(\rho_2) \varphi_{c\gamma\mathbf{x}t}^{[b_3]}(\rho_3), \quad (4.37)$$

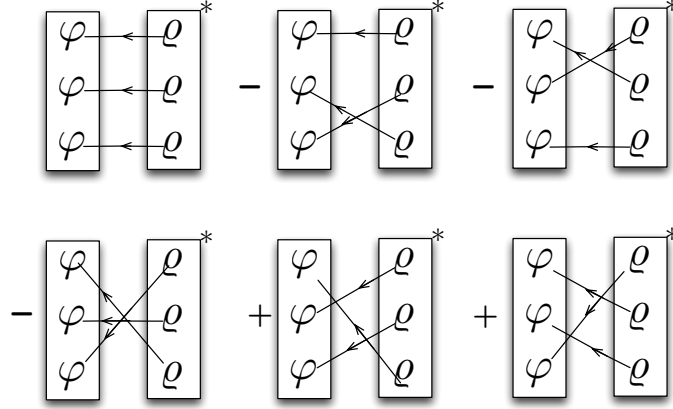


Figure 4.3: Diagrammatic representation of the quark lines involved in baryon to baryon correlators.

where b_1, b_2, b_3 are noise dilution indices and the short-hand notation $\varphi_i \equiv \varphi(\rho_i)$ and $\varrho_i \equiv \varrho(\rho_i)$ are used. The baryon correlator can then be expressed as:

$$\begin{aligned}
C_{\bar{u}u}(t_F - t_0) &= f^{ABC} f^{\overline{ABC}} \left\langle \mathcal{B}_l^{[b_1 b_2 b_3]}(\varphi_1, \varphi_2, \varphi_3; t_F) \right. \\
&\quad \times \left(\delta_{ABC}^{\overline{ABC}} \mathcal{B}_l^{[b_1 b_2 b_3]}(\varrho_1, \varrho_2, \varrho_3; t_0) - \delta_{ABC}^{\overline{ACB}} \mathcal{B}_l^{[b_1 b_3 b_2]}(\varrho_1, \varrho_3, \varrho_2; t_0) \right. \\
&\quad - \delta_{ABC}^{\overline{BAC}} \mathcal{B}_l^{[b_2 b_1 b_3]}(\varrho_2, \varrho_1, \varrho_3; t_0) - \delta_{ABC}^{\overline{CBA}} \mathcal{B}_l^{[b_3 b_2 b_1]}(\varrho_3, \varrho_2, \varrho_1; t_0) \\
&\quad \left. \left. + \delta_{ABC}^{\overline{CAB}} \mathcal{B}_l^{[b_2 b_3 b_1]}(\varrho_2, \varrho_3, \varrho_1; t_0) + \delta_{ABC}^{\overline{BCA}} \mathcal{B}_l^{[b_3 b_1 b_2]}(\varrho_3, \varrho_1, \varrho_2; t_0) \right) \right\rangle_{U, \rho}^*
\end{aligned} \tag{4.38}$$

where we define $\delta_{ABC}^{DEF} \equiv \delta_{AD} \delta_{BE} \delta_{CF}$, and a Monte Carlo average over the gauge field U using a different noise ρ for each configuration is indicated. A, B, C are quark flavors.

Similar to the meson correlators, we can represent Eq. (4.38) diagrammatically, as shown in Fig. 4.3. A box containing three quark sinks/sources is used to represent a baryon sink/source function, with the same convention assuming the right boxes are at source time t_0 and the left boxes are at sink time t_F . There are six terms in Eq. (4.38) corresponding to the permutations of the three quark sources. Grassmann fields anticommute, so the different permutations lead to a plus or minus sign in front of each diagram. Again, the baryon coefficients in terms of the three-quark elementals and the flavor coefficients are absorbed into the baryon function definitions, which are represented by the boxes.

4.3.3 Two-Meson to Meson correlators

Our two meson operators are combinations of single-hadron operators of the form

$$\overline{H}_l(t) = g_{mn}^{(l)*} \overline{M}_m \overline{M}_n = f^{ABCD} g_{mn}^{(l)*} c_{\alpha\beta}^{(m)*} c_{\gamma\delta}^{(n)*} \overline{\Phi}_{\alpha\beta}^{AB}(t) \overline{\Phi}_{\gamma\delta}^{CD}(t), \quad (4.39)$$

where the flavor coefficients f^{ABCD} and the meson-meson superposition coefficients $g_{mn}^{(l)*}$ are determined using group theoretical projections. The coefficients $c_{\alpha\beta}^{(m)*}$ express each single meson in terms of the quark-antiquark elemental operators, as previously described. To evaluate a two-meson to a one-meson correlator, we must first express the correlator in terms of the displaced and smeared quark and antiquark fields

$$\begin{aligned} C_{\bar{l}l}(t_F - t_0) &= \left\langle M_l(t_F) \overline{H}_{\bar{l}}(t_0) \right\rangle = f^{AB} f^{\bar{A}'\bar{B}'\bar{A}''\bar{B}''} c_{\alpha\beta}^{(l)} g_{\bar{l}'\bar{l}''}^{(\bar{l})*} c_{\bar{\alpha}'\bar{\beta}'}^{(\bar{l}')*} c_{\bar{\alpha}''\bar{\beta}''}^{(\bar{l}'')*} \\ &\times \sum_{\mathbf{x}\bar{\mathbf{x}}'\bar{\mathbf{x}}''} e^{-i\mathbf{p}\cdot(\mathbf{x}+\frac{1}{2}(\mathbf{d}_\alpha+\mathbf{d}_\beta))} e^{i\mathbf{p}'\cdot(\bar{\mathbf{x}}'+\frac{1}{2}(\mathbf{d}_{\alpha'}+\mathbf{d}_{\beta'}))} e^{i\mathbf{p}''\cdot(\bar{\mathbf{x}}''+\frac{1}{2}(\mathbf{d}_{\alpha''}+\mathbf{d}_{\beta''}))} \\ &\times \left\langle \bar{q}_{a\alpha}^A(\mathbf{x}, t_F) q_{a\beta}^B(\mathbf{x}, t_F) \bar{q}_{\bar{a}'\bar{\beta}'}^{\bar{B}'}(\bar{\mathbf{x}}', t_0) q_{\bar{a}'\bar{\alpha}'}^{\bar{A}'}(\bar{\mathbf{x}}', t_0) \bar{q}_{\bar{a}''\bar{\beta}''}^{\bar{B}''}(\bar{\mathbf{x}}'', t_0) q_{\bar{a}''\bar{\alpha}''}^{\bar{A}''}(\bar{\mathbf{x}}'', t_0) \right\rangle. \end{aligned}$$

The single-meson sink operator must have a momentum equal to the sum of the two separate source mesons: $\mathbf{p} = \mathbf{p}' + \mathbf{p}''$. Integrate over the quark fields using Wick's theorem to obtain

$$\begin{aligned} C_{\bar{l}l}(t_F - t_0) &= f^{AB} f^{\bar{A}'\bar{B}'\bar{A}''\bar{B}''} c_{\alpha\beta}^{(l)} g_{\bar{l}'\bar{l}''}^{(\bar{l})*} c_{\bar{\alpha}'\bar{\beta}'}^{(\bar{l}')*} c_{\bar{\alpha}''\bar{\beta}''}^{(\bar{l}'')*} \\ &\times \sum_{\mathbf{x}\bar{\mathbf{x}}'\bar{\mathbf{x}}''} e^{-i\mathbf{p}\cdot(\mathbf{x}+\frac{1}{2}(\mathbf{d}_\alpha+\mathbf{d}_\beta))} e^{i\mathbf{p}'\cdot(\bar{\mathbf{x}}'+\frac{1}{2}(\mathbf{d}_{\alpha'}+\mathbf{d}_{\beta'}))} e^{i\mathbf{p}''\cdot(\bar{\mathbf{x}}''+\frac{1}{2}(\mathbf{d}_{\alpha''}+\mathbf{d}_{\beta''}))} \\ &\times \left\langle -\mathcal{Q}_{a\beta\mathbf{x}t_F;a\alpha\mathbf{x}t_F}^{(BA)} \mathcal{Q}_{\bar{a}'\bar{\alpha}'\bar{\mathbf{x}}'t_0;\bar{a}'\bar{\beta}'\bar{\mathbf{x}}'t_0}^{(\bar{A}'\bar{B}')} \mathcal{Q}_{\bar{a}''\bar{\alpha}''\bar{\mathbf{x}}''t_0;\bar{a}''\bar{\beta}''\bar{\mathbf{x}}''t_0}^{(\bar{A}''\bar{B}'')} \right. \\ &\quad - \mathcal{Q}_{\bar{a}'\bar{\alpha}'\bar{\mathbf{x}}'t_0;\bar{a}''\bar{\beta}''\bar{\mathbf{x}}''t_0}^{(\bar{A}'\bar{B}'')} \mathcal{Q}_{\bar{a}''\bar{\alpha}''\bar{\mathbf{x}}''t_0;a\alpha\mathbf{x}t_F}^{(\bar{A}''A)} \mathcal{Q}_{a\beta\mathbf{x}t_F;\bar{a}'\bar{\beta}'\bar{\mathbf{x}}'t_0}^{(B\bar{B}')} \\ &\quad - \mathcal{Q}_{\bar{a}''\bar{\alpha}''\bar{\mathbf{x}}''t_0;\bar{a}'\bar{\beta}'\bar{\mathbf{x}}'t_0}^{(\bar{A}'\bar{B}')} \mathcal{Q}_{a\beta\mathbf{x}t_F;\bar{a}''\bar{\beta}''\bar{\mathbf{x}}''t_0}^{(B\bar{B}'')} \mathcal{Q}_{\bar{a}'\bar{\alpha}'\bar{\mathbf{x}}'t_0;a\alpha\mathbf{x}t_F}^{(\bar{A}'A)} \\ &\quad + \mathcal{Q}_{\bar{a}''\bar{\alpha}''\bar{\mathbf{x}}''t_0;\bar{a}''\bar{\beta}''\bar{\mathbf{x}}''t_0}^{(\bar{A}''\bar{B}'')} \mathcal{Q}_{a\beta\mathbf{x}t_F;\bar{a}'\bar{\beta}'\bar{\mathbf{x}}'t_0}^{(B\bar{B}')} \mathcal{Q}_{\bar{a}'\bar{\alpha}'\bar{\mathbf{x}}'t_0;a\alpha\mathbf{x}t_F}^{(\bar{A}'A)} \\ &\quad + \mathcal{Q}_{\bar{a}''\bar{\alpha}''\bar{\mathbf{x}}''t_0;\bar{a}'\bar{\beta}'\bar{\mathbf{x}}'t_0}^{(\bar{A}''\bar{B}')} \mathcal{Q}_{\bar{a}'\bar{\alpha}'\bar{\mathbf{x}}'t_0;\bar{a}''\bar{\beta}''\bar{\mathbf{x}}''t_0}^{(\bar{A}'\bar{B}'')} \mathcal{Q}_{a\beta\mathbf{x}t_F;a\alpha\mathbf{x}t_F}^{(BA)} \\ &\quad \left. + \mathcal{Q}_{\bar{a}''\bar{\alpha}''\bar{\mathbf{x}}''t_0;a\alpha\mathbf{x}t_F}^{(\bar{A}''A)} \mathcal{Q}_{a\beta\mathbf{x}t_F;\bar{a}''\bar{\beta}''\bar{\mathbf{x}}''t_0}^{(B\bar{B}'')} \mathcal{Q}_{\bar{a}'\bar{\alpha}'\bar{\mathbf{x}}'t_0;\bar{a}'\bar{\beta}'\bar{\mathbf{x}}'t_0}^{(\bar{A}'\bar{B}')} \right\rangle. \quad (4.40) \end{aligned}$$

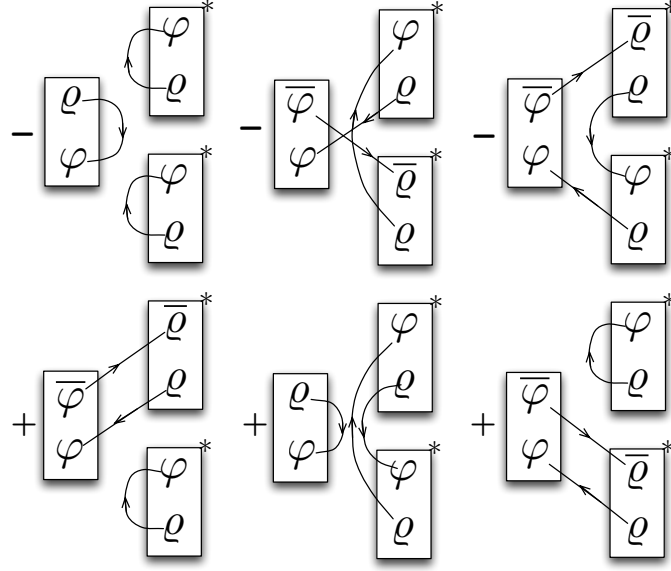


Figure 4.4: The quark line diagrams for a correlator whose source is a two-meson operator and whose sink is a single meson operator. The quark lines indicate summations over dilation indices, and the flavor must be the same at both ends or a zero value results. Diagrams with a quark line beginning and ending in the same meson will be zero unless that meson is an isoscalar.

Approximate each quark line using the stochastic LapH method, then collect together appropriate factors into the meson functions defined in Sec. 4.3.1 to get

$$\begin{aligned}
C_{\bar{l}l}(t_F - t_0) = & f^{AB} f^{\bar{A}\bar{B}'\bar{A}''\bar{B}''} g_{\bar{l}'\bar{l}''}^{(\bar{l})*} \\
& \times \left\langle -\delta_{BA}\delta_{\bar{A}'\bar{B}'}\delta_{\bar{A}''\bar{B}''}\mathcal{M}_l^{[b_0b_0]}(\varphi_0, \varphi_0; t_F)\mathcal{M}_{\bar{l}'}^{[b_1b_1]}(\varphi_1, \varphi_1; t_0)^*\mathcal{M}_{\bar{l}''}^{[b_2b_2]}(\varphi_2, \varphi_2; t_0)^* \right. \\
& -\delta_{\bar{A}'\bar{B}''}\delta_{\bar{A}''\bar{A}}\delta_{\bar{B}\bar{B}'}\mathcal{M}_{\bar{l}'}^{[b_0b_2]}(\varphi_0, \varphi_2; t_0)^*\mathcal{M}_{\bar{l}''}^{[b_1b_0]}(\bar{\varphi}_1, \varphi_0; t_0)^*\mathcal{M}_{\bar{l}}^{[b_1b_2]}(\bar{\varphi}_1, \varphi_2; t_F) \\
& -\delta_{\bar{A}''\bar{B}'}\delta_{\bar{B}\bar{B}''}\delta_{\bar{A}'\bar{A}}\mathcal{M}_{\bar{l}''}^{[b_0b_1]}(\varphi_0, \varphi_1; t_0)^*\mathcal{M}_{\bar{l}'}^{[b_2b_0]}(\bar{\varphi}_2, \varphi_0; t_0)^*\mathcal{M}_{\bar{l}}^{[b_2b_1]}(\bar{\varphi}_2, \varphi_1; t_F) \\
& +\delta_{\bar{A}''\bar{B}''}\delta_{\bar{B}\bar{B}'}\delta_{\bar{A}'\bar{A}}\mathcal{M}_{\bar{l}''}^{[b_0b_0]}(\varphi_0, \varphi_0; t_0)^*\mathcal{M}_{\bar{l}}^{[b_2b_1]}(\bar{\varphi}_2, \varphi_1; t_F)\mathcal{M}_{\bar{l}'}^{[b_2b_1]}(\bar{\varphi}_2, \varphi_1; t_0)^* \\
& +\delta_{\bar{A}''\bar{B}'}\delta_{\bar{A}'\bar{B}''}\delta_{\bar{B}\bar{A}}\mathcal{M}_{\bar{l}''}^{[b_0b_1]}(\varphi_0, \varphi_1; t_0)^*\mathcal{M}_{\bar{l}'}^{[b_1b_0]}(\varphi_1, \varphi_0; t_0)^*\mathcal{M}_{\bar{l}}^{[b_2b_2]}(\varphi_2, \varphi_2; t_F) \\
& \left. +\delta_{\bar{A}''\bar{A}}\delta_{\bar{B}\bar{B}''}\delta_{\bar{A}'\bar{B}'}\mathcal{M}_{\bar{l}''}^{[b_0b_1]}(\bar{\varphi}_0, \varphi_1; t_0)^*\mathcal{M}_{\bar{l}}^{[b_0b_1]}(\bar{\varphi}_0, \varphi_1; t_F)\mathcal{M}_{\bar{l}'}^{[b_2b_2]}(\varphi_2, \varphi_2; t_0)^* \right\rangle.
\end{aligned} \tag{4.41}$$

This equation is diagrammatically represented in Fig. 4.4. Correlators with two-mesons at the sink and a single meson at the source can be obtained from complex conjugation of these diagrams.

4.3.4 More Complicated Correlators

Clearly, the correlators involving sources and sinks of multiple hadrons are very complicated to evaluate. The number of quark-line diagrams to evaluate grows very quickly with the number of quarks and antiquarks involved. For example, the diagrams that need to be evaluated for a two-meson to two-meson correlator are shown in Fig. 4.5. MAPLE software has been used to assist in these diagram determinations. Diagrams needed for meson-baryon operators can be found in Ref. [15].

4.3.5 Avoiding Biased Estimates

Our temporal correlators are sums of products of quark lines \mathcal{Q} . The stochastic LapH method approximates a single quark line using Eq. (4.15):

$$Q_{ij} = \Omega_{ij}^{-1} = \Omega_{ik}^{-1} \delta_{kj} = \Omega_{ik}^{-1} E[\rho_k \rho_j^*] = E[\Omega_{ik}^{-1} \rho_k \rho_j^*] = E[\varphi_i \rho_j^*]$$

defining $\varphi = \Omega^{-1} \rho$. To simplify notation, we suppress displacement and smearing factors in this section. In practice, we find φ by solving the sparse linear system $\Omega \varphi = \rho$ by the biconjugate gradient method. When approximating a *product* of quark lines, it is important to use independent noises for each quark line, otherwise a biased estimate will be produced. Consider estimating a product of two quark lines:

$$Q_1 Q_2 = Q_1 Q_2 E[\rho^{(1)} \rho^{(1)\dagger}] E[\rho^{(2)} \rho^{(2)\dagger}]. \quad (4.42)$$

In order to express this as a single Monte Carlo estimator, we need to exploit

$$E[\rho^{(1)} \rho^{(1)\dagger}] E[\rho^{(2)} \rho^{(2)\dagger}] = E[\rho^{(1)} \rho^{(1)\dagger} \rho^{(2)} \rho^{(2)\dagger}],$$

but this requires that $\rho^{(1)}$ and $\rho^{(2)}$ are *independent* random noises, in which case

$$\begin{aligned} Q_1 Q_2 &= Q_1 Q_2 E[\rho^{(1)} \rho^{(1)\dagger} \rho^{(2)} \rho^{(2)\dagger}] \\ &= E[\varphi^{(1)} \rho^{(1)\dagger} \varphi^{(2)} \rho^{(2)\dagger}] \\ &\approx \sum_{b_1, b_2} \varphi_1^{(1)[b_1]} \rho_1^{(1)[b_1]\dagger} \varphi_2^{(2)[b_2]} \rho_2^{(2)[b_2]\dagger}. \end{aligned} \quad (4.43)$$

In this form, this expression is consistent with Eq. (4.32) as needed. To construct unbiased stochastic estimates of the products of quark lines, an independent noise is

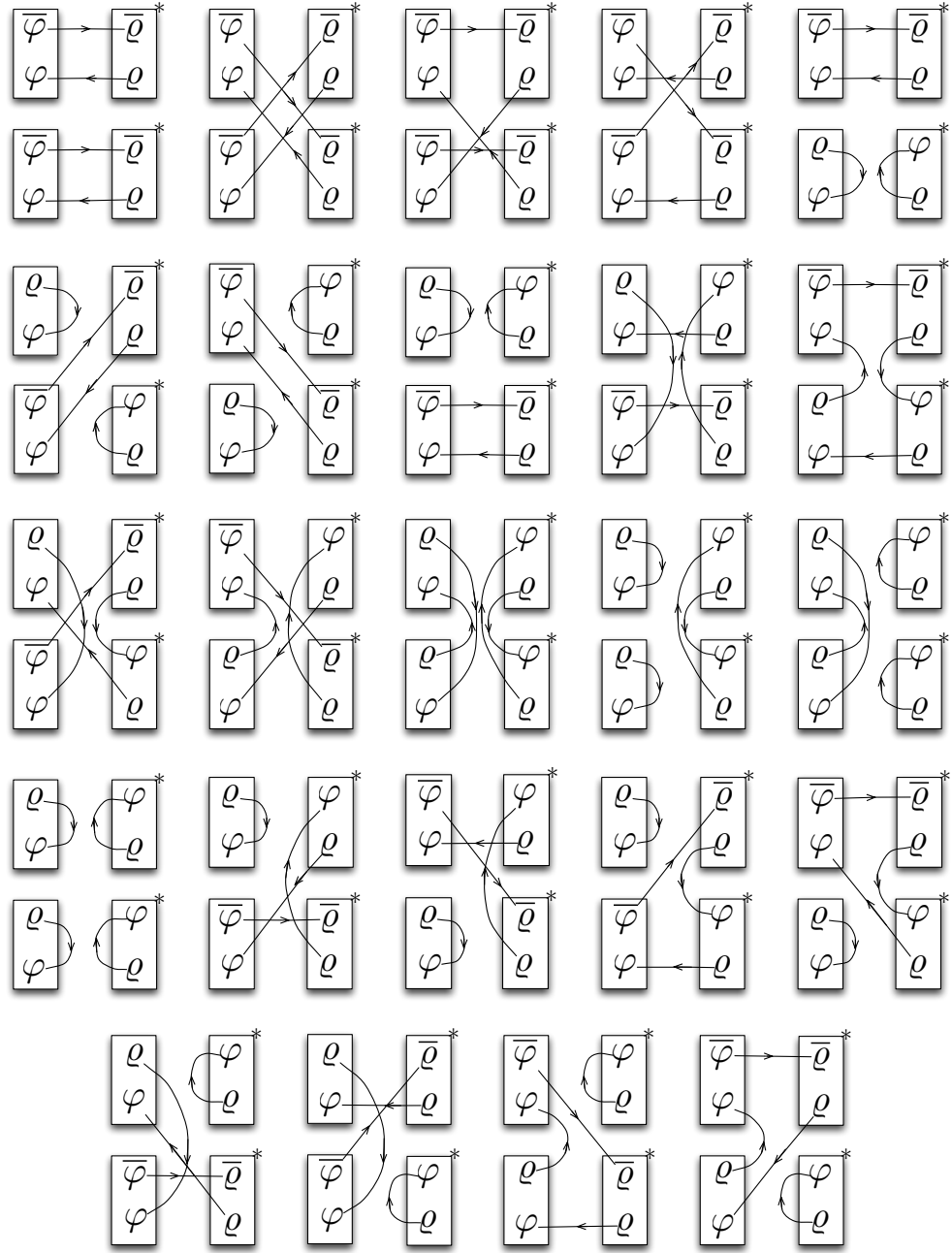


Figure 4.5: The quark line diagrams for a two-meson to two-meson correlator. Lines indicate summations over dilution indices which are nonzero only as long as the two ends of a given line are associated with the same quark flavor.

needed for each quark line.

Our calculations can also benefit from introducing multiple independent noises in another way. We can reuse noises by averaging over the different ways of assigning noises to the different quark lines. For example, in the product of two quark lines Q_1 and Q_2 described above, we can improve the statistics by exchanging noises 1 and 2:

$$Q_1 Q_2 = \frac{1}{2} \sum_{b_1, b_2} \left[\varphi_1^{(1)[b_1]} \rho_1^{(1)[b_1]\dagger} \varphi_2^{(2)[b_2]} \rho_2^{(2)[b_2]\dagger} + \varphi_1^{(2)[b_1]} \rho_1^{(2)[b_1]\dagger} \varphi_2^{(1)[b_2]} \rho_2^{(1)[b_2]\dagger} \right]. \quad (4.44)$$

Computing the solutions φ is the most expensive part of the computations, so reusing the noises and solutions in this way improves statistics with little additional computing effort, provided that the random noises are independent.

In this work, we intend to include multihadron operators up to two-meson operators and meson-baryon operators. Careful consideration of all quark-line diagrams that will be needed indicates that, for the same-time quark lines, two separate random noises are required for light quark lines and two separate noises are needed for the s quark lines, whereas five different random noises are required for the forward/backward quark lines for each quark line flavor. More independent noise vectors would be required if one intended to include three and four particle states.

Chapter 5

Implementation and Analysis

Our method of analyzing the Monte Carlo estimates of the correlators and various implementation details are discussed in this chapter. First, we discuss how we extract energies from our correlator matrix estimates in Sec. 5.1. Details about how we implement the Monte Carlo method and the stochastic LapH method are presented in Sec. 5.2. Quark-field smearing parameters are determined in Sec. 5.3, our selection of single-hadron operators is discussed in Sec. 5.4, and tests of our multi-hadron operators are presented in Sec. 5.5. In Sec. 5.6, we present our procedure for selecting single and multi-hadron operators for use in the symmetry channels of interest, and the operators selected for the $I = \frac{1}{2}$, $S = 1, T_{1u}$ channel are summarized.

5.1 Correlator Matrix Analysis

In this section, we discuss how we extract the energies and other properties of the stationary states of QCD from our Monte Carlo estimates of the temporal correlations of hadron operators.

5.1.1 Noise Reduction

For a set of interpolating operators $\{O_i\}$ that appear in Eq. (2.13), we can define a correlation matrix as

$$\mathcal{C}_{ij}(t) = \langle 0 | O_i(t + t_0) O_j^\dagger(t_0) | 0 \rangle, \quad (5.1)$$

where we replace $t_F = t + t_0$ in Eq. (2.13) and assume $t > 0$ to remove the time ordering operator. In a large matrix of correlations, statistical noise can cause the matrix to

become ill-conditioned, or even to have negative eigenvalues so that the matrix is no longer positive definite. It is important to monitor this and take corrective actions. We do this as follows. Starting with a raw correlation matrix $\mathcal{C}(t)$, we first try to remove the effects of differing normalizations by forming the matrix

$$\mathcal{C}_{ij}(t) \rightarrow \hat{\mathcal{C}}_{ij}(t) = \frac{\mathcal{C}_{ij}(t)}{\sqrt{\mathcal{C}_{ii}(\tau_N)\mathcal{C}_{jj}(\tau_N)}}, \quad (5.2)$$

taking τ_N at a very early time, such as $\tau_N = 3$. We then pick a value $t = \tau_F$ and evaluate the eigenvalues and eigenvectors of $\hat{\mathcal{C}}(\tau_F)$. Since the matrix is Hermitian, the eigenvalues are real and the eigenvectors are orthonormal. Let U_N denote the unitary matrix whose columns are the eigenvectors of $\hat{\mathcal{C}}(\tau_F)$. The columns corresponding to negative eigenvalues must be removed. We also remove the columns corresponding to eigenvalues that are positive, but small. In other words, we remove the columns from U_N for all eigenvalues less than some threshold $\lambda_{\text{threshold}}$. Let P_N denote the projection matrix whose columns are the retained columns (eigenstates) of U_N . We then apply this projection to the correlators to obtain a new correlation matrix $C(t)$:

$$C(t) = P_N^\dagger \hat{\mathcal{C}}(t) P_N. \quad (5.3)$$

The threshold $\lambda_{\text{threshold}}$ is determined as follows. We decide on the largest value of the condition number that is acceptable, denoting this by $\xi_{\text{max}}^{\text{cn}}$. We determine the largest eigenvalue λ_{max} , then since the condition number is the ratio of the largest eigenvalue over the eigenvalue of smallest magnitude, the minimum allowed eigenvalue is

$$\lambda_{\text{threshold}} = \frac{\lambda_{\text{max}}}{\xi_{\text{max}}^{\text{cn}}}. \quad (5.4)$$

Usually $\xi_{\text{max}}^{\text{cn}} < 100$ is a good choice. The above procedure ensures that $C(\tau_F)$ is positive-definite and well conditioned. We also check this for all other t values that we use. Extraction of the energies then proceeds using the refined correlator $C(t)$.

5.1.2 “Rotated” Correlation Matrices

The time evolution of these operators in the Heisenberg picture is described by Heisenberg’s equation $O_i(t) = e^{Ht} O_i e^{-Ht}$. Therefore, each element of the refined correlation

matrix has a spectral decomposition given by

$$\begin{aligned}
C_{ij}(t) &= \sum_n \langle 0|O_i(t+t_0)|n\rangle \langle n|O_j^\dagger(t_0)|0\rangle \\
&= \sum_n \langle 0|O_i|n\rangle \langle n|O_j^\dagger|0\rangle e^{-E_n t} \\
&= \sum_n Z_i^{(n)} Z_j^{(n)*} e^{-E_n t},
\end{aligned} \tag{5.5}$$

where the eigenstate $|n\rangle$ corresponds to eigenvalue E_n relative to vacuum energy. Due to the periodic boundary conditions in finite volume, all eigenstates of H are discrete since all momenta are quantized. The spectral decomposition above assumes that temporal wrap-around effects are insignificant within the time range of interest. The overlap factors above are defined by

$$Z_i^{(n)*} = \langle n|O_i^\dagger|0\rangle, \quad Z_i = \langle 0|O_i|n\rangle, \tag{5.6}$$

and serve as probes to help identify the eigenstates. Further discussions about the use of these overlap factors will be given in Chap. 6.

It is not practical to use Eq. (5.5) to perform fits to all of the correlation matrix elements. Instead, we first solve the eigenvalue problem

$$C(\tau_0)^{-1/2} C(\tau_D) C(\tau_0)^{-1/2} u_n = \lambda_n u_n, \tag{5.7}$$

for $\tau_0 \approx \frac{1}{2}\tau_D$, and τ_D is chosen sufficiently large as discussed below. The above relation requires that $C(\tau_0)$ is positive definite. Define U as the unitary matrix whose columns are the orthonormal eigenvectors u_n , then one can construct a “rotated” correlation matrix

$$\tilde{C}(t) = U^\dagger C(\tau_0)^{-1/2} C(t) C(\tau_0)^{-1/2} U. \tag{5.8}$$

By construction, we have that $\tilde{C}(\tau_0)$ is the identity matrix and $\tilde{C}(\tau_D)$ is a diagonal matrix. It is important to choose τ_D such that all off-diagonal elements of the rotated correlator remain zero within statistical precision for $t > \tau_D$. We can then perform much simpler fits to the diagonal elements $\tilde{C}_{nn}(t)$ and reconstruct the needed overlap factors, as discussed below.

5.1.3 Effective Masses

If the off-diagonal elements of the rotated correlator are consistent with zero for large times, then the diagonal elements of the rotated correlation matrix tend to the form $\tilde{C}_{nn}(t) = A_n e^{-E_n t}$ for large t (ignoring finite temperature temporal wrap-around effects). At small t , contributions from higher-lying states may be nonnegligible.

Good visual tools for monitoring the contributions from higher lying states are the so-called *effective masses*, defined by

$$m_n^{\text{eff}}(t) = -\frac{1}{dt} \ln \left(\frac{\tilde{C}_{nn}(t+dt)}{\tilde{C}_{nn}(t)} \right), \quad (5.9)$$

where dt is a small time separation. In this work, we use $dt = 3$. For large enough t , contributions from higher-lying states become negligible, and the asymptotic form $\tilde{C}_{nn}(t) = A_n e^{-E_n t}$ is attained, resulting in a flat *plateau* in the corresponding effective mass. For earlier times, the effective mass will not be flat, indicating the nonnegligible presence of higher lying states. We will make use of effective masses in Chap. 6 to help describe our spectrum determination.

5.1.4 Fitting the Correlators

The effective mass curves are a good visual tool for showing the signal quality. However, to extract the energies, it is best to fit the diagonal elements of the rotated correlation matrices themselves $\tilde{C}_{nn}(t)$ over a range of large temporal separations $t_{\min} \leq t \leq t_{\max}$ to an appropriate asymptotic form $f(t)$. Such fits are able to take into account all important correlations among the different time slices and different configurations, and are carried out by minimizing the correlated- χ^2 [81] defined by

$$\chi^2 = \sum_{t,t'=t_{\min}}^{t_{\max}} \left[\tilde{C}_{nn}(t) - f(t) \right] \text{Cov}^{-1}(t,t') \left[\tilde{C}_{nn}(t') - f(t') \right], \quad (5.10)$$

with respect to the fit parameters in $f(t)$. The covariance matrix Cov is estimated using a Monte Carlo average over the N configurations, given by

$$\text{Cov}(t,t') \approx \frac{1}{N-1} \left\langle \left[\tilde{C}_{nn}(t) - \langle \tilde{C}_{nn}(t) \rangle \right] \left[\tilde{C}_{nn}(t') - \langle \tilde{C}_{nn}(t') \rangle \right] \right\rangle \quad (5.11)$$

where $\langle \dots \rangle$ represents the average over the N configurations. The covariance matrix is required because the correlators $\tilde{C}(t)$ at different times t are not statistically independent since they are estimated using the same gauge configurations.

We often use the fit form $f_n(t) = A_n e^{-E_n t}$, where the fit parameters are A_n and E_n , but sometimes we use the form $f_n(t) = A_n \cosh(E_n(t - T/2))$, where T is the temporal extent of the lattice, to incorporate the effects of the periodic boundary conditions in the temporal direction. We refer to such fits as “single exponential fits”. The fit range (t_{\min}, t_{\max}) is determined as follows: t_{\max} is chosen as large as possible such that the error in the correlator is still acceptably small, and then t_{\min} is chosen as small as possible such that χ^2/dof , where “dof” stands for “degrees of freedom,” indicates a good fit quality. Our rule of thumb is to require $0.5 < \chi^2/\text{dof} < 1.5$ with the number of time slices in the fit range much greater than the number of parameters in the fit form. We check that the best-fit mass values agree with the effective mass plots in the time ranges used.

Alternatively, the fit form $f_n(t) = A_n e^{-E_n t}(1 + B_n e^{-\Delta_n t})$ can be used. Such fits are known as “two-exponential” fits. The role of the parameters B_n , Δ_n is to absorb the excited-state contamination in the correlator. The fit values of B_n , Δ_n are usually discarded. The main advantage of the two-exponential fits over the single-exponential fits is an insensitivity to t_{\min} . Usually, a much smaller value of t_{\min} can be used, and often, the same t_{\min} value works for a large number of correlators.

Once best-fit values for the parameters E_n and A_n are obtained, we can use the rotation coefficients to evaluate the overlap factors, given by

$$Z_j^{(n)} = [P_N]_{jk} C(\tau_0)_{kl}^{1/2} U_{ln} A_n, \quad (\text{no summation over } n) \quad (5.12)$$

corresponding to the rows and columns of the correlation matrix $C(t)$. Use of the P_N matrix gives the overlaps for the original operator set, modulo a normalization factor for each operator.

5.1.5 Error Analysis Using Resampling Methods

Lattice QCD calculations rely on averages over finite Monte Carlo samples. Monte Carlo estimates of the correlator matrix elements are easily obtained using Eq. 2.52. However, the statistical uncertainties in the best fit parameters, such as energies and overlap factors, are difficult to determine by standard error propagation techniques,

which assume Gaussian distributions. Resampling methods [47], such as the jackknife and bootstrap methods, provide much easier ways to estimate the statistical errors of such parameters.

Bootstrap and jackknife methods usually give us consistent statistical errors. We use the bootstrap method particularly when fitting correlated data as described in Sec. 5.1.4. The average over N extracted values from the original set in each bootstrap sample helps stabilize the fitting parameters and determines the statistical errors of the fitted parameters without complicated error propagation. These two statistical methods are extensively used throughout this work.

Jackknife

The jackknife estimator is defined as follows. Consider an observable f . Let $\langle f \rangle$ represent the average of f using the entire ensemble of N gauge configurations, and define $\langle f \rangle_J$ as the average of f as determined from the ensemble with the J -th configuration removed. Then the jackknife variance is defined by

$$\sigma_J^2(f) = \frac{N-1}{N} \sum_{J=1}^N \left[\langle f \rangle_J - \langle f \rangle \right]^2. \quad (5.13)$$

For such analysis, one quotes the estimate as $\langle f \rangle \pm \sigma_J(f)$.

Bootstrap

The bootstrap estimator is similar to the jackknife. Again, consider an observable f , where $\langle f \rangle$ represents the average of f evaluated using the entire ensemble of N gauge configurations. Define a new “ensemble” B obtained by randomly selecting N of the gauge configurations, allowing for repeats. Let $\langle f \rangle_B$ denote the average of f determined using this bootstrap sample B . Then a bootstrap variance is obtained using

$$\sigma_B^2(f) = \frac{1}{N_b} \sum_{i=1}^{N_b} \left[\langle f \rangle_B - \langle f \rangle \right]^2, \quad (5.14)$$

where N_b is typically chosen to be similar to N in size or larger. One quotes an estimate as $\langle f \rangle \pm \sigma_B(f)$.

5.2 Implementation Details

Our Monte Carlo ensembles of gauge configurations are generated using the USQCD software suite known as QDP++/Chroma[82]. We have developed a C++ software suite called `chroma_laph` that computes the gauge field smearing, quark field smearing, quark sinks and sources, and finally, the single meson and baryon functions. This software links to the QDP++/Chroma library, but parallel MPI input/output routines were written to overcome the I/O limitations of QDP++/Chroma. Finally, C++ software called `last_laph` was written to compute the various quark line diagrams for the single-hadron and multi-hadron correlators, tying together the individual hadron sources and sinks produced by `chroma_laph`.

The computations are carried out in a sequence of tasks, where each task is performed and stored separately for each gauge configuration in the Monte Carlo ensemble:

1) Smeared Gauge Fields \tilde{U}

The spatial link variables are smeared using the stout smearing procedure as described in Sec.3.1. A four-dimensional version of QDP++ is required to read the original gauge configurations, but the spatial smeared gauge fields \tilde{U} are then stored in separate time slices for each gauge configuration. The link variable smearing parameters used [41] are $n_\rho = 10$ and $\rho = 0.10$ in this work.

2) Laplacian Eigenvectors V_s and Smeared Quark Field

The eigenvectors of the smeared Laplacian operator defined in Eq.(3.7) are computed time-slice by time-slice using a Krylov-Spectral Restarted Lanczos (KSRL) method. This method is a modification of the thick restarted Lanczos method described in Ref.[83]. Details of its implementation are described in Ref.[13]. After one obtains the convergent eigenvectors for different time slices, a final reorganization is required to convert the eigenvectors into a four-dimensional format labeled by the level number of the eigenvalues. The eigenvectors corresponding to the lowest N_v eigenvalue magnitudes of the Laplacian are retained [13], where $N_v = 32$ for the $(16^3|390)$ ensemble, $N_v = 64$ for the $(20^3|390)$ ensemble, $N_v = 112$ for the $(24^3|390)$ and $(24^3|240)$ ensembles, and $N_v = 264$ for the $(32^3|240)$ ensemble. These eigenvectors form a smearing matrix of the quark field defined in Eq.(3.11). The corresponding eigenvalue cutoff is $\sigma_s \approx 0.33$, which will be discussed in the next section.

3) Quark Sinks/Sources

The computation of the quark sinks defined in Eq. (4.18) requires the inversion of the Dirac matrix Ω . The stochastic LapH method with dilution enables us to solve the inversion in a smaller LapH subspace with less computation time. For every random Z_4 noise ρ^r projected using a $P^{(b)}$ operator onto a diluted subspace, the solution of the linear equation $\Omega \phi^{r[b]} = V_s P^{(b)} \rho^r$ is obtained using a mixed-precision improved version of the biconjugate gradient method with even-odd preconditioning [84]. If the solution does not reach a convergent result within a certain number of iterations, a slower, but more robust, conjugate gradient solver is applied to the system $\Omega^\dagger \Omega \phi^{r[b]} = \Omega^\dagger V_s P^{(b)} \rho^r$, where $\Omega^\dagger \Omega$ is Hermitian, as required for the conjugate gradient solver. After the solving the linear equation, the quark sinks are obtained by multiplying the eigenvectors $V_s^\dagger \phi^{r[b]}$. These quark-sink results are then stored on disk. There are only $N_t N_v$ elements to store for each noise r and each dilution projector b in each gauge configuration, which dramatically reduces the disk space needed.

The quark sources are obtained by simply applying the projection operators $P^{(b)}$ and the eigenvector matrix V_s onto the random noise ρ^r . Since this multiplication is fast to compute, it is not necessary to store the quark sources on disk. However, in order to reconstruct the quark sources correctly for the already generated quark sinks, the noises must be generated in a systematic and repeatable way. This is achieved by introducing a chosen 16-bit unsigned integer s , combined with the RHMC trajectory number k represented by another 16-bit unsigned integer, producing a 32-bit unsigned integer m that is used as the starting seed for a 32-bit Mersenne twister[85] pseudo random number generator. For one chosen s , we can generate the Z_4 noise $\rho^{(s)}(t, i, \alpha)$ for each Laplacian eigenvector labeled by time t , level i and for each spin index α , starting from the seed m , which ends up being independent for every trajectory. Different choices of s can serve to label the different random noises. When the same seed is used, the same random noise is guaranteed to be reconstructed from the Mersenne twister.

The choice of dilution scheme will be discussed in Sec. 5.3. We choose (TF, SF, LI8) for forward/backward quark lines, and (TI16, SF, LI8) for same-time quark lines.

4) Single-Hadron Functions

The quark sinks and sources are combined and stored in meson functions, as in Eq. (4.31), and baryon functions, as in Eq. (4.37). First of all, the group theoretical coefficients are computed using MAPLE and stored on disk for input by `chroma_laph`. Since the single-hadrons are made out of spatially-displaced quark fields, these coefficients, along with the quark sinks and sources, are combined using proper displacement operators. The displacement operator $D^{(j)}$ and the first part V_s in the smearing matrix $S = V_s V_s^\dagger$ are applied when combining the quark sinks and sources into the hadron functions. The covariant displacement operator involves straightforward multiplications of the smeared gauge field. Low statistics studies[76] led us to choose a displacement length of $3a_s$ for meson functions and $2a_s$ for baryon functions. After the spatial sums, the hadron functions are no longer lattice objects, but multidimensional arrays with dilution indices only. These objects are computed and stored on disk for later combinations into the hadron correlators.

5) Single-Hadron and Multi-hadron Correlation Matrix

The equations for evaluating the temporal correlations have been outlined in Sec. 4.3. Given the large number of correlators that are required in this process for a large variety of flavor combinations of single-hadron and multihadron operators, it is impractical to code up all these Wick contraction diagrams by hand. Instead, MAPLE software was written that encodes the flavor combinations for various isospin and strangeness, as in Table 3.6 and Table 3.7, along with the Wick contractions, and enumerates the needed quark line diagrams. This MAPLE software was used to generate the actual C++ routines that carry out the evaluations of the quark line diagrams. These C++ routines are part of the `last_laph` suite. Averaging over different random noise assignments in the meson and baryon functions is also incorporated into these routines.

There are two other implementation details worth mentioning. First, translational invariance of the lattice QCD action along the time direction can be exploited to improve statistics. For this purpose, we evaluate our temporal correlations at 4 different source times t_0 for the $(24^3|390)$ and $(24^3|240)$ ensembles, whereas for the $(32^3|240)$ ensemble, we choose to average over 8 t_0 values. Secondly, for baryons containing identical quark flavors, such as the Δ^{++} baryons with uuu , the baryon functions can

be evaluated by averaging over all permutations of the quark displacement and spin index assignments to the quark lines of the same flavor. This effectively permutes the random noise assignments, improving the statistics of the temporal correlation evaluations.

5.3 Smearing Parameters and Dilution Scheme

To carry out our computations, we need to decide on quark smearing parameters and the dilution schemes to use.

The effective masses of three representative nucleon operators for temporal separation $t = 1$ are shown in Fig. 5.1. Lower points indicate smaller contributions from unwanted excited states. Thus, we choose a value for the cutoff that yields the lowest $t_s = 1$ effective mass values for a wide variety of operators. The vertical dashed line indicates our choice of $\sigma_s^2 \approx 0.33$, used throughout this work.

The effectiveness of the stochastic LapH method over other stochastic methods can be demonstrated by comparing estimates obtained for a variety of quantities. The stochastic LapH method introduces noise in the LapH subspace, such that ρ has a time index, a spin index, and an index associated with the LapH eigenvectors. Previously developed stochastic methods introduce noise in the full lattice space, such that ρ has spin, time, color, and lattice site indices. Figure 5.2 compares the statistical errors σ obtained for the correlator $C(t = 5)$ associated with a representative triply-displaced-T nucleon operator computed using both LapH and lattice noise for various dilution schemes. Errors are shown as a ratio over the gauge noise error σ_{gn} , defined as the statistical error of the same correlator $C(t = 5)$ using an exact quark propagator method, which is possible on small lattices. The error for an exact quark propagator method comes entirely from the Monte Carlo sampling of gauge configurations. From Fig. 5.2, we observe that the noise ratios σ/σ_{gn} of the LapH method (triangles) are significantly lower than those of the lattice method (squares) for dilution schemes that yield similar numbers of Dirac matrix inversions N_D . The correlators at other time separations and other types of operators also show similarly large error reductions using the stochastic LapH method. These tests were presented in Ref. [13].

A crucial feature of the stochastic LapH method with different dilution schemes is its insensitivity to different volumes. A comparison of the σ/σ_{gn} ratio of the correlator $C(t = 5)$ for the same nucleon triply-displaced-T operator on 16^3 (triangles) and 20^3

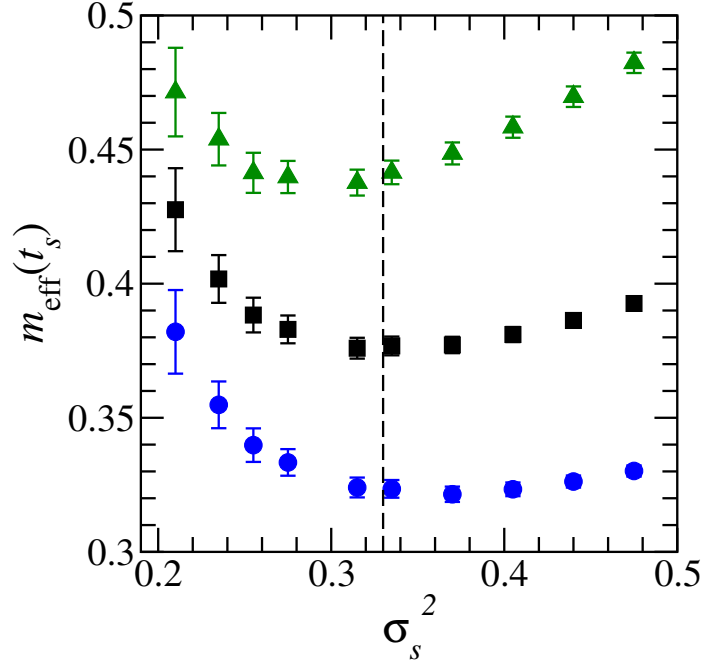


Figure 5.1: The effective masses for three representative nucleon operators at $t_s = 1$ against the LapH smearing cutoff σ_s^2 on the $(16^3|390)$ ensemble. The circles show results (shifted downward by 0.04) for a single-site (SS) operator. The squares correspond to a singly-displaced (SD) nucleon operator, and the triangles are the results (shifted upward by 0.04) for a triply-displaced-T (TDT) operator. The dashed line indicates our choice $\sigma_s^2 \approx 0.33$ [13] for this work.

(squares) lattice is shown in Fig. 5.3. One sees that, for the same number of Dirac matrix inversions N_D for the same dilution scheme applied on different volumes, the error ratio σ/σ_{gn} is not increased very much. As shown in Fig. 5.3, the dilution scheme (TF, SF, LI8) has $\sigma/\sigma_{gn} = 1.31$ for the 16^3 lattice and $\sigma/\sigma_{gn} = 1.32$ for the 20^3 lattice. Recall that the number of LapH eigenvectors needed is 32 for the 16^3 lattice and 64 for 32^3 lattice: for an exact treatment of quark propagation, two times more inversions are required, whereas with the stochastic LapH method, we can use the same number of inversions to achieve comparable error. Moreover, our choice of dilution scheme (TF, SF, LI8) produces error ratios that are very close to unity in the two different volumes, showing that this scheme is a very good approximation to replace an exact treatment. The correlators at other time-separations and other types of operators are also checked to give a consistent conclusion.

A series of tests using different dilution schemes for 16^3 , 20^3 and 24^3 lattices with

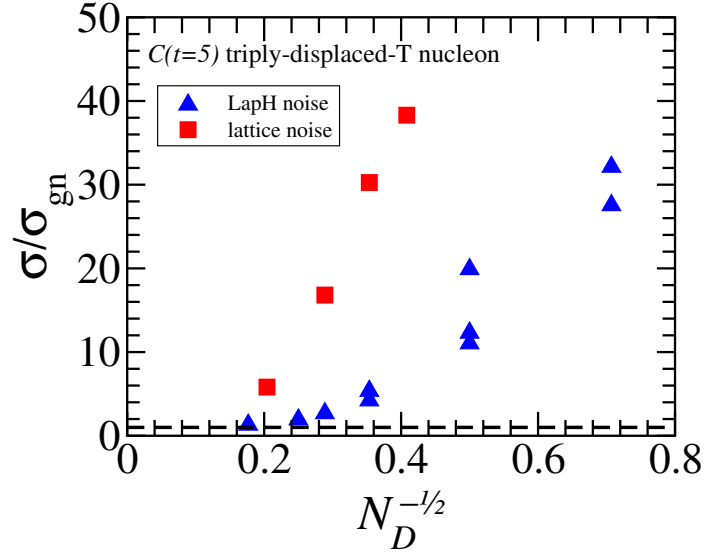


Figure 5.2: Statistical errors σ obtained for the correlator $C(t=5)$ associated with a representative triply-displaced-T nucleon operator computed using both LapH (triangles) and lattice (squares) noise for various dilution schemes, against $N_D^{-1/2}$, where N_D is the required number of inversions of the Dirac matrix. Errors are shown as ratios over the gauge noise σ_{gn} for the $(16^3|240)$ ensemble for a variety of dilution schemes. Results taken from Ref. [13].

different pion masses have been performed to determine the best practical dilution scheme. See Refs. [14, 15, 84] for more details. For the forward/backward quark lines defined in Table 4.1 that connect between sink time t_F and source time t_0 , the scheme (TF, SF, LI8) produced errors close to the gauge noise. This amounts to 128 Dirac matrix inversions for each noise, quark flavor, and configuration, with full time dilution (4) (we use 4 different source time t_0 to improve statistics), full spin dilution (4), and interlace-8 LapH eigenvector dilution (8). For the same-time quark lines that connect the same sink time t_F , the scheme (TI16, SF, LI8) was chosen that is suitable for our calculation. This amounts to 512 Dirac matrix inversions for each noise, quark flavor, and configuration, with interlace-16 time dilution (16), full spin dilution (4) and interlace-8 LapH eigenvector dilution (8). To include multi-hadron operators up to 5 quark systems (in particular, meson-baryon systems), 5 different noises for forward/backward quark lines and 2 noises for same-time quark lines are required for unbiased estimates of all correlators. In other words, $5 \times 128 + 2 \times 512 = 1664$ inversions per configuration per quark flavor are required, compared to 57,344 inversions for the $24^3 \times 128$ ensemble with $N_v = 112$ and 270,336 inversions for the $32^3 \times 256$ ensemble

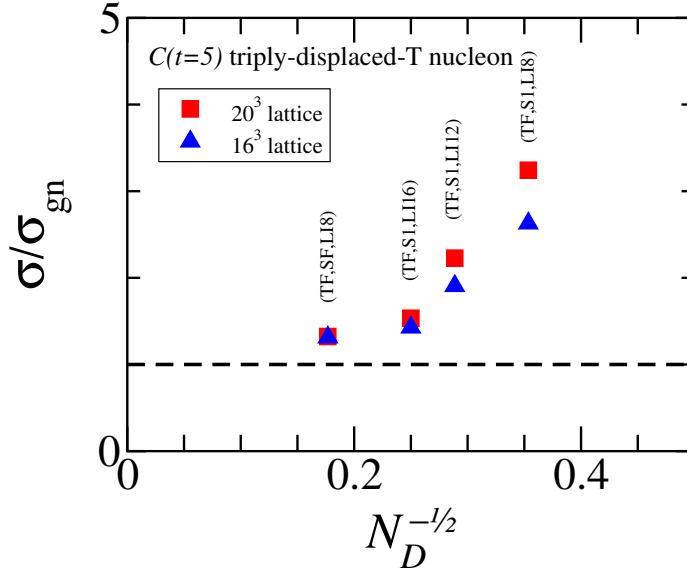


Figure 5.3: Volume dependence of various LapH dilution schemes. The ratios of statistical errors σ over the gauge noise errors σ_{gn} of the correlator $C(t=5)$ for a representative triply-displaced-T nucleon operator is shown against $N_D^{-1/2}$, where N_D is the number of inversions required per source per quark line. Triangles show results on a 16^3 lattice, and squares show results from a 20^3 lattice. Comparison of σ/σ_{gn} between 16^3 and 20^3 reveals very little volume dependence, especially for the (TF, SF, LI8) result. This dilution scheme yields $\sigma/\sigma_{gn} = 1.31$ for 16^3 lattice and $\sigma/\sigma_{gn} = 1.32$ for 20^3 lattice. Plot taken from [13].

with $N_v = 264$ using an exact treatment of quark propagation. This is a huge saving in computation time with only slight increase in error.

5.4 Single-Hadron Operator “Pruning”

Our construction method of assembling single-hadron operators with group-theoretical projections using smeared, covariantly-displaced quark fields as building blocks leads to large numbers of single-hadron operators in each symmetry channel. However, it is not practical to utilize all such operators. Some operators are found to be very noisy, and some couple strongly to unwanted higher-lying states. Also, many of the operators are not sufficiently different from one another, leading to correlation matrices that are ill conditioned. Computation limitations must also be taken into account. Therefore, a procedure of choosing appropriate subsets of operators for use in our final correlation matrices is needed. We refer to the process of choosing such subsets

as operator “pruning”.

Our operator “pruning” procedure, as applied to single-hadron operators in a single symmetry channel, can be summarized as follows:

- 1) In each symmetry channel, we first compute the diagonal elements of the correlation matrix for all operators. Operators that produce a correlator with large statistical errors or whose effective masses appear to plateau at energies above a certain cutoff E_c are discarded.
- 2) The full “raw” correlation matrix $\mathcal{C}_{ij}(t)$ is then computed for the remaining operators.
- 3) We then evaluate the rescaled matrix $\hat{\mathcal{C}}_{ij}(t_P) = \mathcal{C}_{ij}(t_P) (\mathcal{C}_{ii}(t_P)\mathcal{C}_{jj}(t_P))^{-1/2}$ for a small temporal separation t_P . Typically, we use a pruning time separation $t_P = 1$. We then search for a subset of about twenty or so operators that yields a good condition (CN) for $\hat{\mathcal{C}}_{ij}(t_P)$, restricted to that subset of operators. Recall that the condition number of a matrix is the ratio of the maximum eigenvalue magnitude over the minimum eigenvalue magnitude. Usually $\text{CN} < 100$ is a good choice.
- 4) Finally, we verify that the resulting correlation matrix can be diagonalized for a large range of time separations, and that the effective masses associated with the eigenvalues plateau well before being overwhelmed by statistical noise.

The pruning for our single-hadron operators of zero momentum was completed in Ref. [15]. This was performed using the $(16^3|390)$ ensemble with 100 configurations, with energy cutoff $E_c = 0.5a_t^{-1}$. In this work, the operator pruning was extended to single hadrons of nonzero momenta. For single hadrons with nonzero momenta, we assumed that such operators would be used in two-hadron operators, so the energy cutoff we used was lowered to $E_c = [(0.5)^2 - E_\pi(p)^2]^{1/2}a_t^{-1}$, where $E_\pi(p)$ is the energy of a single pion of momentum magnitude $p = |\mathbf{p}|$. Since the number of allowed meson states with different momenta grows very quickly with the cutoff, a lower cutoff greatly reduces the computational resources and disk storage requirements, especially since all irrep rows are needed. Keep in mind that momenta are quantized due to the periodic boundary conditions. We expect the selection of the single-hadron operators should be fairly independent of the lattice volume, except that the energy cutoff leads to very different numbers of operators in the different volumes. In an L^3 spatial lattice, the

	(24 ³ 390)		(24 ³ 240)		(32 ³ 240)	
	N_{op}	N_{mom}	N_{op}	N_{mom}	N_{op}	N_{mom}
π	1776	123	2028	123	2740	149
η	2012	51	2204	51	3078	77
ϕ	2012	51	2204	51	3078	77
K	1499	51	1517	51	1949	65
K^c	1499	51	1517	51	1949	65
N/Δ	1472	33	-	-	1616	59
Λ/Σ	2274	33	-	-	2054	51
Ξ	1320	33	-	-	700	51
Ω	728	33	-	-	680	45

Table 5.1: The numbers N_{op} of single-hadron operators that are selected after the pruning procedure. The number of momenta N_{mom} includes zero, on-axis, planar-diagonal, and cubic-diagonal momenta for each flavor. For the pions, various special directions, such as $(0, 1, 2)$ and $(1, 1, 2)$, are also included. The flavor naming convention follows Table 3.5.

allowed momenta are $2\pi(n_x, n_y, n_z)/L$, for integer n_x, n_y, n_z , so the number of modes that lie below the cutoff increases quickly with increasing volume. The numbers of single-hadron operators retained after the pruning procedure are listed in Table 5.1 for the different lattice volumes we use.

5.5 Multi-hadron Operator Testing

Our two-hadron operators with definite momenta \mathbf{p} are combinations of various single-hadron operators that each have definite momentum \mathbf{p}_a and \mathbf{p}_b , where $\mathbf{p} = \mathbf{p}_a + \mathbf{p}_b$. An alternative design for a two-hadron operator of definite momentum is a summation over all spatial sites of a localized hadron-hadron field with appropriate phases on each site, depending on the total momentum. In such operators, the individual hadron field operators do not create definite momenta. For example, one can design an operator that is a summation over all spatial sites of a localized $\pi\pi$ field in the $I = 2$ channel, given by

$$(\pi\pi)^{A_{1g}^+}(t) = \sum_{\mathbf{x}} \pi^+(\mathbf{x}, t) \pi^+(\mathbf{x}, t), \quad (5.15)$$

where $\pi(\mathbf{x}, t) = \widetilde{\varphi} \gamma_5 \widetilde{\varphi}$, defined using LapH-smearred quark fields. Such an operator creates zero momentum and transforms irreducibly according to the A_{1g}^+ irrep. One can also define an operator in the $I = 1, T_{1u}^+$ irrep by

$$(\pi\pi)^{T_{1u}^+}(t) = \sum_{\mathbf{x}, k=1,2,3} \left[\pi^+(\mathbf{x}, t) \Delta_k \pi^0(\mathbf{x}, t) - \pi^0(\mathbf{x}, t) \Delta_k \pi^+(\mathbf{x}, t) \right], \quad (5.16)$$

where $\Delta_k \pi(\mathbf{x}, t) = \pi(\mathbf{x} + \hat{k}, t) - \pi(\mathbf{x} - \hat{k}, t)$. Such operators, being summations over all spatial sites of a localized $\pi\pi$ field, have total momentum zero, but each constituent pion does not have definite momentum. We refer to such operators as “localized” two-hadron operators.

Figure 5.4 shows the effective masses of localized $\pi\pi$ operators compared to the $\pi\pi$ operators formed from individual π operators that each have a definite momentum. Results from two symmetry channels $I = 2 A_{1g}^+$ and $I = 1 T_{1u}^+$ are shown. This figure demonstrates that the localized $\pi\pi$ operators in both symmetry channels are coupled more to higher excited states at earlier time separations t , as revealed by their effective masses having much larger values. The localized operators also require a much greater time separation for their effective masses to reach their plateau values. Figure 5.4 is dramatic evidence that our approach to constructing two-meson operators is superior to the simpler localized approach.

Compared to the more familiar “localized” operators, multi-hadron operators constructed with individual hadrons of definite momenta have much less excited-state contamination and are easier to make in large numbers. These advantages are the reasons we choose to use them. The method that we use to evaluate the temporal correlations of the single- and multi-hadron operators is known as the *stochastic LapH method*, which is described in Chapter 4. Multi-hadron operators constructed with individual hadrons of definite momenta also have a technical advantage that a storage format for them can be used in the stochastic LapH method that takes up much less disk space.

5.6 Operator Selection in $I = \frac{1}{2}, S = 1, T_{1u}$ Channel

In this initial work, we focus on the resonance-rich $I = \frac{1}{2}, S = 1, T_{1u}$ channel. The $I = 1, S = 0, T_{1u}^+$ channel was also recently studied in Ref. [16].

A large set of single-hadron and multi-hadron operators is required to fully sat-

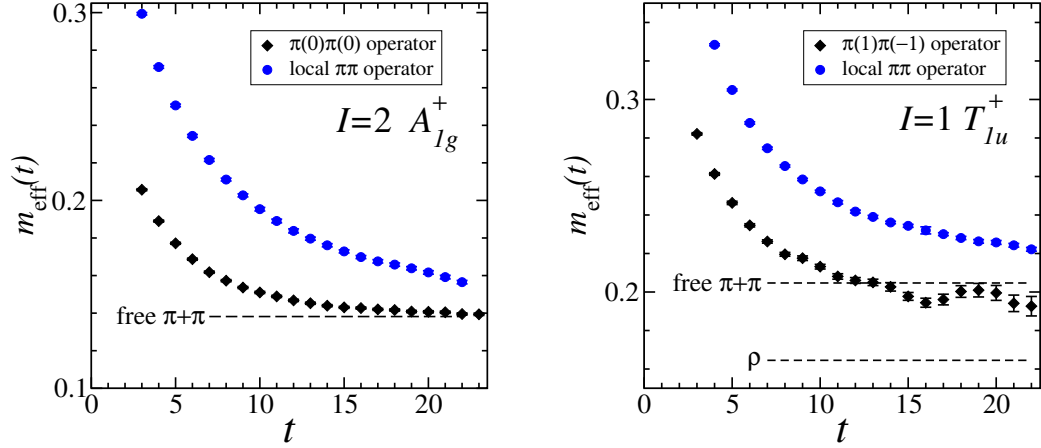


Figure 5.4: The $dt = 3$ effective masses $m_{\text{eff}}(t)$ of two-meson operators with definite momentum and localized $\pi\pi$ operators on the $(24^3|390)$ ensemble. (Left) Effective mass of $I = 2$ $\pi(0)\pi(0)$ operators in the A_{lg}^+ channel using two zero momentum pion single-site operators, along with the localized $\pi\pi$ operator as defined in Eq. (5.15). The horizontal dashed line shows the energy of a free $\pi + \pi$ state from lattice simulation. (Right) Effective mass of $I = 1$ $\pi(1)\pi(-1)$ operators in the T_{lu}^+ channel using two single-site operators, each having one unit of equal and opposite on-axis momentum, along with localized $\pi\pi$ operator as defined in Eq. (5.16). The horizontal dashed lines show the energy of the lowest-lying state ρ in this channel and the free $\pi + \pi$ state in this channel. Plots taken from Ref. [76].

urate all energy levels in this channel below roughly 2 GeV. We have selected a set of less-noisy single-hadron operators with good condition number using the pruning procedure discussed in Sec. 5.4. Extra single-hadron operators with small statistical errors are included to further improve the lowest-lying state extractions. Our choices of single-hadron operators to use are listed in Table 5.2. In this work, 9 single-hadron operators are chosen to ensure appropriate coupling to 4 observed experimental levels.

Selection of our multi-hadron operators is more complicated. First of all, all possible flavor combinations for total isospin $I = \frac{1}{2}$ and strangeness $S = 1$ are K , $K\pi$, $K\eta$, and $K\phi$, as listed in Table 3.6. We have to include multi-hadron operators which are the tensor product of $(I = \frac{1}{2}) \otimes (I = 1)$ ($K\pi$) states and $(I = \frac{1}{2}) \otimes (I = 0)$ ($K\eta, K\phi$) states. On the other hand, all possible combinations with group-theoretical projections onto the T_{lu} irrep add up to a total of 115 combinations. With our choices for the single-hadron operators from the pruning procedure, the total number of operators in this channel adds up to 10722 operators. It is not

Single-Hadron Operators
$K T_{1u}$ SS1
$K T_{1u}$ DDL13
$K T_{1u}$ TDO42
$K T_{1u}$ DDL1
$K T_{1u}$ SD3
$K T_{1u}$ DDL6
$K T_{1u}$ SS0
$K T_{1u}$ DDL5
$K T_{1u}$ DDL18

Table 5.2: List of 9 single-hadron operators used in this work.

practical to use all such operators.

First, small-lattice, low-statistics simulations in all symmetry channels give us the masses and identities of the lightest of the mesons. We confirm these identifications using experimental results from the Particle Data Group [6]. We can combine these single mesons having various momenta in all possible ways to form two-meson states of total zero momentum, then use group theory projections to find all the “expected” two-meson states in each symmetry channel. If the interactions between these mesons are small, then the energies of these two-meson states should be close to their non-interacting energies. This listing of expected levels helps us to choose the two-meson operators that are needed in each symmetry channel. The small-lattice low-statistics simulations also reveal that some single-hadron operators selected from the pruning procedure lead to multi-hadron operators that are either too noisy or plateau well above our 2 GeV threshold, so we avoid such operators in our final choices.

Based on the small-lattice, low-statistics simulations done during the initial pruning procedure, we identify single-hadron operators that couple strongly to the low-lying single-hadron states in each symmetry channel, which we refer to here as “good” single-hadron operators. For each “expected” two-meson level, we form a two-meson operator using these “good” single-hadron operators. These operators formed in this way we refer to as our “primary” multi-hadron operators. For an expected level including an isoscalar meson, we make primary two-meson operators using both $\bar{u}u + \bar{d}d$ and $\bar{s}s$ isoscalar mesons. We follow this procedure for every expected level, starting

from the lowest-lying level and proceeding with increasing expected energy. Some of the expected levels are degenerate states when multiple continuum combinations subduce to the same lattice symmetry channel. We choose different combinations of composite lattice irreducible representations with different single-hadron operators for the same expected level. For some of the lower-lying expected levels, we also form other combinations of single-hadron operators, which we refer to as the “secondary” set. Such operators can help the diagonalizations of the correlators achieve even better saturation of all low-lying states in the Hilbert space.

Tables 5.3, 5.4 and 5.5 list our choices of two-meson operators in the $I = \frac{1}{2}$, $S = 1$, T_{1u} channel of interest obtained following the above procedure. For example, the first two-meson expected level is a combination of a $K(497)$ and a $\pi(140)$ state with opposite momenta having magnitudes of one unit $|P| = 1$ in terms of multiples of $2\pi/L$. We need on-axis (OA) single-hadron operators for this level. The meson $K(497)$ is a spin-0 particle with odd parity, which appears in the A_{1u} stationary irrep. From Table 3.3, we see that the subduction of A_{1u} onto the C_{4v}^D group leads to the A_2 irrep. From our low statistics pruning procedure, we observe that the operator $SS1$ is a “good” operator that couples to the lowest-lying state in this channel. Similarly, $\pi(140)$ is a spin-0 particle with odd parity and g -parity, which corresponds to the A_{1u}^- stationary irrep and the A_2^- on-axis irrep. The operator $SS1$ is a good choice for an operator to produce the lowest-lying state in this channel. Therefore, the combination KA_2SS1 and πA_2^-SS1 with on-axis momenta is expected to have strong coupling to this $K(497) \pi(140)$ state and is our “primary” operator for this level. Meanwhile, the $SS0$ operator in the πA_2^- channel is useful for making additional operators. We choose the combination KA_2SS1 and πA_2^-SS0 as one of the “secondary” multi-hadron operators for the $K(497) \pi(140)$ state.

As another example, the first expected level in Table 5.5 is a combination of $K(497)$ and $\omega(782)$ states with opposite momenta, each having magnitude of two units of momentum $|P| = 2$ in terms of $2\pi/L$. This is a two-fold degenerate state in this channel. We use planar-diagonal (PD) single-hadron operators to construct this state. The state $K(497)$ appears in the A_{1u} stationary irrep, which subduces to the A_2 irrep according to the C_{2v}^D column in Table 3.3. We choose the $SS0$ operator as the lowest-lying single-hadron operator for the planar-diagonal A_2 irrep. On the other hand, the state $\omega(782)$ is an isoscalar spin-1 state with odd parity and g -parity, which appears in the stationary T_{1u}^- irrep, which subduces to C_{2v}^D irreps A_1^- , B_1^-

and B_2^- . However, irrep A_2 combines only with B_1^- and B_2^- to produce an operator that transforms according to the T_{1u} irrep. The choice of lowest-lying operators are $SS1$ for B_1^- irrep and $SS2$ for B_2^- irrep. Therefore, we choose the combinations $KA_2SS0\ \eta B_1^-SS1$ and $KA_2SS0\ \eta B_2^-SS2$ for this expected level. The same operator choices for the isoscalar meson with $\bar{s}s$ flavor structure are used as well.

This work builds on past works presented in several Ph.D. theses [14–16] and publications [13, 76]. My first contribution to the efforts of our group was to the single-hadron operator “pruning” procedure for isovector and kaon flavor sectors described in Ref. [15]. I then extended this procedure to the selection of isoscalar single-meson operators. These selected operators were used to generate and store single-hadron functions for all flavor sectors and symmetry channels using the `chroma_laph` program. I also helped with the production of these single-hadron functions on the $(24^3|390)$, $(24^3|240)$ and $(32^3|240)$ ensembles. I was involved in the numerical tests of `last_laph` program, which was written to compute the various quark line diagrams for the single-hadron and multi-hadron correlation functions. An alternative program modified from `chroma_laph` was used to compute the same correlation function independently. Both results were compared within single precision in every symmetry channel. Finally, my selection of 49 two-meson operators listed in Tables 5.3, 5.4 and 5.5, along with the 9 single-hadron operators listed in Table 5.2, were used to form a 58×58 correlation matrix using the `last_laph` program. My modified version of the analysis code from the research work in Ref. [16] was used to analyze the correlation matrix for extracting the stationary-state energies in the T_{1u} channel.

Expected Levels	Multi-Hadron Operators	Remark
$K(497) \pi(140)$	$K A_2 \text{ SS1 } \pi A_2^- \text{ SS1 } OA$	-
$K(497) \pi(140)$	$K A_2 \text{ SS1 } \pi A_2^- \text{ SS0 } OA$	2^{nd}
$K(497) \pi(140)$	$K A_2 \text{ SS0 } \pi A_2^- \text{ SS0 } OA$	2^{nd}
$K(497) \eta(547)$	$K A_2 \text{ SS1 } \eta A_2^+ \text{ SS1 } OA$	$u\bar{u}$
$K(497) \eta(547)$	$K A_2 \text{ SS1 } \phi A_2^+ \text{ SS1 } OA$	$s\bar{s}$
$K(497) \pi(140)$	$K A_2 \text{ SS0 } \pi A_2^- \text{ SS0 } PD$	-
$K(497) \pi(140)$	$K A_2 \text{ SS1 } \pi A_2^- \text{ SS0 } PD$	2^{nd}
$K(497) \pi(140)$	$K A_2 \text{ SS0 } \pi A_2^- \text{ SS1 } PD$	2^{nd}
$K_1(1270) \pi(140)$	$K T_{1g} \text{ SS0 } \pi A_{1u}^- \text{ SS0}$	-
$K^*(892) \pi(140)$	$K E \text{ SS2 } \pi A_2^- \text{ SS1 } OA$	-
$K^*(892) \pi(140)$	$K E \text{ SS3 } \pi A_2^- \text{ SS1 } OA$	2^{nd}
$K^*(892) \pi(140)$	$K E \text{ SS2 } \pi A_2^- \text{ SS0 } OA$	2^{nd}
$K_1(1400) \pi(140)$	$K T_{1g} \text{ DDL6 } \pi A_{1u}^- \text{ SS0}$	-
$K(497) \rho(770)$	$K A_2 \text{ SS1 } \pi E^+ \text{ SS1 } OA$	-
$K(497) \rho(770)$	$K A_2 \text{ SS0 } \pi E^+ \text{ SS1 } OA$	2^{nd}
$K(497) \rho(770)$	$K A_2 \text{ SS1 } \pi E^+ \text{ SS2 } OA$	2^{nd}

Table 5.3: List of expected two-meson levels in the T_{1u} channel and our choices of two-meson operators. The labels K , π , η , ϕ are as defined in Table 3.5. The back-to-back momenta for the single hadrons are labeled by OA , PD and CD , referring to on-axis, planar-diagonal and cubic-diagonal momentum directions. Little group irreps are listed in Table 3.3. Different irrep combinations are chosen for degenerate expected levels, and we use the label “deg.” to identify such occurrences. Operators from the “secondary” set are indicated by “ 2^{nd} ”. Isoscalar operators are made entirely from either light quarks, indicated by $u\bar{u}$, or entirely from strange quarks, indicated by $s\bar{s}$ in the last column. Continued in Table 5.4.

Expected Levels	Multi-Hadron Operators	Remark
$K(497) \omega(782)$	$K A_2 \text{ SS1 } \eta E^- \text{ SS1 } OA$	$u\bar{u}$
$K(497) \omega(782)$	$K A_2 \text{ SS1 } \phi E^- \text{ SS1 } OA$	$s\bar{s}$
$K(497) \eta(547)$	$K A_2 \text{ SS0 } \eta A_2^+ \text{ SS0 } PD$	$u\bar{u}$
$K(497) \eta(547)$	$K A_2 \text{ SS0 } \phi A_2^+ \text{ SS0 } PD$	$s\bar{s}$
$K(497) \pi(140)$	$K A_2 \text{ SS0 } \pi A_2^- \text{ SS0 } CD$	-
$K(497) h_1(1170)$	$K A_{1u} \text{ SS0 } \eta T_{1g}^- \text{ SS0}$	$u\bar{u}$
$K(497) h_1(1170)$	$K A_{1u} \text{ SS0 } \phi T_{1g}^- \text{ SS0}$	$s\bar{s}$
$K^*(892) \eta(547)$	$K E \text{ SS2 } \eta A_2^+ \text{ SS1 } OA$	$u\bar{u}$
$K^*(892) \eta(547)$	$K E \text{ SS2 } \phi A_2^+ \text{ SS1 } OA$	$s\bar{s}$
$K^*(892) \pi(140)$	$K B_1 \text{ SS1 } \pi A_2^- \text{ SS0 } PD$	deg.
$K^*(892) \pi(140)$	$K B_2 \text{ SS3 } \pi A_2^- \text{ SS0 } PD$	deg.
$K(497) \eta'(958)$	$K A_2 \text{ SS1 } \eta A_2^+ \text{ SS0 } OA$	$u\bar{u}$
$K(497) \eta'(958)$	$K A_2 \text{ SS1 } \phi A_2^+ \text{ SS0 } OA$	$s\bar{s}$
$K(497) b_1(1235)$	$K A_{1u} \text{ SS0 } \pi T_{1g}^+ \text{ SS0}$	-
$K(497) a_1(1260)$	$K A_{1u} \text{ SS0 } \pi T_{1g}^- \text{ SS0}$	-
$K(497) \phi(1020)$	$K A_2 \text{ SS1 } \eta E^- \text{ SS2 } OA$	$u\bar{u}$
$K(497) \phi(1020)$	$K A_2 \text{ SS1 } \phi E^- \text{ SS2 } OA$	$s\bar{s}$
$K(497) \rho(770)$	$K A_2 \text{ SS0 } \pi B_1^+ \text{ SS1 } PD$	deg.
$K(497) \rho(770)$	$K A_2 \text{ SS0 } \pi B_2^+ \text{ SS2 } PD$	deg.

Table 5.4: Continued from Table 5.3. List of expected two-meson levels in the T_{1u} channel and our choices of two-meson operators. The labels K , π , η , ϕ are as defined in Table 3.5. The back-to-back momenta for the single hadrons are labeled by OA , PD and CD , referring to on-axis, planar-diagonal and cubic-diagonal momentum directions. Little group irreps are listed in Table 3.3. Different irrep combinations are chosen for degenerate expected levels, and we use the label “deg.” to identify such occurrences. Operators from the “secondary” set are indicated by “2nd”. Isoscalar operators are made entirely from either light quarks, indicated by $u\bar{u}$, or entirely from strange quarks, indicated by $s\bar{s}$ in the last column. Continued in Table 5.5.

Expected Levels	Multi-Hadron Operators	Remark
$K(497) \omega(782)$	$K A_2 \text{ SS0 } \eta B_1^- \text{ SS1 } PD$	$u\bar{u}$; deg.
$K(497) \omega(782)$	$K A_2 \text{ SS0 } \eta B_2^- \text{ SS2 } PD$	$u\bar{u}$; deg.
$K(497) \omega(782)$	$K A_2 \text{ SS0 } \phi B_1^- \text{ SS1 } PD$	$s\bar{s}$; deg.
$K(497) \omega(782)$	$K A_2 \text{ SS0 } \phi B_2^- \text{ SS2 } PD$	$s\bar{s}$; deg.
$K(497) f_1(1285)$	$K A_{1u} \text{ SS0 } \eta T_{1g}^+ \text{ SS0}$	$u\bar{u}$
$K(497) f_1(1285)$	$K A_{1u} \text{ SS0 } \phi T_{1g}^+ \text{ SS0}$	$s\bar{s}$
$K_1(1270) \pi(140)$	$K A_2 \text{ SS0 } \pi A_2^- \text{ SS1 } OA$	deg.
$K_1(1270) \pi(140)$	$K E \text{ SS0 } \pi A_2^- \text{ SS1 } OA$	deg.
$K_1(1270) \eta(547)$	$K T_{1g} \text{ SS0 } \eta A1u^+ \text{ SS0}$	$u\bar{u}$
$K_1(1270) \eta(547)$	$K T_{1g} \text{ SS0 } \phi A1u^+ \text{ SS0}$	$s\bar{s}$
$K(497) \eta(547)$	$K A_2 \text{ SS0 } \eta A_2^+ \text{ SS0 } CD$	$u\bar{u}$
$K(497) \eta(547)$	$K A_2 \text{ SS0 } \phi A_2^+ \text{ SS0 } CD$	$s\bar{s}$
$K(497) \pi(140)$	$K A_2 \text{ SS1 } \pi A_2^- \text{ SS1 } OA(2)$	-
$K^*(892) a_0(980)$	$K T_{1u} \text{ SS1 } \pi A_{1g}^- \text{ SS0}$	-

Table 5.5: Continued from Table 5.4. List of expected two-meson levels in the T_{1u} channel and our choices of two-meson operators. The labels K , π , η , ϕ are as defined in Table 3.5. The back-to-back momenta for the single hadrons are labeled by OA , PD and CD , referring to on-axis, planar-diagonal and cubic-diagonal momentum directions. The label $OA(2)$ refers to a single hadron with two units of momentum. Little group irreps are listed in Table 3.3. Different irrep combinations are chosen for degenerate expected levels, and we use the label “deg.” to identify such occurrences. Operators from the “secondary” set are indicated by “ 2^{nd} ”. Isoscalar operators are made entirely from either light quarks, indicated by $u\bar{u}$, or entirely from strange quarks, indicated by $s\bar{s}$ in the last column.

Chapter 6

Isodoublet strangeness $S = 1$ T_{1u} Spectroscopy Results

The first exploratory results in the $I = 1$, $S = 0$, T_{1u}^+ channel using a large set of single-hadron and two-hadron operators was presented in Ref. [16]. More than 50 energy levels were extracted from a large correlation matrix in that study. We extend that work with an exploratory study of the energy spectrum in the $I = \frac{1}{2}$, $S = 1$, T_{1u} channel, focusing on the analysis of the $(24^3|390)$ ensemble. Although we determine the energies of 57 stationary states in the finite volume of the 24^3 lattice, most of these states are dominated by two-meson Fock components. Our main interest lies in identifying the kaon resonance “precursor” states, the stationary states in finite volume that we expect to evolve into the resonances as the volume increases.

According to the Particle Data Group [6], there are three known isodoublet strangeness $S = 1$ spin-1 resonance states with odd parity, labeled as $K^*(892)$, $K^*(1410)$ and $K^*(1680)$, respectively. These states are expected to appear in the T_{1u} channel in a cubic box with periodic boundary conditions. A fourth state with spin-3 and odd parity, known as $K^*(1780)$, also appears in the T_{1u} irreducible representation, according to Table. 3.4. There are two unconfirmed [6] higher spin-4 and spin-5 states that also appear in this channel. These states are associated with energies above 2 GeV. The relativistic quark model in Ref. [7] also predicts four $\bar{q}q$ states below 2 GeV. In this work, we focus on the single-hadron resonance states, targeting the states below 2 GeV that have spin-1 or spin-3.

We present our results in this chapter. In Sec. 6.1, we extract the stationary-state energies from our correlation matrix, evaluated using the operator set selected in

Sec. 5.6. Our analysis follows the procedure outlined in Sec. 5.1. Our identifications of the extracted levels are discussed in Sec. 6.2 using overlap factors, and the spectrum of “precursor” resonant states is presented and compared with experiment.

6.1 Analysis of Correlation Matrix

We now turn to the extractions of the stationary-state energies. The analysis of our correlation matrix follows the procedure described in Sec. 5.1. Starting with the raw 58×58 correlation matrix $\mathcal{C}_{ij}(t)$ in the T_{1u} channel, we first remove irrelevant normalization factors by defining the correlation matrix $\hat{\mathcal{C}}_{ij}(t)$ using Eq. (5.2) and choosing $\tau_N = 3$. After this, we inspect the eigenvalues of $\hat{\mathcal{C}}(t_F)$ at time $\tau_F = 4$ to perform a first noise reduction step. Most of the eigenvalues are of order unity, but a few turn out to be smaller. By choosing $\lambda_{\text{threshold}} = 0.05$, we drop one eigenvector with an uncomfortably small eigenvalue. The resulting condition number is roughly 66. We then apply the noise reduction projection operator P_N onto the remaining 57 eigenvectors using Eq. (5.3), ending up with a 57×57 correlation matrix $C_{ij}(t)$.

The next step is to solve the generalized eigenvalue problem, defined in Eq. (5.7), using the noise-reduced correlation matrix $C_{ij}(t)$. We try a variety of choices for τ_0 and τ_D . For each choice, we compute the “rotation” matrix U , then construct the rotated correlation matrix $\tilde{\mathcal{C}}_{ij}(t)$ using Eq. (5.8). Note that the same matrix U is applied to all time slices. We then examine all off-diagonal elements of the rotated correlator for all $t > \tau_D$ to see if they are all statistically consistent with zero. We do this as follows. First, we evaluate the quantities

$$|\tilde{\mathcal{C}}_{ij}^{(N)}(t)| = |\tilde{\mathcal{C}}_{ij}(t)| (\tilde{\mathcal{C}}_{ii}(t)\tilde{\mathcal{C}}_{jj}(t))^{-1/2}, \quad (6.1)$$

and their jackknife errors $\text{Err}[|\tilde{\mathcal{C}}_{ij}^{(N)}(t)|]$ are also computed. We then evaluate the ratios $\sum_t |\tilde{\mathcal{C}}_{ij}^{(N)}(t)| / \text{Err}[|\tilde{\mathcal{C}}_{ij}^{(N)}(t)|]$, which sums over all available time slices. An inspection of the largest 20 such ratio values leads us to choose $\tau_0 = 4$ and $\tau_D = 11$ in this work. Our guiding principle is to find the smallest values of τ_0 and τ_D that produce correlators whose off-diagonal elements are all statistically consistent with zero. A plot of $|\tilde{\mathcal{C}}_{ij}^{(N)}(t)|$ for the largest five elements using $\tau_0 = 4$ and $\tau_D = 11$ is shown in Fig. 6.1.

Since the rotated correlation matrix stays diagonal for all time separations $t > \tau_D$

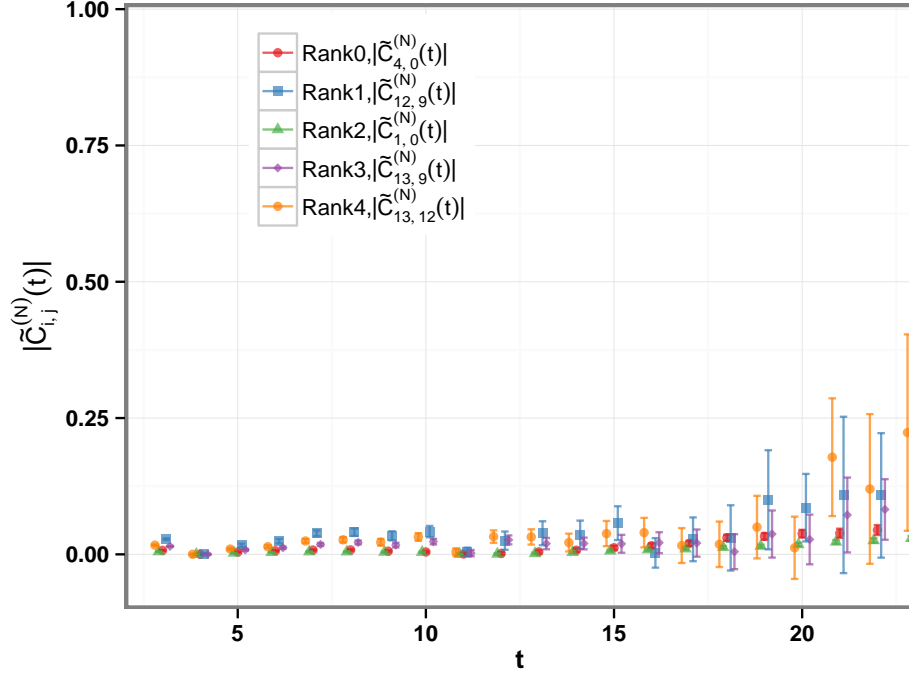


Figure 6.1: The five largest off-diagonal elements of the rotated correlation matrix normalized at every time defined by Eq. (6.1). The ranking of the off-diagonal elements is determined as described in the text. Since the diagonalization procedure used $t = \tau_0 = 4$ and $t = \tau_D = 11$, the rotated correlator is exactly diagonal at these times. One sees that the off-diagonal elements are all statistically consistent with zero for other times $t > \tau_D$.

of interest, we can use correlated- χ^2 fits to extract energy levels from the diagonal elements of the rotated matrix. The correlated- χ^2 fit procedure is described in Sec. 5.1.4. Our method of determining the range of times t_{\min} to t_{\max} to use in each fit is as follows: t_{\max} is chosen as large as possible such that the error in the correlator is still acceptably small, and then t_{\min} is chosen as small as possible such that χ^2/dof , where “dof” stands for “degrees of freedom,” indicates a good fit quality. The choice of t_{\max} is usually very straightforward and does not vary much for different energy levels, but for the single-exponential fit the determination of t_{\min} is sometimes fraught with subjectiveness and can change appreciably depending on the energy level. For the large number of energy levels to be studied, determining t_{\min} values for all levels can be time consuming and tedious. However, we have found that the fitting process can

be significantly improved and simplified by using “two-exponential” forms

$$f(t) = A_n e^{-E_n t} (1 + B_n e^{-\Delta_n^2 t}), \quad (6.2)$$

where the primary decay term $A_n e^{-E_n t}$ dominates at larger times, and the role of the parameters B_n, Δ_n in the secondary decay term $e^{-(E_n + \Delta_n^2)t}$ is to mock up the excited-state contamination at smaller times. Note that we never use the best-fit values of B_n and Δ_n in any way other than as a tool to help expose the primary decay term (the “signal”), obscured by the higher-lying unwanted contributions (the “background”). A major advantage of the two-exponential fits is an insensitivity to t_{\min} . We find that t_{\min} values of 3 or 4 lead to acceptable χ^2/dof (around unity) for all levels.

We have successfully extracted 57 levels from the 57×57 correlation matrix $C_{ij}(t)$ in the T_{1u} channel. For most levels, we used $t_{\min} = 3$ and $t_{\max} = 20$ to perform two-exponential fits, obtaining reasonable χ^2/dof values. A few levels required a small change in t_{\min} and t_{\max} to produce a χ^2/dof within the range $0.5 - 1.5$. Two-exponential fits failed for level 56, so we used a single-exponential fit with $t_{\min} = 3$ and $t_{\max} = 8$. We included all single-meson and two-meson operators needed to reliably determine energies lying below an upper limit $0.5 a_t^{-1}$, so since this level is well above our upper limit, we view the extraction of this level as tentative.

The $dt = 3$ effective masses associated with the diagonal elements of the rotated correlator matrix are shown in Figs. 6.2, 6.3, 6.4, 6.5 and 6.6. The levels $0, 1, 2, \dots$ are indexed in order of increasing energy fit value, which is listed in the upper right corner of each plot and shown by horizontal dashed lines, indicating the upper and lower bound of the bootstrap error. The horizontal range of the dashed lines indicates the t_{\min} and t_{\max} used for each level. The two-exponential best-fit function is shown as a red dashed-dotted line in each plot, which agrees well with the Monte Carlo points in all cases.

6.2 Level Identification and Spectrum

With such a large number of energies extracted, level identification becomes a key issue. QCD is a complicated interacting quantum field theory, so characterizing its stationary states in finite volume is not likely to be done in a simple way. Level identification must be inferred from the Z overlaps factors of our probe operators,

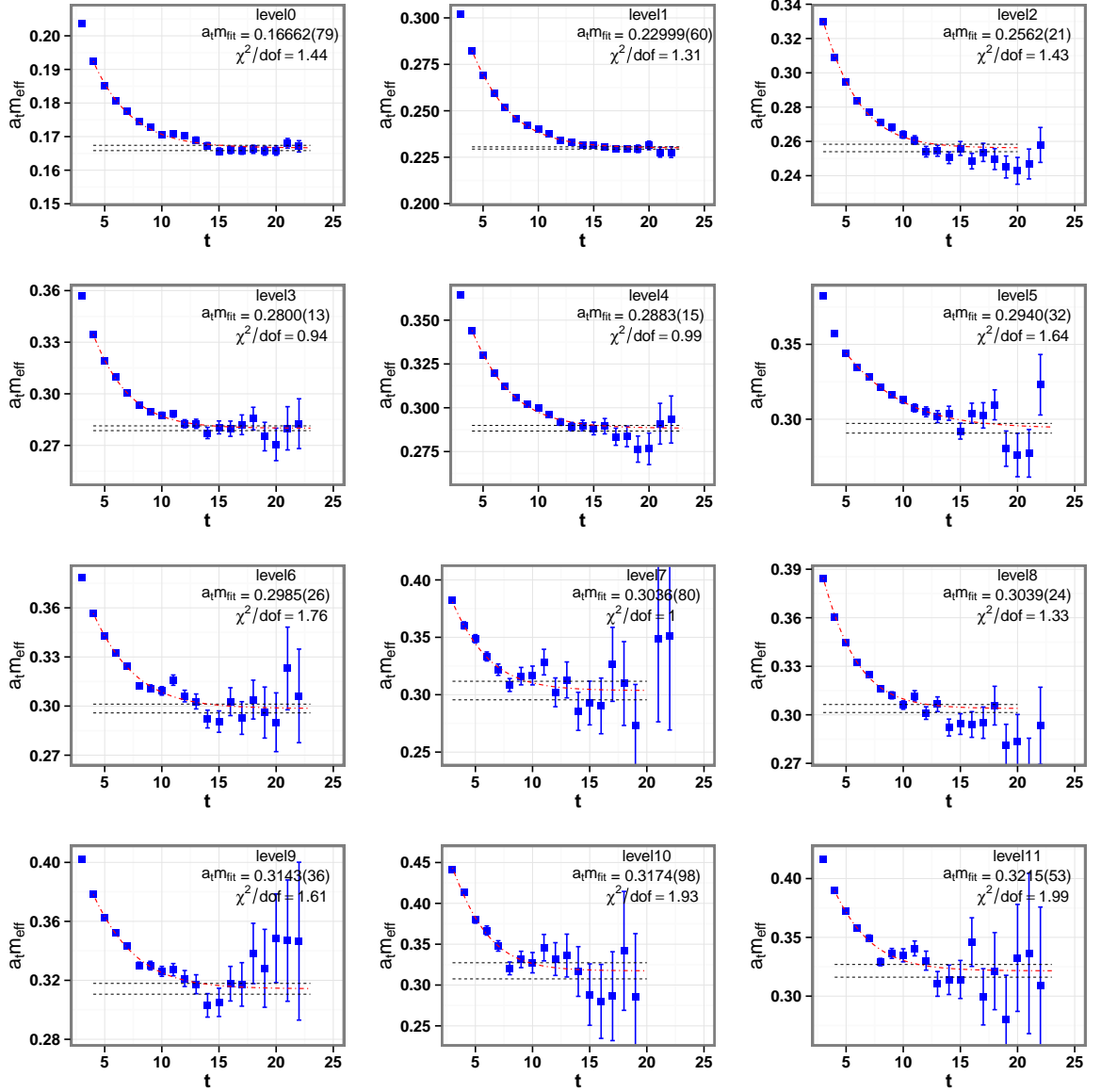


Figure 6.2: The $dt = 3$ effective masses $m_{\text{eff}}(t)$ of the diagonal elements of the rotated correlation matrix corresponding to the lowest 12 energies, in order of increasing energy. The red dashed-dotted line in each plot shows the best-fit two-exponential function with χ^2 per degree of freedom listed in the top right corner. The two horizontal black dashed lines in each plot show the best fit energy, with the vertical spacing between the lines indicating the statistical uncertainty.

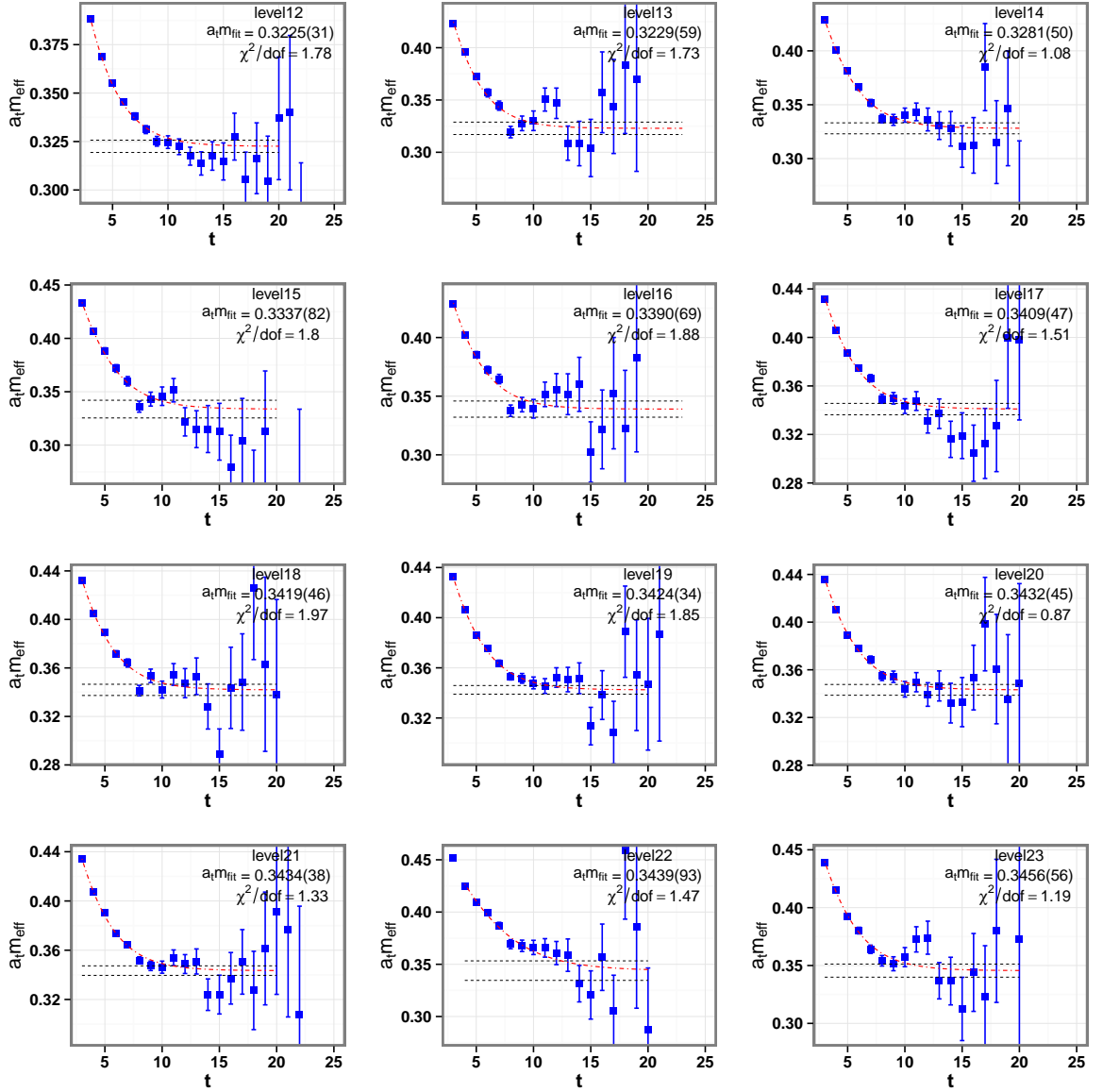


Figure 6.3: The $dt = 3$ effective masses $m_{\text{eff}}(t)$ of the diagonal elements of the rotated correlation matrix corresponding to levels 12 to 23, in order of increasing energy. The red dashed-dotted line in each plot shows the best-fit two-exponential function with χ^2 per degree of freedom listed in the top right corner. The two horizontal black dashed lines in each plot show the best fit energy, with the vertical spacing between the lines indicating the statistical uncertainty.

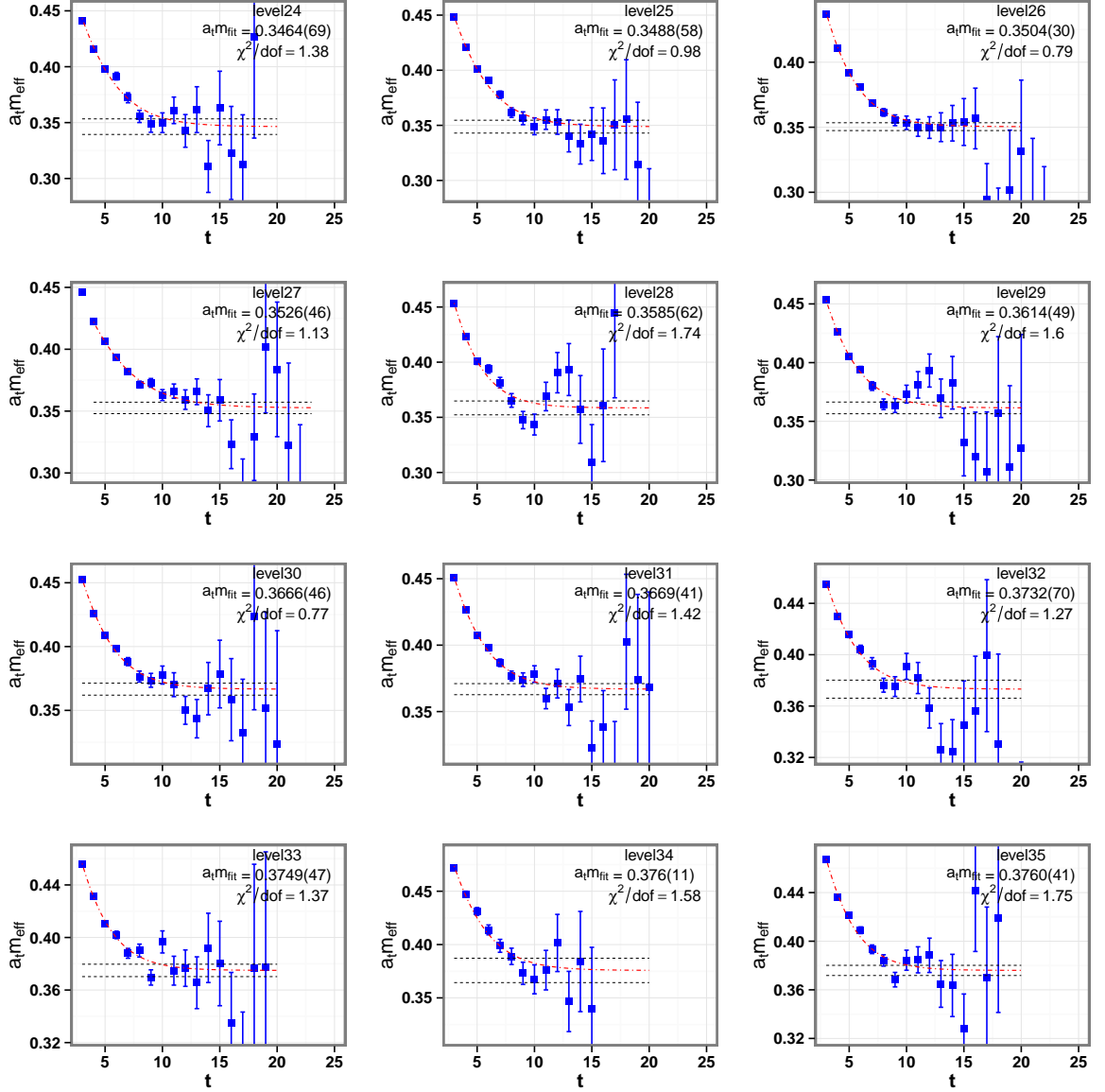


Figure 6.4: The $dt = 3$ effective masses $m_{\text{eff}}(t)$ of the diagonal elements of the rotated correlation matrix corresponding to levels 24 to 35, in order of increasing energy. The red dashed-dotted line in each plot shows the best-fit two-exponential function with χ^2 per degree of freedom listed in the top right corner. The two horizontal black dashed lines in each plot show the best fit energy, with the vertical spacing between the lines indicating the statistical uncertainty.

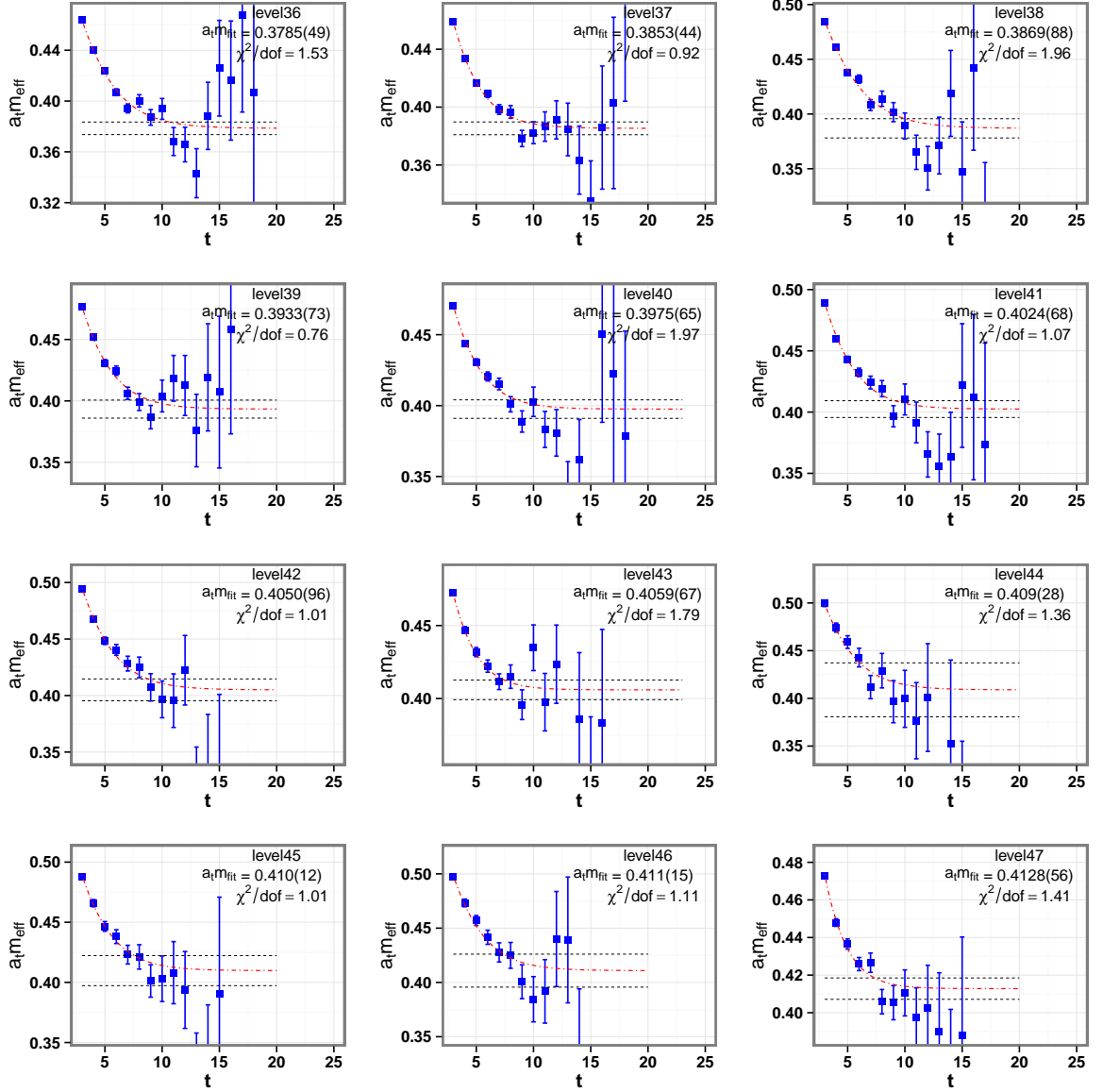


Figure 6.5: The $dt = 3$ effective masses $m_{\text{eff}}(t)$ of the diagonal elements of the rotated correlation matrix corresponding to levels 36 to 47, in order of increasing energy. The red dashed-dotted line in each plot shows the best-fit two-exponential function with χ^2 per degree of freedom listed in the top right corner. The two horizontal black dashed lines in each plot show the best fit energy, with the vertical spacing between the lines indicating the statistical uncertainty.

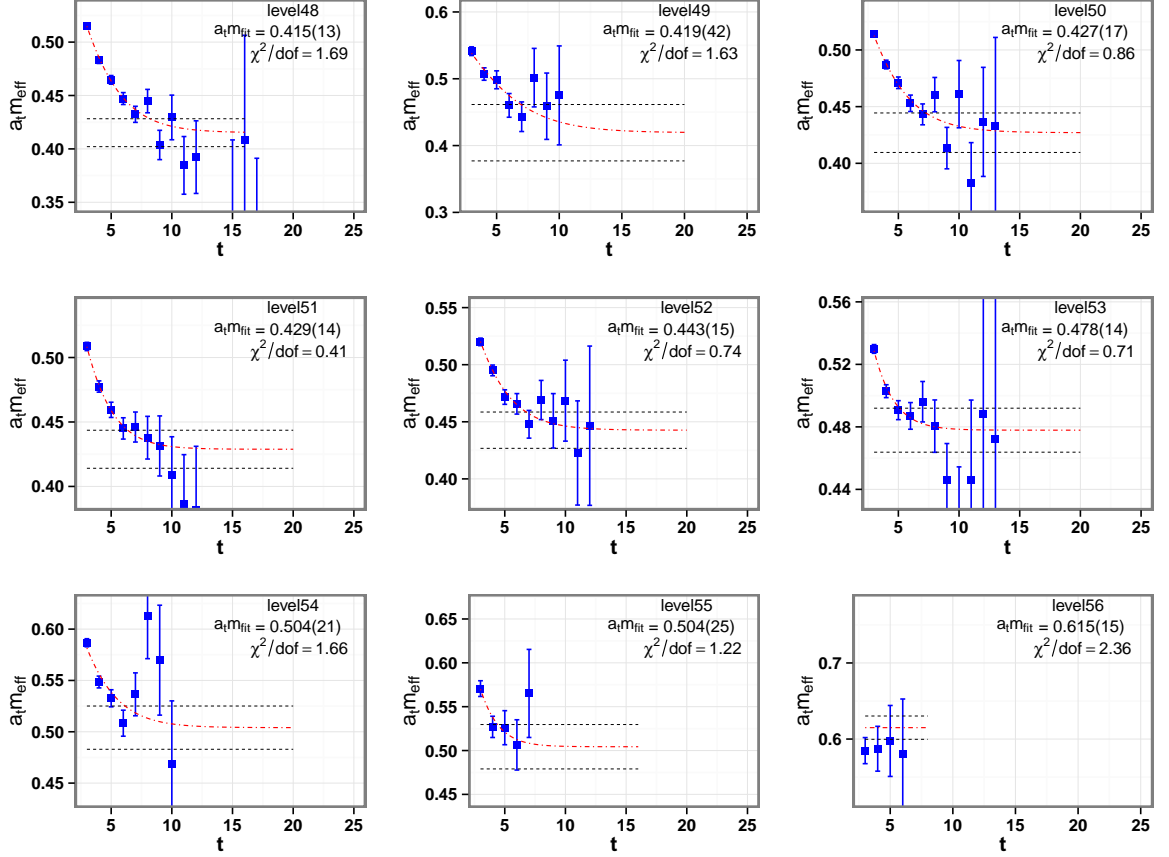


Figure 6.6: The $dt = 3$ effective masses $m_{\text{eff}}(t)$ of the diagonal elements of the rotated correlation matrix corresponding to levels 48 to 56, in order of increasing energy. The red dashed-dotted line in each plot shows the best-fit two-exponential function (except level 56) with χ^2 per degree of freedom listed in the top right corner. The two horizontal black dashed lines in each plot show the best fit energy, with the vertical spacing between the lines indicating the statistical uncertainty.

analogous to deducing resonance properties from scattering cross sections in experiments. Although we are in control of the probe operators \overline{O}_j which act on the vacuum to create “probe states” $|\Phi_j\rangle \equiv \overline{O}_j|0\rangle$, we have limited knowledge and control of the probe states so produced. Judiciously chosen probe operators, constructed from smeared fields, should excite the low-lying states of interest, with hopefully little coupling to unwanted higher-lying states, and help with classifying the levels extracted. Small- a classical expansions can help to characterize the probe operators, and hence, the states they produce.

The overlap factors $Z_j^{(n)} = \langle 0|O_j|n\rangle$ describe the coupling of an operator O_j to the stationary states $|n\rangle$. Using the fitted amplitude A_n of the primary decay from Sec. 6.1, we estimate the overlap factors for each operator according to Eq. (5.12). Note that since we use the noise-reduced correlation matrix to solve the generalized eigenvalue problem, we have to project back to the original set using the projection operator P_N .

Figures 6.7, 6.8, 6.9 and 6.10 show the magnitude squares of the overlap factors $|Z_j^{(n)}|^2$ for various two-meson operators. In each plot, magnitudes squared are shown against the energy eigenstate number N ordered by increasing energy. Since our hadronic operators are constructed from smeared fields, we expect that they should have little coupling to higher-lying states ($N > 56$). For the operators with a single dominant peak in its overlap factor plot, we can identify the dominant level as the state that we expect the operator to create.

For example, the first plot in Fig. 6.7 shows the overlap factors for a particular probe operator which we expect predominantly creates a $K\pi$ state having back-to-back on-axis momenta of unit magnitude (in units of $2\pi/L$). We observe a single dominant peak at level 1. Hence, we identify level 1 as a stationary state dominated by a $K\pi$ state having back-to-back on-axis momenta of unit magnitude. The second plot shows the overlap factors for another $K\pi$ operator that is similar to the first operator, but this operator belongs to the “secondary” set of $K\pi$ operators and is constructed using displacement types different from that used in the operator in the first plot. There is a significant peak at level 1, confirming our identification of level 1. This operator also has large overlap factors for levels 36 and 37, suggesting a significant excited $K\pi$ component for those levels.

The plot in the second row, third column in Fig. 6.7 shows the overlaps for a probe operator that we expect predominantly creates a $K\pi$ state having back-to-back

planar-diagonal momenta of two units of magnitude (in units of $2\pi/L$). We observe a single peak at level 3, provoking the identification of level 3 as a stationary state dominated by a $K\pi$ state having back-to-back planar-diagonal momenta of minimal magnitude. Two secondary operators shown in the next two plots also have large overlaps at level 3, which confirms this identification.

The same identification procedure can be applied to many of the other two-meson operators. However, we do observe some two-meson operators with multiple peaks, which makes the classification of some levels problematic. Also, we expect the stationary states of this fully interacting quantum field theory to be rather complicated superposition of various Fock states, so a simple level identification may not be possible in all cases. A comparison of the interacting energy with free two-meson energies can also help with identification. Our interest here lies more in identifying the resonance “precursor” states, so we leave a more detailed study of the two-meson levels to future work.

To identify the resonance precursor states, it is best to use probe operators that create such states without creating other states. We have found that the best way to construct such probe operators is to use “optimized” linear combinations of our single-hadron operators. We limit our attention to the 9×9 correlator submatrix involving only the 9 single-hadron operators. We follow the same noise reduction and optimization rotation as in Sec. 6.1, with the same choice of τ_0 , τ_D and τ_F . This defines a single-hadron rotation matrix \tilde{U} and noise reduction projector \tilde{P}_N , then our “optimized” single-hadron (SH) operators \tilde{O}_m are linear combinations of the original single-hadron operators O_j given by $\tilde{O} = \tilde{U}^\dagger \tilde{P}_N^\dagger O$. The index m now labels the optimized probe operators, and the single-hadron-optimized (SH-optimized) overlap factors are given by

$$\tilde{Z}_m^{(n)} = \langle 0 | \tilde{O}_m | n \rangle = \tilde{U}_{mk}^* [\tilde{P}_N]_{kj}^* Z_j^{(n)}, \quad (\text{for } j \in \{\text{SH}\}). \quad (6.3)$$

In this work, 8 SH-optimized operators are constructed from the original 9 single-meson operators. From these SH-optimized overlap factors, we can identify the levels that dominate the finite-volume stationary states expected to evolve into the single-meson resonances in infinite volume. Again, we call such states “resonance precursor states”.

The top plot in Fig. 6.11 shows the magnitudes squared $|\tilde{Z}_m^{(n)}|^2$ of the overlap

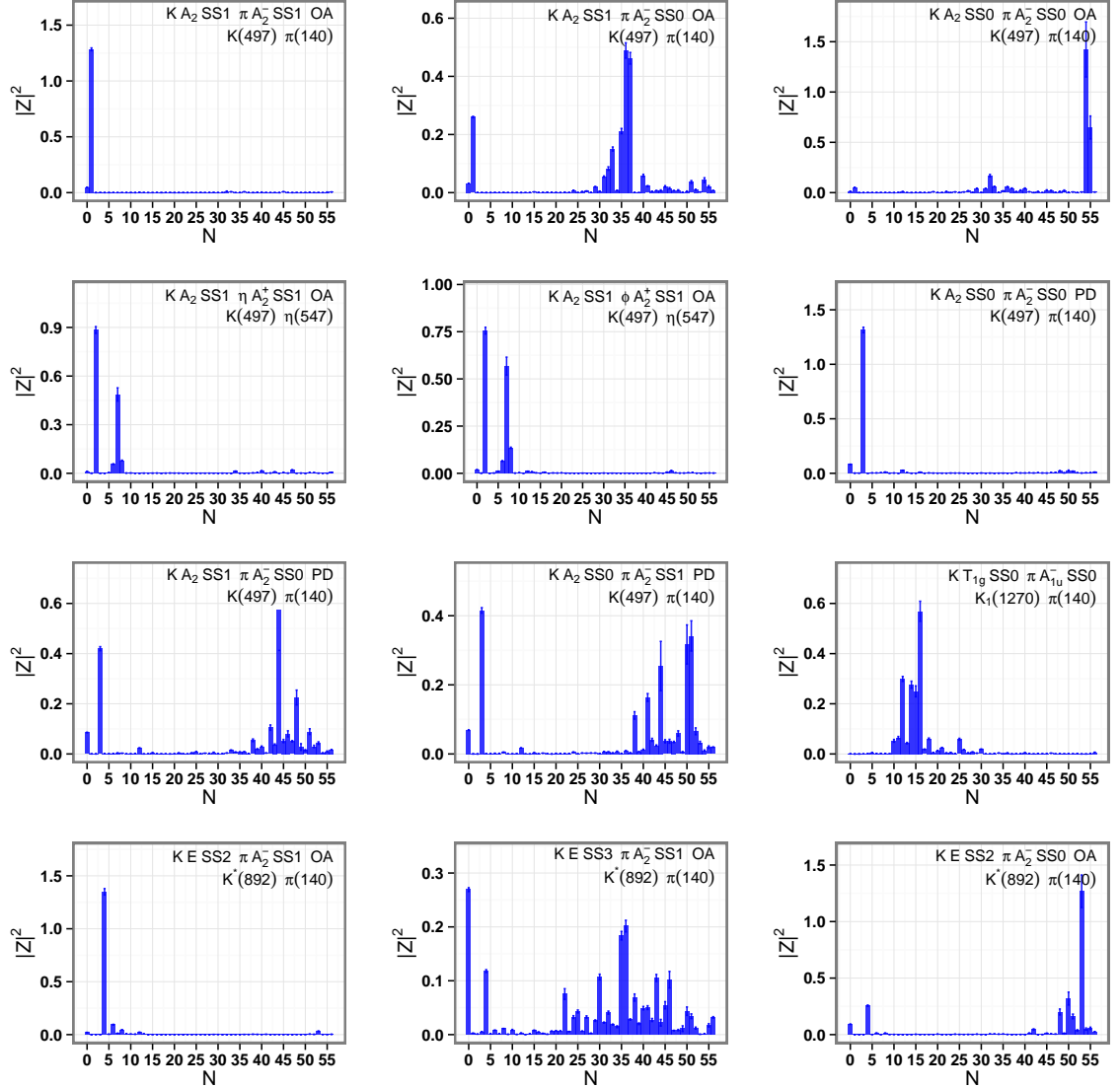


Figure 6.7: Overlap factors $|Z_m^{(N)}|^2$ for various two-meson operators against eigenstates labelled by N . A description of each operator is given in the top right hand corner of each plot, along with the dominant physical content created by the operator. Most operators have a dominant single peak, and these can be used to identify the energy levels.

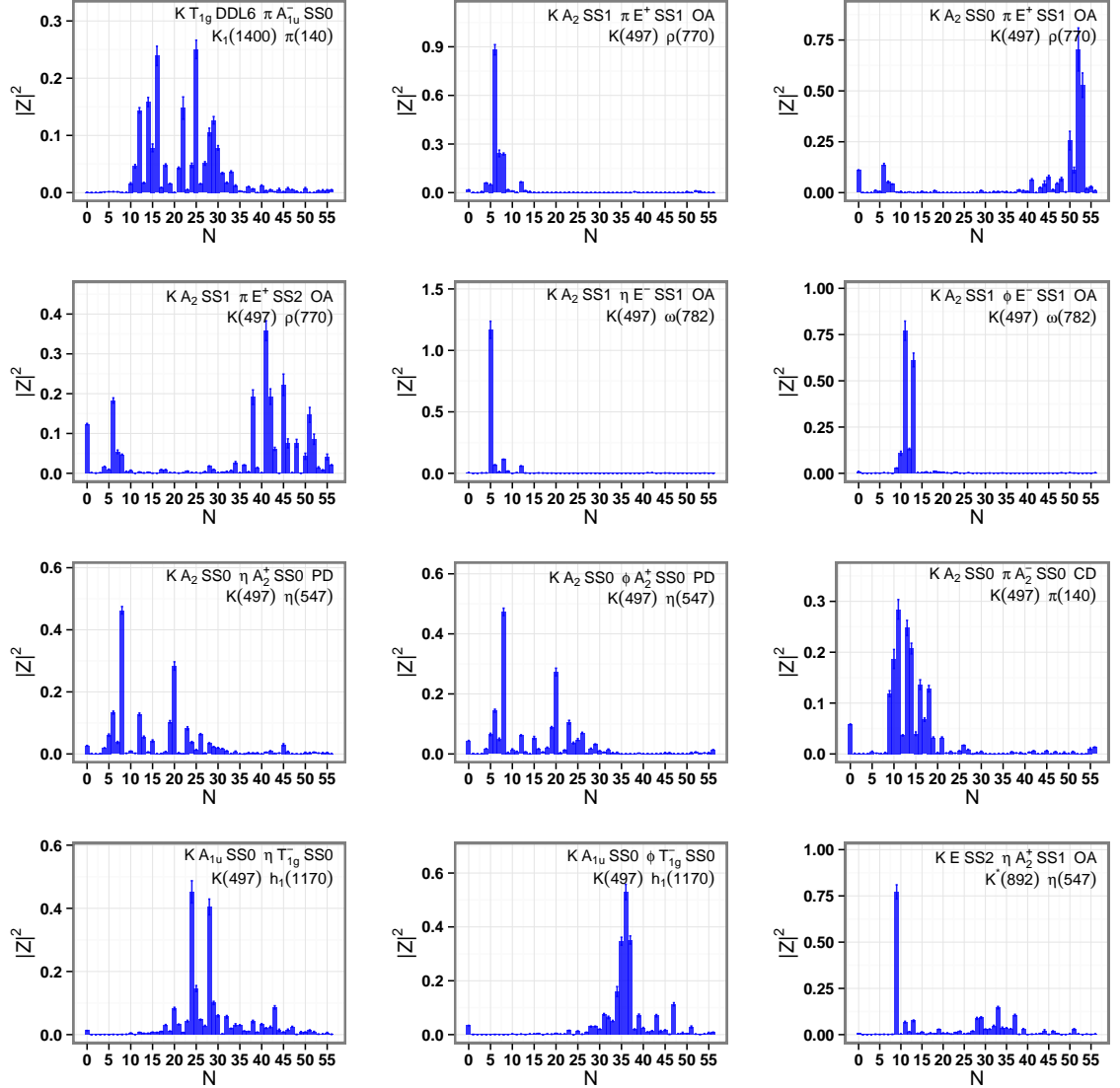


Figure 6.8: Overlap factors $|Z_m^{(N)}|^2$ for various two-meson operators against eigenstates labelled by N . A description of each operator is given in the top right hand corner of each plot, along with the dominant physical content created by the operator. Most operators have a dominant single peak, and these can be used to identify the energy levels.

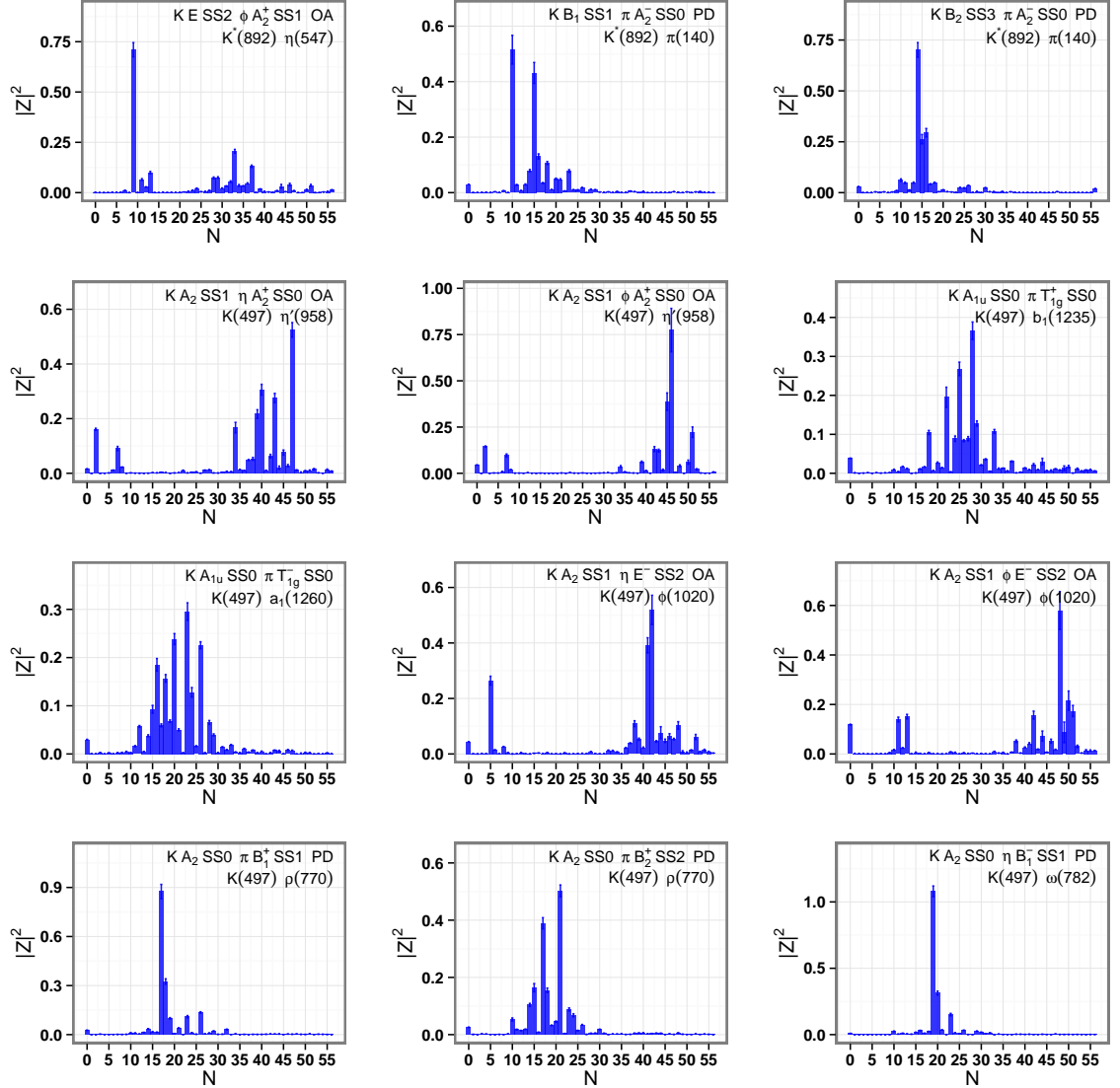


Figure 6.9: Overlap factors $|Z_m^{(N)}|^2$ for various two-meson operators against eigenstates labelled by N . A description of each operator is given in the top right hand corner of each plot, along with the dominant physical content created by the operator. Most operators have a dominant single peak, and these can be used to identify the energy levels.

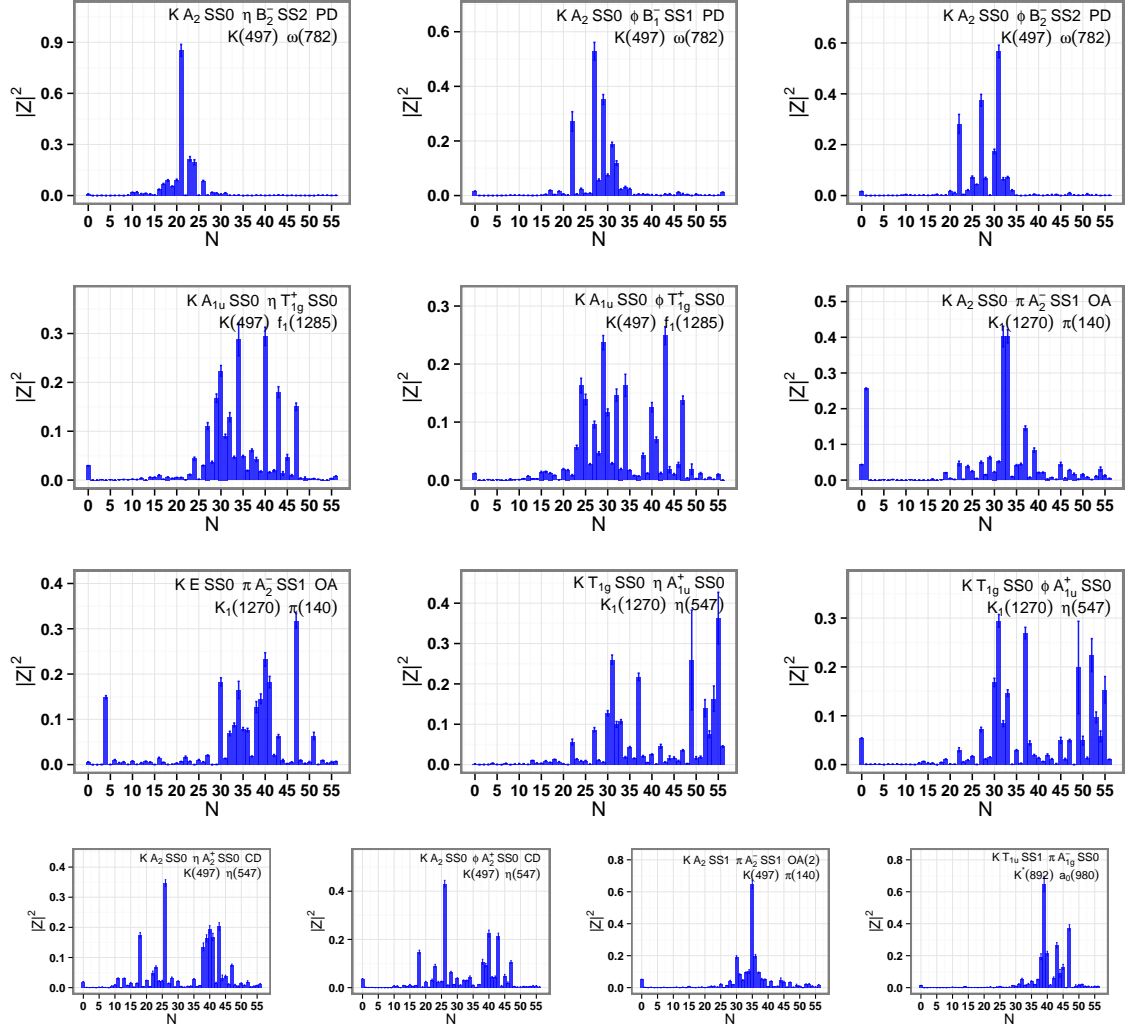


Figure 6.10: Overlap factors $|Z_m^{(N)}|^2$ for various two-meson operators against eigenstates labelled by N . A description of each operator is given in the top right hand corner of each plot, along with the dominant physical content created by the operator. Most operators have a dominant single peak, and these can be used to identify the energy levels.

factors for the lowest-lying SH-optimized operator, which has a single dominant peak at level 0. We identify level 0 as the lowest-lying resonance precursor state, expected to be the $K^*(892)$ in infinite volume. In the bottom plot in Fig. 6.11, we show the $dt = 3$ effective mass associated with the level-0 diagonal element of the rotated 57×57 correlator matrix, shown by blue squares. We also show the effective mass associated with the level-0 diagonal element of the rotated 9×9 correlator submatrix involving only the single-hadron operators. Energies extracted from two-exponential fits to these diagonal correlator elements are also shown. These energy extractions are consistent within statistical uncertainty, but the inclusion of two-meson operators has substantially decreased the statistical uncertainty, improving the energy extraction.

Similarly, the top plot in Fig. 6.12 shows that the first-excited SH-optimized operator mainly produces level 12, with small overlaps to a few other states. Hence, we identify level 12 as the precursor of the first-excited resonance in this channel. The bottom plot in this figure once again shows the improvement in the energy extraction that results from including two-meson operators.

In Fig. 6.13, we observe two dominant peaks at level 10 and level 13. The energy of level 10 is $0.3174(98)a_t^{-1}$, whereas the energy of level 13 is $0.3229(59)a_t^{-1}$. In this case, the energy of the resonance precursor state happens to fall very close to the energy of a state comprised of the decay products of this resonance. The stationary states are admixtures of the single-hadron and two-meson states. This mixing will be studied in more detail in the future. For now, we simply select the energy of level 13 as the energy of the single-meson resonance precursor state. The bottom plot shows the substantial improvement in the energy extraction by including two-meson operators.

This procedure can be repeated using each of the other SH-optimized operators, and we identify levels 34, 44, 52, 55 and 56 to represent the energies of higher-lying single-meson precursor states. The overlap factors of these SH-optimized operators and the improvements of the energy extractions due to including two-meson operators are shown in Figs. 6.14, 6.15, 6.16, 6.17, and 6.18.

To help with the level identification, we have devised a few operators whose classical small- a expansions have spin 3 and spin 4. The overlap factors for these operators will help to identify states that will evolve into spin-3 and spin-4 resonances in infinite volume, such as the $K_3^*(1780)$ resonance. These overlap factors have not yet been computed, but will be evaluated in the near future. To identify the spin-3 resonance

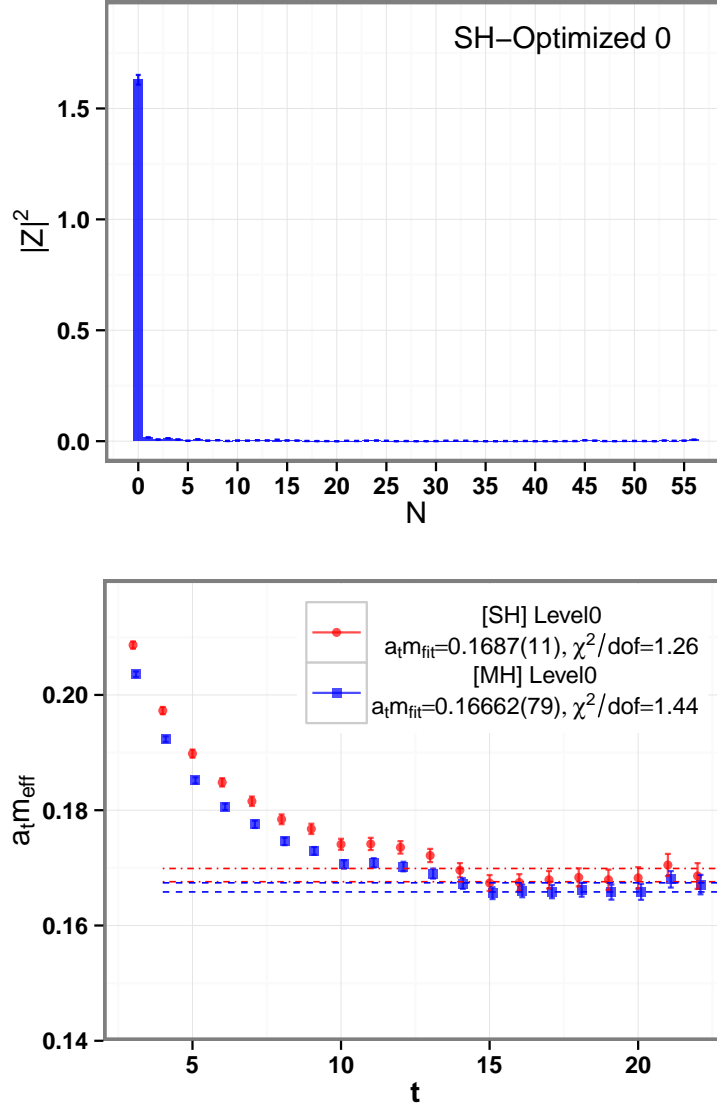


Figure 6.11: (Top) Overlap factor $|\tilde{Z}_m^{(N)}|^2$ for the 0-th single-meson optimized operator, defined in Eq. 6.3, against eigenstates labelled by N . From this plot, we identify level 0 as the lowest-lying resonance precursor state. (Bottom) The $dt = 3$ effective masses against t of level 0 from the correlator submatrix involving only the single-hadron operators (red circles) and level 0 from the full correlator matrix (blue squares). Energies obtained from two-exponential fits are indicated by horizontal dashed lines. The two energy estimates are consistent within errors, but including two-meson operators improves the mass extraction.

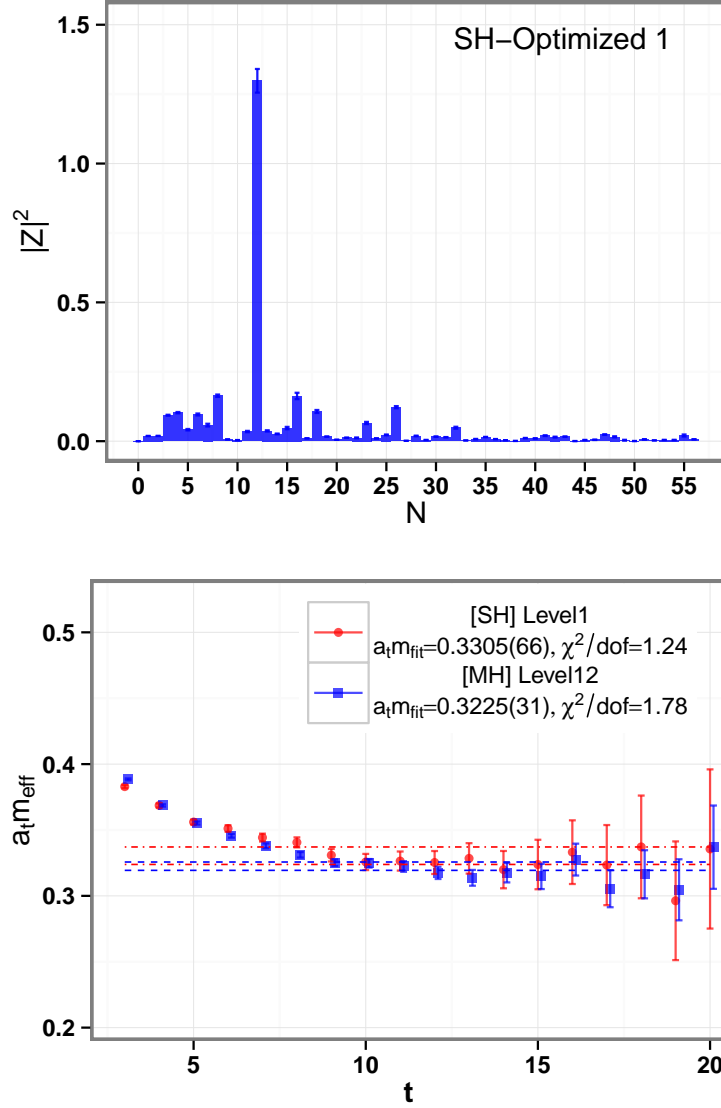


Figure 6.12: (Top) Overlap factors $|\tilde{Z}_m^{(N)}|^2$ for the 1-st single-meson optimized operator, defined in Eq. 6.3, against eigenstates labelled by N . From this plot, we identify level 12 as the resonance precursor state associated with this optimized SH operator. (Bottom) The $dt = 3$ effective masses against t of level 1 from the correlator sub-matrix involving only the single-hadron operators (red circles) and level 12 from the full correlator matrix (blue squares). Energies obtained from two-exponential fits are indicated by horizontal dashed lines. The two energy estimates are consistent within errors, but including two-meson operators improves the mass extraction.

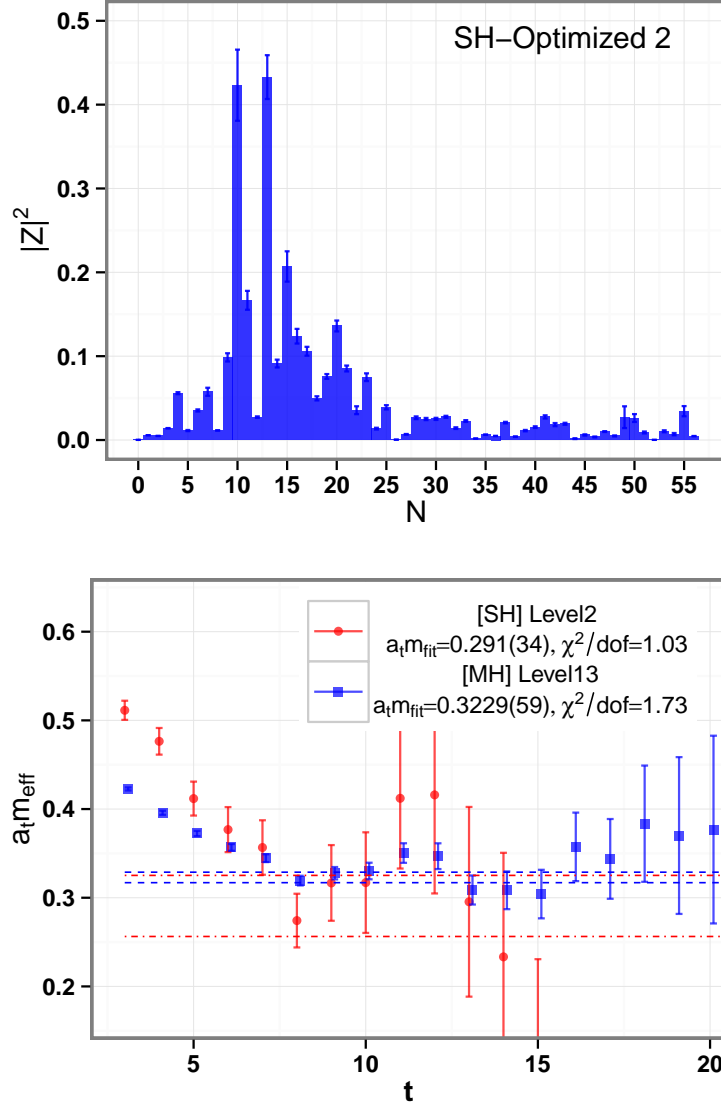


Figure 6.13: (Top) Overlap factors $|\tilde{Z}_m^{(N)}|^2$ for the 2-nd single-meson optimized operator, defined in Eq. 6.3, against eigenstates labelled by N . From this plot, we identify the resonance precursor state associated with this optimized SH operator as a mixture of levels 10 and 13. (Bottom) The $dt = 3$ effective masses against t of level 2 from the correlator submatrix involving only the single-hadron operators (red circles) and level 13 from the full correlator matrix (blue squares). Energies obtained from two-exponential fits are indicated by horizontal dashed lines. The two energy estimates are consistent within errors, but including two-meson operators improves the mass extraction.

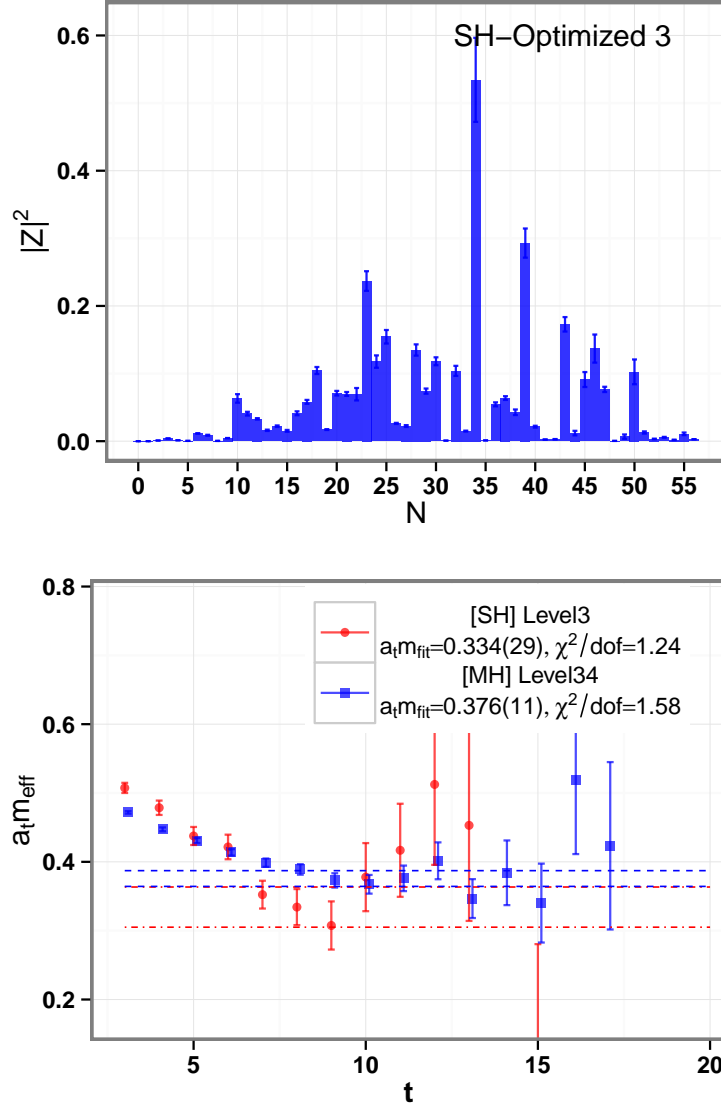


Figure 6.14: (Top) Overlap factors $|\tilde{Z}_m^{(N)}|^2$ for the 3-rd single-meson optimized operator, defined in Eq. 6.3, against eigenstates labelled by N . From this plot, we identify level 34 as the resonance precursor state associated with this optimized SH operator. (Bottom) The $dt = 3$ effective masses against t of level 3 from the correlator submatrix involving only the single-hadron operators (red circles) and level 34 from the full correlator matrix (blue squares). Energies obtained from two-exponential fits are indicated by horizontal dashed lines. The two energy estimates are consistent within errors, but including two-meson operators improves the mass extraction.

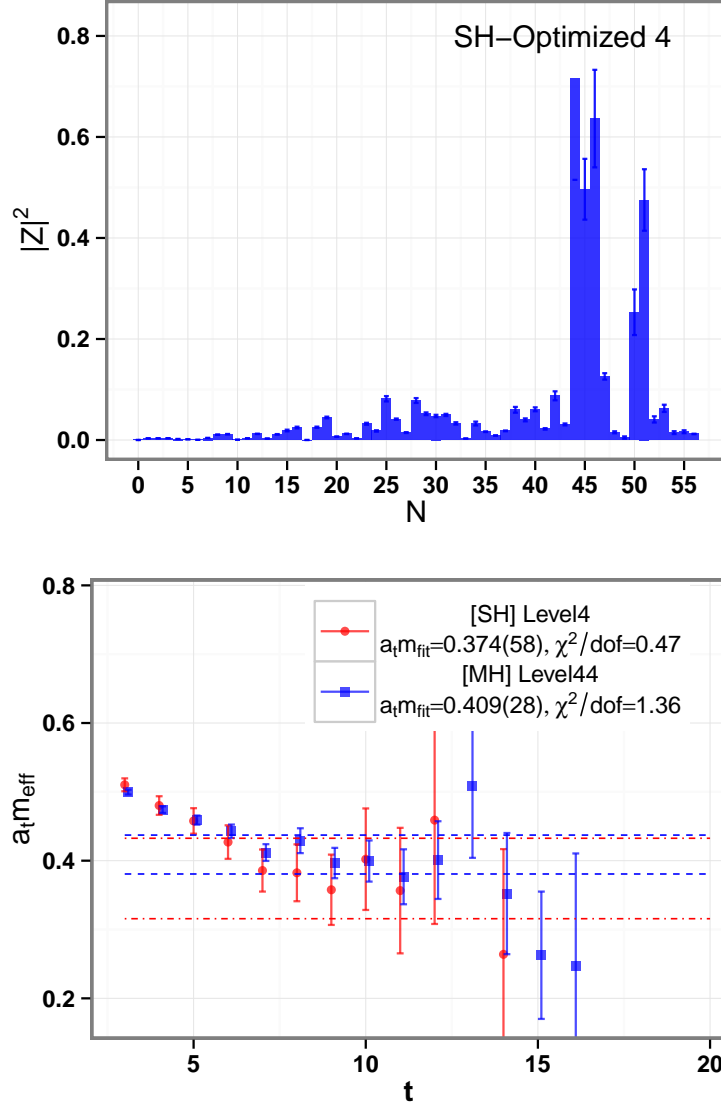


Figure 6.15: (Top) Overlap factors $|\tilde{Z}_m^{(N)}|^2$ for the 4-th single-meson optimized operator, defined in Eq. 6.3, against eigenstates labelled by N . From this plot, we identify the resonance precursor state associated with this optimized SH operator as a mixture of levels 44 and 46. (Bottom) The $dt = 3$ effective masses against t of level 4 from the correlator submatrix involving only the single-hadron operators (red circles) and level 44 from the full correlator matrix (blue squares). Energies obtained from two-exponential fits are indicated by horizontal dashed lines. The two energy estimates are consistent within errors, but including two-meson operators improves the mass extraction.

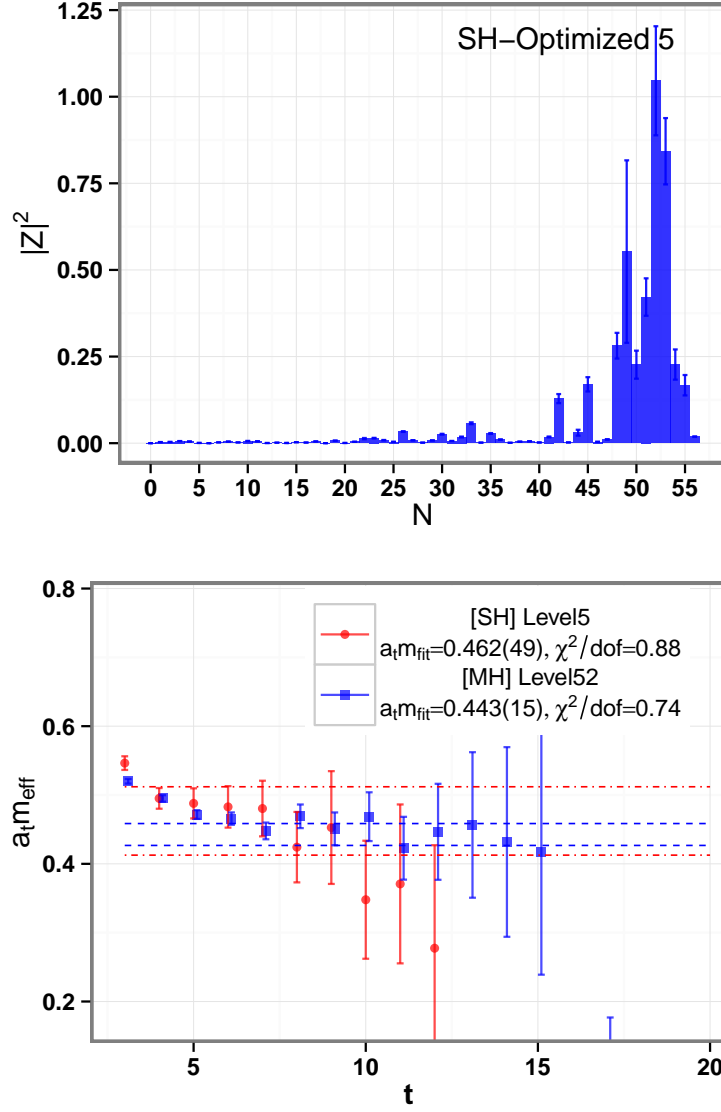


Figure 6.16: (Top) Overlap factors $|\tilde{Z}_m^{(N)}|^2$ for the 5-th single-meson optimized operator, defined in Eq. 6.3, against eigenstates labelled by N . From this plot, we identify level 52 as the resonance precursor state associated with this optimized SH operator. (Bottom) The $dt = 3$ effective masses against t of level 5 from the correlator submatrix involving only the single-hadron operators (red circles) and level 52 from the full correlator matrix (blue squares). Energies obtained from two-exponential fits are indicated by horizontal dashed lines. The two energy estimates are consistent within errors, but including two-meson operators improves the mass extraction.

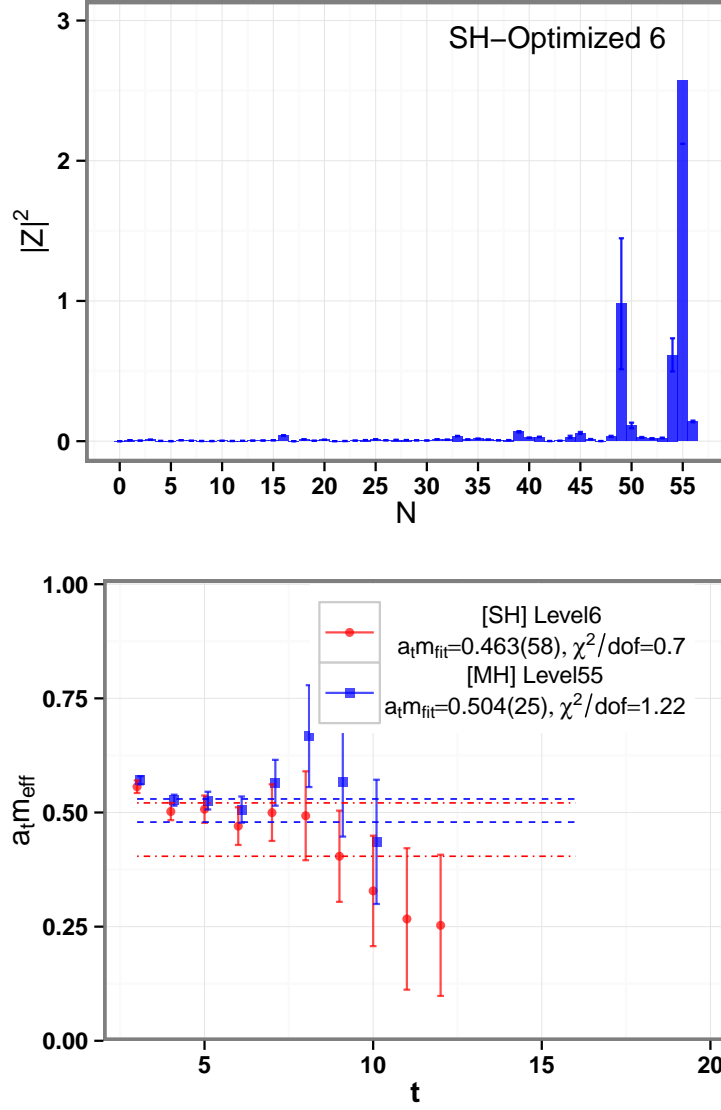


Figure 6.17: (Top) Overlap factors $|\tilde{Z}_m^{(N)}|^2$ for the 6-th single-meson optimized operator, defined in Eq. 6.3, against eigenstates labelled by N . From this plot, we identify level 55 as the resonance precursor state associated with this optimized SH operator. (Bottom) The $dt = 3$ effective masses against t of level 6 from the correlator submatrix involving only the single-hadron operators (red circles) and level 55 from the full correlator matrix (blue squares). Energies obtained from two-exponential fits are indicated by horizontal dashed lines. The two energy estimates are consistent within errors, but including two-meson operators improves the mass extraction.

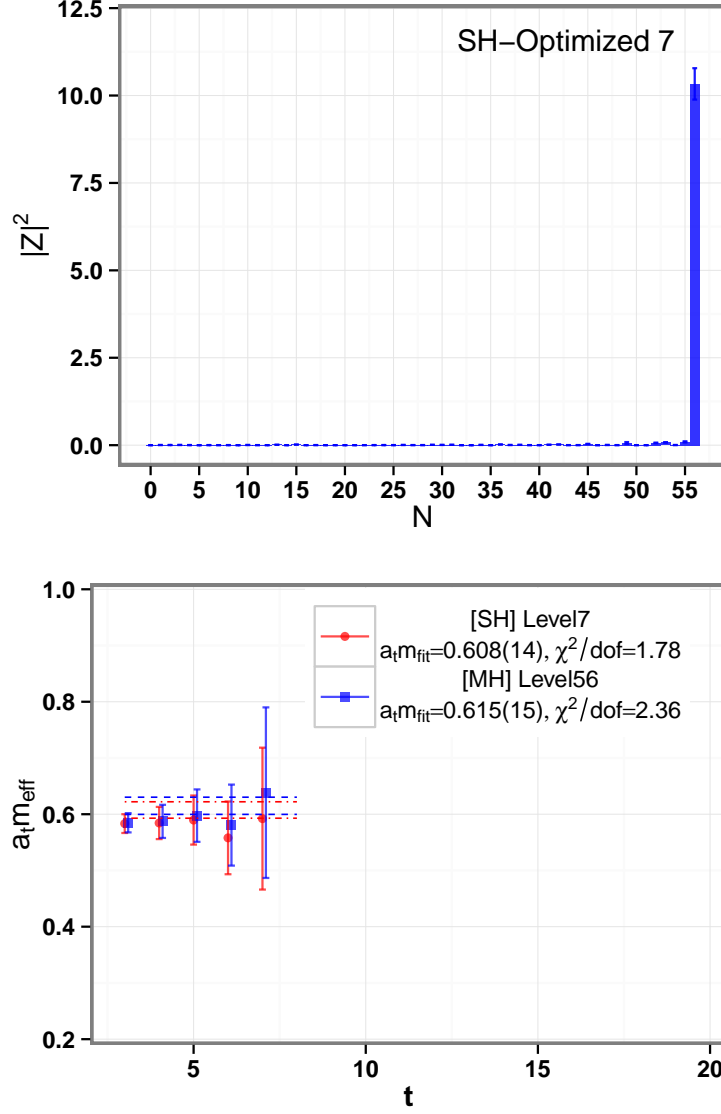


Figure 6.18: (Top) Overlap factors $|\tilde{Z}_m^{(N)}|^2$ for the 7-th single-meson optimized operator, defined in Eq. 6.3, against eigenstates labelled by N . From this plot, we identify level 56 as the resonance precursor state associated with this optimized SH operator. (Bottom) The $dt = 3$ effective masses against t of level 7 from the correlator submatrix involving only the single-hadron operators (red circles) and level 56 from the full correlator matrix (blue squares). Energies obtained from two-exponential fits are indicated by horizontal dashed lines. The two energy estimates are consistent within errors, but including two-meson operators improves the mass extraction.

precursor state in this channel, we will also look at the precursor states in the A_{2u} channel in the future.

We summarize our single-meson precursor state masses m in Fig. 6.19. We express the results as ratios $5m/(3m_\Omega)$, where m_Ω is the Ω baryon mass, which we separately determine using the same $(24^3|390)$ ensemble. Given the experimental value for the Ω baryon, the ratios $5m/(3m_\Omega)$ are numerically close to the particle masses in GeV. We believe we have reliably extracted the first five lowest-lying single-hadron resonances in the T_{1u} channel, since we have constructed a set of orthogonal levels from the 58×58 matrix. We also tentatively identified three higher-lying single-hadron resonances, two of which are indicated by the hollow boxes. We view their extractions as merely tentative since we expect that there are other two-meson states lying below these that have not been taken into account. Note that three and four meson states are not taken into account at all in these computations. Given the small mixing observed between the single-hadron operators and the two-meson operators, and that we are mainly interested in the qualitative pattern of single-hadron resonance precursor states, the neglect of states involving three or more particles is not expected to be a serious omission.

The experimentally known resonances in the T_{1u} channel are also shown in Fig. 6.19. However, a direct comparison of our results with experiment is not possible since our calculations use unphysical u, d quark masses leading to a pion mass of 390 MeV. Future calculations using the $(32^3|240)$ ensemble will perform an extrapolation of our results to the physical limit, and greatly facilitate comparison with experiment.

Finally, in Fig. 6.20, we compare our results with those obtained in a recent study[16] of the $I = 1$, $S = 0$, T_{1u}^+ channel. The pattern of resonances is seen to be very similar, which is not too surprising given the closeness of the s -quark mass and the unphysically large u, d quark masses used in both computations. This similarity is expected since the single-meson flavor structure in the isovector T_{1u}^+ channel is du , whereas the flavor structure in the isodoublet T_{1u} channel is su , and our u, d, s quark masses are similar. Again, future calculations using the $(32^3|240)$ ensemble will prove to be very interesting.

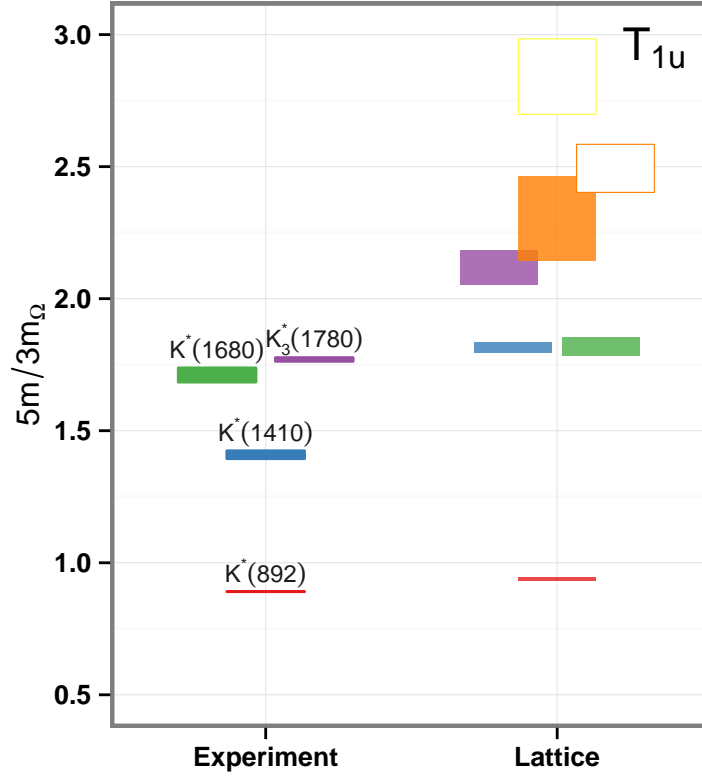


Figure 6.19: (Right) Our results m for the energies of the kaon resonance precursor states in the isodoublet strangeness $S = 1$ T_{1u} channel using the $(24^3|390)$ ensemble. Results are shown as ratios $5m/(3m_\Omega)$, where m_Ω is the mass of the Ω baryon. Vertical heights of boxes show statistical uncertainties. Hollow boxes show energy extractions for which some lower-lying two-mesons states have been neglected. (Left) Isodoublet strangeness $S = 1$ kaon resonance masses of spin-1 and spin-3 measured in experiments.

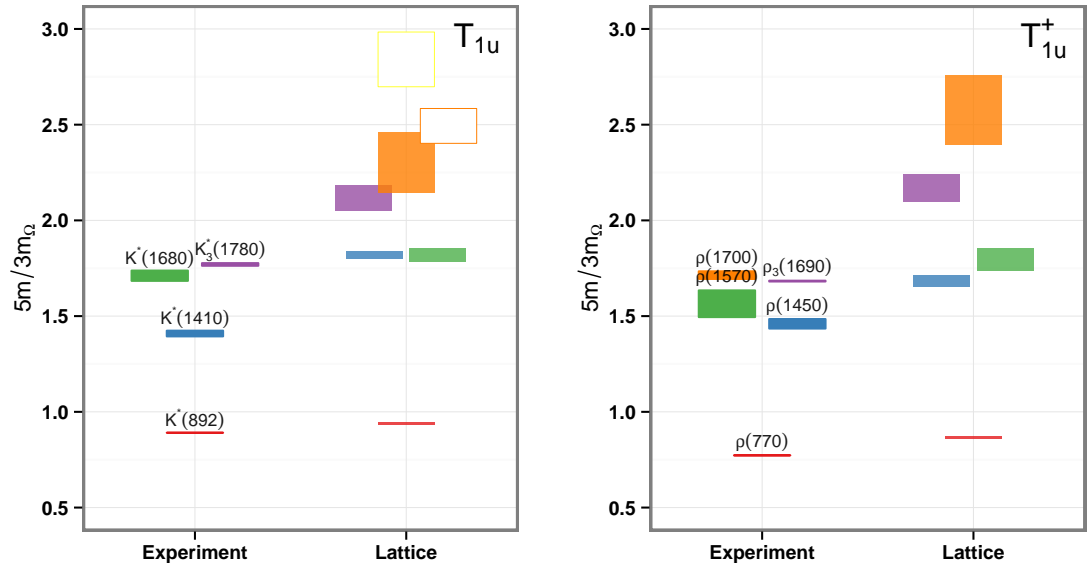


Figure 6.20: Comparison of our results for the kaon resonance precursor states (left) with recent results[16] in the $I = 1, S = 0, T_{1u}^+$ channel (right). Both results are computed using the $(24^3|390)$ ensemble. Experimental results are also shown.

Chapter 7

Conclusion and Outlook

We have presented in this work the effective use of a large 58×58 correlation matrix to extract 57 energy levels in the isodoublet strangeness $S = 1$ T_{1u} channel of QCD for an anisotropic $24^3 \times 128$ lattice with u, d quark masses producing a pion mass of 390 MeV. The 58 hadronic operators were composed of 49 two-meson operators and 9 single-meson operators, constructed from smeared quark fields displaced using stout-smeared gauge links. A Markov chain Monte Carlo method was used to estimate the correlation matrix elements, and the stochastic LapH method was used to efficiently handle the quark propagation needed to evaluate all quark line diagrams. Our main goal was to identify the kaon resonance precursor states in this channel. This work, along with a companion study in Ref. [16], are the first to study excited states in lattice QCD using such large correlator matrices and taking two-meson states into account so completely.

The analysis of our correlation matrix showed nonzero but small coupling between single-meson and two-meson states. In order to reliably extract a single-meson energy of interest, it was necessary to consider all lower-lying and nearby two-meson states. With such a large number of energies extracted, level identification was a key issue. QCD is a complicated interacting quantum field theory, so characterizing its stationary states in finite volume is not likely to be done in a simple way. Level identification was inferred from the Z overlaps of probe operators, analogous to deducing resonance properties from scattering cross sections in experiments. To identify the resonance precursor states, we used probe operators that were “optimized” linear combinations of the single-hadron operators used. Five kaon resonance precursor states were reliably extracted and identified from the 57 energy levels. Inclusion of the two-meson

operators, in addition to the single-hadron operators, substantially improved our energy extractions of the excited resonance precursor states. Three and four meson states were not taken into account at all in these computations. Given the small mixing observed between the single-hadron operators and the two-meson operators, and that we were mainly interested in the qualitative pattern of single-hadron resonance precursor states, the neglect of states involving three or more particles was not viewed to be a serious omission.

Calculations using an ensemble generated with an anisotropic $32^3 \times 256$ lattice for u, d quark masses producing a pion mass of 240 MeV will occur in the near future. We also plan to study the energies in all other symmetry channels. To assist with level identification, operators whose classical small- a expansions are dominated by spin-3 and spin-4 operators will be used. More detailed studies of the two-meson energies, with a comparison to the energies of two free mesons, will be carried out as well. Scattering phase shifts will be evaluated, and in some cases, resonance widths will be determined from finite-box energy shifts. Such studies are now possible on large lattices due to the stochastic LapH method.

Bibliography

- [1] M. Gell-Mann, “A Schematic Model of Baryons and Mesons”, Phys. Lett. **8**, 214–215 (1964).
- [2] G. Zweig, “An SU(3) model for strong interaction symmetry and its breaking. Version 1”, (1964).
- [3] H. Fritzsche, M. Gell-Mann, and H. Leutwyler, “Advantages of the Color Octet Gluon Picture”, Phys. Lett. **B47**, 365–368 (1973).
- [4] D. Gross and F. Wilczek, “Ultraviolet Behavior of Nonabelian Gauge Theories”, Phys. Rev. Lett. **30**, 1343–1346 (1973).
- [5] H. D. Politzer, “Reliable Perturbative Results for Strong Interactions?”, Phys. Rev. Lett. **30**, 1346–1349 (1973).
- [6] J. B. et al., “Review of Particle Physics”, Phys. Rev. **D86**, 010001 (2012).
- [7] S. Godfrey and N. Isgur, “Mesons in a Relativized Quark Model with Chromodynamics”, Phys. Rev. **D32**, 189–231 (1985).
- [8] G. ’t Hooft, “The Topological Mechanism for Permanent Quark Confinement in a Nonabelian Gauge Theory”, Phys. Scripta **25**, 133–142 (1982).
- [9] K. G. Wilson, “Confinement of Quarks”, Phys. Rev. **D10**, 2445–2459 (1974).
- [10] G. S. Bali, “QCD forces and heavy quark bound states”, Phys. Rept. **343**, 1–136 (2001).
- [11] G. S. Bali, H. Neff, T. Duessel, T. Lippert, and K. Schilling, “Observation of string breaking in QCD”, Phys. Rev. **D71**, 114513 (2005).
- [12] S. Durr, Z. Fodor, J. Frison, C. Hoelbling, R. Hoffmann, et al., “Ab-Initio Determination of Light Hadron Masses”, Science **322**, 1224–1227 (2008).

- [13] C. Morningstar, J. Bulava, J. Foley, K. J. Juge, D. Lenkner, et al., “Improved stochastic estimation of quark propagation with Laplacian Heaviside smearing in lattice QCD”, Phys. Rev. **D83**, 114505 (2011).
- [14] J. Bulava, “An Improved Variance Reduction Technique for Stochastic All-to-All Quark Propagators in Lattice QCD Spectrum Computations”, PhD thesis (Carnegie Mellon University, 2010).
- [15] C. Wong, “The Stochastic Laplacian Heaviside Method in Lattice QCD and its First Applications to Hadron Spectroscopy”, PhD thesis (Carnegie Mellon University, 2011).
- [16] D. W. Lenkner, “The Spectrum of Meson States in the Isovector Non-strange T_{1u}^+ Channel by the Stochastic LapH Method in Lattice QCD”, PhD thesis (Carnegie Mellon University, 2013).
- [17] M. Luscher, “Volume Dependence of the Energy Spectrum in Massive Quantum Field Theories. 2. Scattering States”, Commun. Math. Phys. **105**, 153–188 (1986).
- [18] M. Luscher, “Two particle states on a torus and their relation to the scattering matrix”, Nucl. Phys. **B354**, 531–578 (1991).
- [19] M. Luscher, “Signatures of unstable particles in finite volume”, Nucl. Phys. **B364**, 237–254 (1991).
- [20] R. P. Feynman, “Space-time approach to non-relativistic quantum mechanics”, Rev. Mod. Phys. **20**, 367 (1948).
- [21] L. H. Karsten and J. Smit, “Lattice Fermions: Species Doubling, Chiral Invariance, and the Triangle Anomaly”, Nucl. Phys. **B183**, 103 (1981).
- [22] C. Gattringer and C. B. Lang, *Quantum chromodynamics on the lattice: an introductory presentation* (Springer, 2009).
- [23] K. Symanzik, “Continuum Limit and Improved Action in Lattice Theories: 1. Principles and ϕ^4 Theory”, Nucl. Phys. **B226**, 187 (1983).
- [24] K. Symanzik, “Continuum Limit and Improved Action in Lattice Theories: 2. $O(N)$ Nonlinear Sigma Model in Perturbation Theory”, Nucl. Phys. **B226**, 205 (1983).

- [25] M. Luscher and P. Weisz, “On-Shell Improved Lattice Gauge Theories”, *Commun. Math. Phys.* **97**, 59 (1985).
- [26] G. Curci, P. Menotti, and G. Paffuti, “Symanzik’s Improved Lagrangian for Lattice Gauge Theory”, *Phys. Lett.* **B130**, 205 (1983).
- [27] G. P. Lepage and P. B. Mackenzie, “On the viability of lattice perturbation theory”, *Phys. Rev.* **D48**, 2250–2264 (1993).
- [28] G. Parisi, “Recent Progresses in Gauge Theories”, *World Sci. Lect. Notes Phys.* **49**, 349–386 (1980).
- [29] R. G. Edwards, B. Joo, and H.-W. Lin, “Tuning for Three-flavors of Anisotropic Clover Fermions with Stout-link Smearing”, *Phys. Rev.* **D78**, 054501 (2008).
- [30] C. J. Morningstar and M. J. Peardon, “Efficient glueball simulations on anisotropic lattices”, *Phys. Rev.* **D56**, 4043–4061 (1997).
- [31] R. Gupta, “Introduction to lattice QCD”, 83–219 (1997).
- [32] H. B. Nielsen and M. Ninomiya, “No Go Theorem for Regularizing Chiral Fermions”, *Phys. Lett.* **B105**, 219 (1981).
- [33] J. B. Kogut and L. Susskind, “Hamiltonian Formulation of Wilson’s Lattice Gauge Theories”, *Phys. Rev.* **D11**, 395 (1975).
- [34] L. Susskind, “Lattice Fermions”, *Phys. Rev.* **D16**, 3031–3039 (1977).
- [35] H. Sharatchandra, H. Thun, and P. Weisz, “Susskind Fermions on a Euclidean Lattice”, *Nucl. Phys.* **B192**, 205 (1981).
- [36] D. B. Kaplan, “A Method for simulating chiral fermions on the lattice”, *Phys. Lett.* **B288**, 342–347 (1992).
- [37] V. Furman and Y. Shamir, “Axial symmetries in lattice QCD with Kaplan fermions”, *Nucl. Phys.* **B439**, 54–78 (1995).
- [38] H. Neuberger, “Exactly massless quarks on the lattice”, *Phys. Lett.* **B417**, 141–144 (1998).
- [39] H. Neuberger, “More about exactly massless quarks on the lattice”, *Phys. Lett.* **B427**, 353–355 (1998).
- [40] K. G. Wilson, “New Phenomena In Subnuclear Physics. Part A. Proceedings of the First Half of the 1975 International School of Subnuclear Physics”, A. Zichichi, Plenum Press, New York, 69–142 (1977).

- [41] C. Morningstar and M. J. Peardon, “Analytic smearing of SU(3) link variables in lattice QCD”, Phys. Rev. **D69**, 054501 (2004).
- [42] B. Sheikholeslami and R. Wohlert, “Improved Continuum Limit Lattice Action for QCD with Wilson Fermions”, Nucl. Phys. **B259**, 572 (1985).
- [43] P. Matthews and A. Salam, “The Green’s functions of quantized fields”, Nuovo Cim. **12**, 563–565 (1954).
- [44] P. Matthews and A. Salam, “Propagators of quantized field”, Nuovo Cim. **2**, 120–134 (1955).
- [45] G. C. Wick, “The Evaluation of the Collision Matrix”, Phys. Rev. **80**, 268–272 (1950).
- [46] C. Morningstar, “The Monte Carlo method in quantum field theory”, (2007).
- [47] B. A. Berg, *Markov Chain Monte Carlo Simulations And Their Statistical Analysis: With Web-based Fortran Code* (World Scientific, 2004).
- [48] H. J. Rothe, *Lattice gauge theories: an introduction* (World Scientific, 2005).
- [49] N. Metropolis, A. Rosenbluth, M. Rosenbluth, A. Teller, and E. Teller, “Equation of state calculations by fast computing machines”, J. Chem. Phys. **21**, 1087–1092 (1953).
- [50] W. Hastings, “Monte Carlo Sampling Methods Using Markov Chains and Their Applications”, Biometrika **57**, 97–109 (1970).
- [51] U. Wolff, “Critical Slowing Down”, Nucl. Phys. Proc. Suppl. **17**, 93–102 (1990).
- [52] M. Creutz, L. Jacobs, and C. Rebbi, “Experiments with a Gauge Invariant Ising System”, Phys. Rev. Lett. **42**, 1390 (1979).
- [53] M. Creutz, L. Jacobs, and C. Rebbi, “Monte Carlo Study of Abelian Lattice Gauge Theories”, Phys. Rev. **D20**, 1915 (1979).
- [54] M. Creutz, “Monte Carlo Study of Quantized SU(2) Gauge Theory”, Phys. Rev. **D21**, 2308–2315 (1980).
- [55] A. Kennedy and B. Pendleton, “Improved Heat Bath Method for Monte Carlo Calculations in Lattice Gauge Theories”, Phys. Lett. **B156**, 393–399 (1985).
- [56] S. L. Adler, “An Overrelaxation Method for the Monte Carlo Evaluation of the Partition Function for Multiquadratic Actions”, Phys. Rev. **D23**, 2901 (1981).

- [57] D. Weingarten and D. Petcher, “Monte Carlo Integration for Lattice Gauge Theories with Fermions”, *Phys. Lett.* **B99**, 333 (1981).
- [58] S. Duane, A. Kennedy, B. Pendleton, and D. Roweth, “Hybrid Monte Carlo”, *Phys. Lett.* **B195**, 216–222 (1987).
- [59] I. Omelyan, I. Mryglod, and R. Folk, “Symplectic analytically integrable decomposition algorithms: classification, derivation, and application to molecular dynamics, quantum and celestial mechanics simulations”, *Computer Physics Communications* **151**, 272–314 (2003).
- [60] Y. Saad, *Iterative Methods for Sparse Linear Systems*, 2nd (Society for Industrial and Applied Mathematics, Philadelphia, PA, USA, 2003).
- [61] M. Luscher, “Computational Strategies in Lattice QCD”, 331–399 (2010).
- [62] M. Clark, “The Rational Hybrid Monte Carlo Algorithm”, *PoS LAT2006*, 004 (2006).
- [63] A. Frommer and P. Maass, “Fast CG-Based Methods for Tikhonov–Phillips Regularization”, *SIAM Journal on Scientific Computing* **20**, 1831–1850 (1999).
- [64] B. Jegerlehner, “Krylov space solvers for shifted linear systems”, (1996).
- [65] H.-W. Lin et al., “First results from 2+1 dynamical quark flavors on an anisotropic lattice: Light-hadron spectroscopy and setting the strange-quark mass”, *Phys. Rev.* **D79**, 034502 (2009).
- [66] R. Morrin, A. O. Cais, M. Peardon, S. M. Ryan, and J.-I. Skullerud, “Dynamical QCD simulations on anisotropic lattices”, *Phys. Rev.* **D74**, 014505 (2006).
- [67] M. Hasenbusch, “Speeding up the hybrid Monte Carlo algorithm for dynamical fermions”, *Phys. Lett.* **B519**, 177–182 (2001).
- [68] C. Urbach, K. Jansen, A. Shindler, and U. Wenger, “HMC algorithm with multiple time scale integration and mass preconditioning”, *Comput. Phys. Commun.* **174**, 87–98 (2006).
- [69] M. Hasenbusch and K. Jansen, “Speeding up lattice QCD simulations with clover improved Wilson fermions”, *Nucl. Phys.* **B659**, 299–320 (2003).
- [70] M. Luscher, R. Narayanan, P. Weisz, and U. Wolff, “The Schrodinger functional: A Renormalizable probe for nonAbelian gauge theories”, *Nucl. Phys.* **B384**, 168–228 (1992).

- [71] T. R. Klassen, “The Schrodinger functional for improved gluon and quark actions”, Nucl. Phys. **B509**, 391–428 (1998).
- [72] T. R. Klassen, “The Anisotropic Wilson gauge action”, Nucl. Phys. **B533**, 557–575 (1998).
- [73] M. Albanese et al., “Glueball Masses and String Tension in Lattice QCD”, Phys. Lett. **B192**, 163–169 (1987).
- [74] M. G. Alford, T. Klassen, and Lepage, “The D234 action for light quarks”, Nucl. Phys. Proc. Suppl. **47**, 370–373 (1996).
- [75] M. Peardon et al., “A Novel quark-field creation operator construction for hadronic physics in lattice QCD”, Phys. Rev. **D80**, 054506 (2009).
- [76] C. Morningstar, J. Bulava, B. Fahy, J. Foley, Y. Jhang, et al., “Extended hadron and two-hadron operators of definite momentum for spectrum calculations in lattice QCD”, Phys. Rev. **D88**, 014511 (2013).
- [77] S. Basak, R. Edwards, G. Fleming, U. Heller, C. Morningstar, et al., “Group-theoretical construction of extended baryon operators in lattice QCD”, Phys. Rev. **D72**, 094506 (2005).
- [78] R. Penrose, “A Generalized inverse for matrices”, Proc. Cambridge Phil. Soc. **51**, 406–413 (1955).
- [79] J. J. Dudek, R. G. Edwards, B. Joo, M. J. Peardon, D. G. Richards, et al., “Isoscalar meson spectroscopy from lattice QCD”, Phys. Rev. **D83**, 111502 (2011).
- [80] J. Foley, K. Jimmy Juge, A. O’Cais, M. Peardon, S. M. Ryan, et al., “Practical all-to-all propagators for lattice QCD”, Comput. Phys. Commun. **172**, 145–162 (2005).
- [81] C. Michael, “Fitting correlated data”, Phys. Rev. **D49**, 2616–2619 (1994).
- [82] R. G. Edwards and B. Joo, “The Chroma software system for lattice QCD”, Nucl. Phys. Proc. Suppl. **140**, 832 (2005).
- [83] K. Wu and H. Simon, “Thick-Restart Lanczos Method for Large Symmetric Eigenvalue Problems”, SIAM Journal on Matrix Analysis and Applications **22**, 602–616 (2000).

- [84] J. Foley, C. H. Wong, J. Bulava, K. J. Juge, D. Lenkner, et al., “A novel method for evaluating correlation functions in lattice hadron spectroscopy”, (2010).
- [85] M. Matsumoto and T. Nishimura, “Mersenne twister: a 623-dimensionally equidistributed uniform pseudo-random number generator”, *ACM Trans. Model. Comput. Simul.* **8**, 3–30 (1998).